INSTITUTO SUPERIOR TÉCNICO
Universidade Técnica de Lisboa

The effect of wind and turbulence on sound propagation in the atmosphere

André Filipe Garcia Peixoto de Oliveira

Dissertação para obtenção do Grau de Mestre em

Engenharia Aeroespacial

Júri

Presidente:	Doutor Fernando José Parracho Lau
Orientador:	Doutor João Manuel Gonçalves de Sousa Oliveira
Vogais:	Doutor Pedro da Graça Tavares Alvares Serrão

Maio 2012

ACKNOWLEDGEMENTS

I would like to begin by thanking my advisor Professor João Oliveira, for the opportunity of working with him and for his patience, understanding and availability while advising me in my work.

I would also like to express my gratitude to my Family, whose support and love have carried me throughout my Masters degree and will, undoubtedly, continue to do so throughout the rest of my life.

Finally, to my colleagues and friends, whose friendship was important to the conclusion of my Masters degree, I thank you all.

ABSTRACT

In the last years, societies growing environmental and health conscience, obliged the national authorities to reinforce existing legislation concerning the maximum permissible noise levels. These new demands lead to increasingly accurate tools to perform noise analysis, not only because they must include a growing number of parameters that influence its propagation, thus with more complexity, but also with more flexibility, quick and easy use and less computational effort.

This dissertation, after presenting the several existing numerical methods to evaluate the sound propagation and its intrinsic limitations, describes the acoustic wave equation resolution method, using a Green function. Since the focus of this work is to develop a numerical application, which allows incorporating the wind and turbulence effects on sound propagation in the atmosphere, was created a C language numerical program. It includes input and output interfaces which ease the analysis of the referred effects variations on sound propagation.

The numerical program validation was achieved not only by comparing its results with exact numerical methods, but also by using numerical approaches with known accuracy and with results from experimental measurements. The program was applied to an airport by using realistic parameters. The coherent results obtained confirmed that the program developed is numerically accurate and its user interface is suitable and can be, easily and effectively, used to evaluate the effects of wind and turbulence on sound in the vicinity of an airport.

Keywords: sound propagation, wind, turbulence, noise, sound refraction, shadow zone.

RESUMO

Nos últimos anos, crescentes preocupações ambientais e de saúde, obrigaram as autoridades nacionais a reforçar a legislação existente referente aos níveis máximos de ruído admissíveis. Estas exigências conduzem à necessidade de dispor de ferramentas mais precisas de análise de ruído, por um lado mais complexas, por terem de incluir o maior número possível de parâmetros que condicionam a sua propagação, por outro lado mais flexíveis, de rápida e fácil ultilização e com maior rapidez de cálculo.

A presente dissertação, após apresentar os vários métodos númericos existentes para a avaliação da propagação do som e as suas limitações intrínsecas, descreve o método de resolução da equação geral do som por intermédio de uma função de Green. Sendo o objectivo deste trabalho desenvolver uma aplicação numérica que permitisse incorporar o efeito do vento e da turbulência na propagação do som, foi desenvolvido um programa em linguagem C. Este dispõe de interfaces de entrada e saída de dados, que facilitam a análise da variação de ambos os efeitos.

A validação numérica da aplicação foi efectuada, quer por comparação com métodos numéricos exactos, quer usando aproximações numéricas de precisão conhecida, quer ainda, por comparação com resultados de medições experimentais. O programa foi aplicado à situação de um aeroporto usando parâmetros realistas e a coerência dos resultados obtidos confirmou a sua precisão numérica e que a interface é adequada e pode ser, fácil e eficazmente, usada para avaliar o efeito do vento e da turbulência no som, nas proximidades de um aeroporto.

Palavras Chave: propagação do som, vento, turbulência, ruído, refracção do som, região de sombra.

CONTENTS

LIST OF FIGURES

LIST OF TABLES

LIST OF ACRONYMS AND SYMBOLS

Mathematical notation

Boldfaced symbols are used for vectors, for example $\mathbf{r} = (x, y, z)$,

A line above the symbol denotes a time average over turbulent fluctuations, for example $\overline{\chi}$

$\partial_x f = \partial f / \partial x$ partial derivate of function f,

$\partial_x^2 f = \partial^2 f / \partial x^2$ second derivate of function f,

$\nabla f = \left(\partial_x f, \partial_y f, \partial_z f, \right)$ gradient of a scalar function f.

Acronyms

ABL	Atmospheric Boundary Layer
ASL	Atmospheric Surface Layer
C	C programming language
CLI	Command Line type Interface
CNPE	Crank-Nicolson Parabolic Equation
DTF	Discrete Fourier Transform
DUC	Downward Upward Constant profile
FFP	Fast Field Program
FFT	Fast Fourier Transform
FFTW	Fastest Fourier Transform in the West
GFPE	Green´s Function Parabolic Equation
PE	Parabolic Equation
PRNG	Pseudorandom Number Generator
TA	Total Attenuation
TL	Transmission Loss

Roman symbols

a	correlation length of turbulent refractive index fluctuations
A	attenuation factor
b	parameter of logarithmic sound speed profile
B_1	parameter in equation (6.6)
B_2	parameter in equation (6.6)
c	(adiabatic) sound speed
c_0	sound speed at ground surface

c_{eff}	effective sound speed
C	cumulative of equation (4.16)
C_T^2	structure parameter for the temperature fluctuation
C_v^2	structure parameter of the wind speed fluctuation
d	constant value in equation (5.2)
f	frequency
f_0	center frequency of an octave band
f_1	lowest frequency of an octave band
f_2	highest frequency of an octave band
F	spectral density function
g	grain shape factor of porous medium
	two dimensional Green's function
G	three dimensional Green's function
	mode amplitude in equation (3.63)
g_2	two dimensional Green's function
k	wave number
k_a	reference value of wave number at some average height
k_{abs}	absorption layer wave number
k_{eff}	effective wave number
k_h	horizontal wave number
k_{nr}, k_{nz}	components of wave number vector
k_v	vertical wave number
	wave number corresponding to z by Fourier transformation
K_0	parameter of von Kármán turbulence spectrum
L	size of largest eddies, outer scale of turbulence
	Monin-Obukhov lenght
L_p	sound pressure level
$L_{p,free}$	sound pressure level of free field
L_w	sound power level
M	number of vertical points
n	acoustic refractive index
n_d	determinist part of acoustic refractive index n
$\mathbf{n}$	unit normal vector
N	integral
N_{pr}	Prandtl number
p_c	complex amplitude of acoustic pressure
p_{free}	complex pressure of free field
p_{ref}	reference pressure level

P	complex pressure of acoustic pressure ($P \equiv p_c$)
q	tortuosity of porous medium
	quantity defined in equation (3.4) ($q_c \equiv q$)
q_c	quantity defined in equation (3.4) ($q_c \equiv q$)
Q	operator defined in equation (3.33)
Q_2	operator defined in equation (3.39)
r	horizontal distance
R	distance from source do receiver
$\mathbf{R}$	position vector
R_p	plane wave reflection coefficient
s_f	pore shape factor ratio of porous medium
S	(integration) surface
	integral number in equation (3.62)
	summand of equation (4.15)
S_c	closed surface
T	absolute temperate
T_0	constant temperature
T_t	turbulent temperature fluctuation
T^*	scaling temperature
u	wind vector of three components
u_r	horizontal wind component (cylindrical coordinate)
u_t	turbulent wind velocity fluctuation
u_z	vertical wind component (cylindrical coordinate)
u_θ	angular wind component (cylindrical coordinate)
u^*	friction velocity
V	(integration) volume
y_{max}	maximum elevation angle
z	coordinate of xyz coordinate system
z_0	roughness length of ground surface
z_{abs}	height of bottom of absorption layer in PE grid
Z_g	normalized acoustic impedance of (ground) surface
z_r	receiver height
z_s	source height
z_{top}	height of PE grid

Greek symbols

α	atmospheric absorption coefficient
	random angle for calculation of turbulent refractive index field
β	quantity defined in equation (3.28)

γ	specific heat ratio of air
Γ	gamma function
	Adiabatic correction factor
δ	Dirac delta function
δk	quantity defined in equation (4.20)
δk^2	quantity defined in equation (3.32)
Δk	wave number spacing
ΔL	relative sound pressure level
Δr	horizontal grid spacing
Δz	vertical grid spacing
ϕ	azimuthal angle
κ	von Kármán constant
λ	wave length
μ	turbulent fluctuation of acoustic refractive index n
μ_2	average refractive index n fluctuation defined in equation (3.59)
θ	reflection angle
	random angle for calculation of turbulent refractive index field
Θ	average turbulent phase fluctuation defined in equation (3.61)
Π	quantity defined in equation (4.8)
ρ	(acoustic) density of atmosphere
ρ_0	air density
σ	(effective) flow resistivity of ground
σ_v	standard deviation of wind speed fluctuations
σ_T	standard deviation of temperature fluctuations
Υ	quantity defined in equation (3.65)
ω	angular frequency
Ω	porosity of porous medium
ψ	quantity defined in equation (3.40)
ψ_M	Diabatic momentum profile correction function
ψ_H	Diabatic heat profile correction function
Ψ	Fourier transform defined in equation (3.41)
ζ	(specific) acoustic impedance of propagation medium
ζ_{air}	(specific) acoustic impedance of air
ζ_g	(specific) acoustic impedance of (ground) surface air

1 INTRODUCTION

1.1 BACKGROUND

The sound propagation studies in the atmosphere had always been a major concern in the scientific community. In the 19th century there were several isolated investigations to address specific requests, such as foghorns to aid shipping traffic or the location of artillery pieces. Refer to [Wescott & Kushner, (1965)], for a detailed bibliografy of the research done before 1965. When, in the 1960s, jet aircraft use grew significantly, governments throughout the world begun to produce specific legislation to limit the noise pollution, with the intent of protecting human health and minimizing the annoyance of noise to the communities and environment. As a result of this, new research activity grew in this area and with the aid of knowledge from other fields of physics, new methods to measure the outdoor sound propagation, with increasing accuracy, where developed.

In the last years, societies growing environmental and health conscience, obliged the national authorities to reinforce existing legislation concerning the maximum permissible noise levels, such as the Green Paper, published by the European Commission, which addressed the need for a European noise reduction policy [E. C. Environment, (1996)].

1.2 MOTIVATION

In the context described above, the knowledge of the sound propagation phenomena assumes a growing importance. Nowadays all the previous studies associated with the construction of new infrastructures or the renewing of another ones, that can generate significant levels of noise, namely airports, are mandatory. These studies must incorporate a large variety of parameters in order to reproduce the future real situation and they consume a large amount of resources to obtain accurate results, with special relevance for the financial costs associated, as well as, the long time to complete them.

The existent methods to calculate the sound level in a given atmosphere, have different degrees of complexity accuracy and speed. Some of them do not incorporate many parameters that influence the real atmospheric sound behavior or are computationally inefficient. The most relevant methods are the Generalized Fast Field Program (FFP), that do not incorporate range dependent atmospheric parameters; the Crank-Nicholson Parabolic Equation (CNPE) method, which requires significant computation time, the Ray Model method, which results are not accurate enough for some situations and the Green Function Parabolic Equation (GFPE) method.

As we will see later, the GFPE method, which was developed by [Gilbert, et al., (1993)], is the most suitable one to study the effect of wind and turbulence on sound propagation in the atmosphere. Using this method, we developed a computational program, in C language, to calculate the sound field where we included several inputs that represent the most significant parameters of sound propagation phenomena. The method puts together the best features of each of the three methods referred above

and its results were successfully validated its results by comparing it with other numerical models and existing experimental measurements.

1.3 OUTLINE

Chapter 1 of this text, introduces the problem by presenting the thesis background and aim.

Chapter 2 describes the major aspects related with sound propagation, as well as some numerical methods used to compute the sound field and their intrinsic limitations.

Chapter 3 details the GFPE as a method to solve the inhomogeneous Helmholtz equation as well as the theoretical incorporation of atmospheric turbulence.

Chapter 4 presents and explains the assumptions used to develop a C language program to calculate the sound field. This program incorporates the main parameters that govern sound propagation in a real atmosphere.

Chapter 5 presents the results and validates them by comparing with other numerical models and with existing experimental measurements.

Chapter 6 applies the developed program to an airport situation, using realistic parameters, and evaluates its results and suitability.

Chapter 7 provides a general discussion and concluding remarks of the present work, as well as, a few suggestions the author considers of interest for future developments.

2 BACKGROUND ON SOUND PROPAGATION

This chapter is a review of the most important concepts and mechanisms that control sound propagation in the atmosphere. Since the field is so vast, only the dominant mechanisms of sound propagation will be presented here. Section 2.1 gives a general view over the atmospheric acoustics, while sound propagation in a homogeneous atmosphere (section 2.2) and sound propagation in an inhomogeneous atmosphere (section 2.3) are the following two areas described in this chapter. In section 2.4 the existent numerical models to compute the sound field are briefly described.

2.1 ATMOSPHERIC ACOUSTICS

Sound is a mechanical wave, which is an oscillation of pressure transmitted through a medium, composed of frequencies within the range of hearing and with a level sufficiently strong to be heard.

A sound propagation scheme can be illustrated by a source, located at a height z_s above the ground, a receiver at a distance R from the source and placed at a height z_r, as illustrated in the following figure,

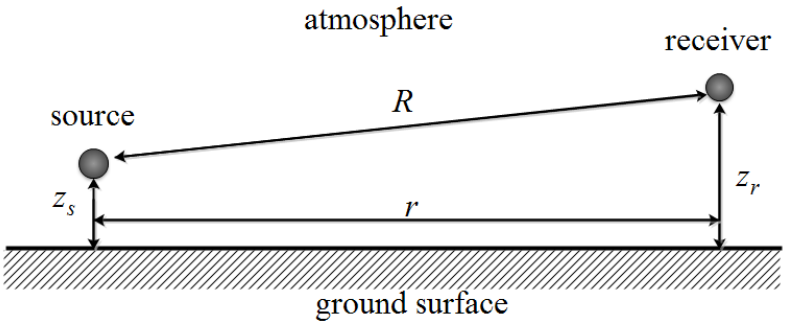

Figure 2.1 - Outdoor sound propagation basic geometry

Sound pressure in a atmosphere is the local pressure deviation from the average atmospheric pressure caused by a sound wave. The sound pressure level L_p is a logarithmic measure of the effective sound pressure of a sound relative to a reference value. Its value is measured in decibel and is given by,

$$L_p = 10log_{10}\left(\frac{1}{2}\times\frac{|p_c|^2}{\mathrm{p_{ref}}^2}\right) \tag{2.1}$$

where p_{ref} is a reference value, usually $2\times10^{-5}Pa$ and p_c is the sound pressure of a harmonic spherical wave. This reference value is considered the threshold of human hearing (at 1 kHz).

Another useful quantity used is the relative sound pressure level that can be defined as,

$$\Delta L = L_p - L_{p,free} \tag{2.2}$$

where $L_{p,free}$ is the sound pressure in a homogeneous atmosphere without a ground surface, given by,

$$L_{p,free} = 10log_{10}\left(\frac{1}{2} \times \frac{|p_{free}|^2}{\mathrm{p_{ref}}^2}\right) \tag{2.3}$$

hence, the relative sound pressure ΔL can be obtained by,

$$\Delta L = 10log_{10}\left(\frac{|p_c|^2}{|p_{free}|^2}\right) \tag{2.4}$$

However, in a benchmark point of view, the transmission loss is considered the most useful quantity for comparison purposes. The following definition is used,

$$\mathrm{TL} = 10log_{10}\left(\frac{|p_c|^2}{|p_{free}|^2_{r=1}}\right) = 10log_{10}(|p_c|^2) \tag{2.5}$$

where $|p_{free}|^2_{r=1}$ is the acoustic pressure of the direct sound field at 1 m from the source.

The two previous formulas are used later in this work to evaluate the sound levels calculated by the developed program.

2.2 SOUND PROPAGATION IN A HOMOGENEOUS ATMOSPHERE

In a homogeneous atmosphere, the medium average pressure and average density are constant. The sound wave propagation is influenced by three main phenomena:

i) spreading of sound waves,
ii) atmospheric absorption,
iii) ground absorption.

2.2.1 Geometrical spreading

As a sound wave travels out from a source with an increasing radius, the sound intensity decreases as the surface of the wave front expands. The resulting attenuation is dependent on the propagation distance, but is frequency independent. For a point source, the spreading is spherical (see Figure 2.2) and the sound level decreases 6 dB per doubling distance. On the other hand, if it is an infinite line source, the spreading of the sound waves is cylindrical (see Figure 2.2) and the sound

level drops 3 dB per doubling distance, half the rate of the spherical spreading. In both cases, those values occur if the sound propagates in a homogenous free field, i.e., with no boundaries or reflecting surfaces.

The sound emitted from a single airplane or a single vehicle can be considered as a point source, thus the spreading is spherical. By contrast, a busy highway can be comparable to a line source with cylindrical spreading, i.e., equal sound power output per unit length.

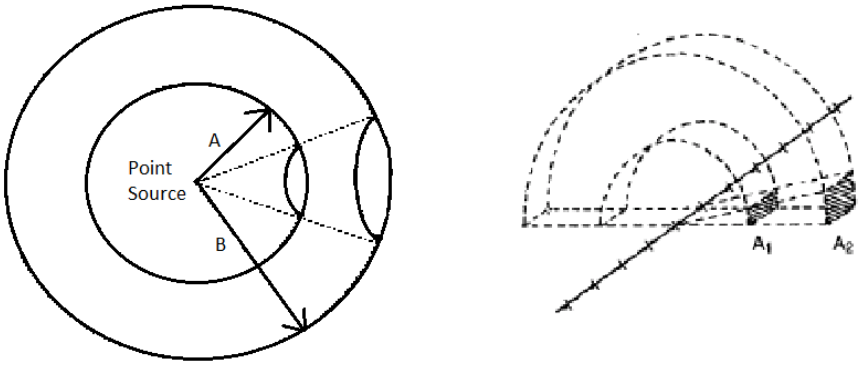

Figure 2.2 - Schematic diagram for spherical spreading (left) and cylindrical spreading (right) [Piercy, et al., (1977)]

2.2.2 Atmospheric absorption

Spreading losses represent only a reduction in the sound power per unit area as the distance of an expanding wave front increases. The real loss of sound power from the noise source is called atmospheric absorption and results from three effects:

i) Thermal conduction and viscosity of air
ii) Vibrational relaxation of molecules of air (oxygen and nitrogen)
iii) Rotational relaxation of molecules of air

this loss occurs due to the existence of small amounts of heating, viscous losses and energy exchange between air molecules, as a sound wave passes through. In this process the sound wave loses energy, which is converted into heat. Figure 2.3 shows the different physical effects and their contribution to the atmospheric absorption. It evidences that the atmospheric absorption increases mostly with the frequency of the sound wave. Meteorological effects, such as temperature, humidity and atmospheric pressure, also influence it, although in a minor level.

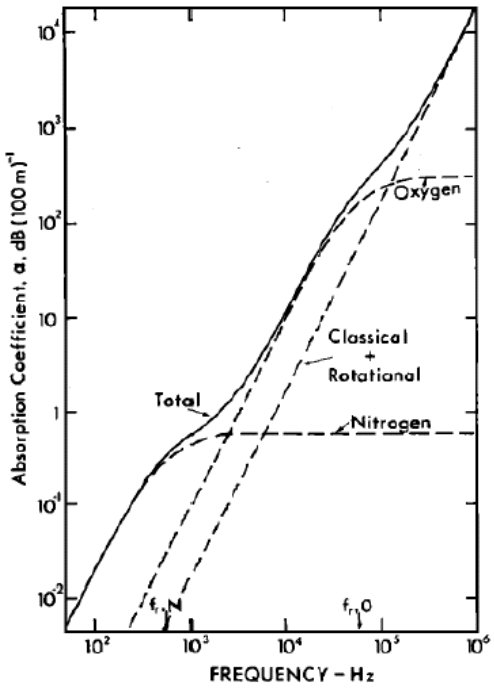

Figure 2.3 Absorption coefficient α in dB/100m as a function of frequency f, calculated for a temperature of 20 ^{o}C, relative humidity of 70 % and a pressure of 1 atm [Piercy, et al., 1977].

The attenuation by geometrical spreading, which was described in the previous section and is constant for a given ratio of propagation path lengths while, the attenuation by absorption is constant for equal propagation distance. Thus, in long range sound propagation perspective, the attenuation by absorption plays an important role, specially at high frequencies. On sound propagation at short distances, or at low frequencies, or both, the effect is small and can be neglected.

2.2.3 Ground interaction

When the source or the receiver, or both, are close to the ground, sound propagation is affected by a complex interaction of sound waves. This is the situation for most outdoor sound propagation problems, although some specific situations, such as high flying aircraft, do not have this boundary condition. When a sound wave reaches a ground surface, part of the wave is reflected back into the air and part is absorbed by the ground therefore, there are also reflected waves besides the direct sound waves (Figure 2.4).

The reflection coefficient for a plane wave on a locally reacting surface is [Salomons,(2001)],

$$R_p = \frac{Z_g \cos\theta - 1}{Z_g \cos\theta + 1} \tag{2.6}$$

and for practical situations, if both source and receiver are not in a too low position, the wave reflection coefficient can be approximated as for the case of plane waves.

The plane wave reflection coefficient R_p varies with the angle of incidence θ (Figure 2.4), but also with Z_g, which is called normalized ground impedance. This value is a complex number and can be defined as $Z_g = \zeta_g/\zeta_{air}$. The acoustic impedance, $\zeta = p_c/v_c$, is the ratio of the complex pressure and the amplitude of the speed of an acoustic wave traveling through a medium. For an acoustically hard surface, like water or concrete, we have $Z_g = \infty$. An acoustically absorbing ground, like grassland, has a finite value of ground impedance.

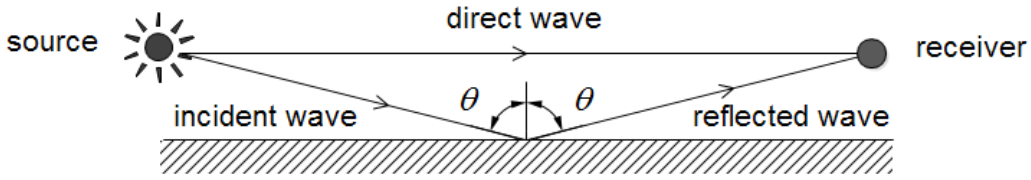

Figure 2.4 Reflection of a sound wave on a flat reacting ground surface

Various accurate models for the impedance calculation of porous materials were developed by [Zwikker, et al., (1949)], [Delany, et al., (1970)] and [Attenborough, (1985)], each of them depending on the frequency of the source and of the type of ground material. They are based on different theoretical models and differ on the number of ground parameters used. For the computational program developed in this thesis, we adopt the Attenborough's four parameter model. Its normalized ground impedance is defined as [Attenborough, (1985)]:

$$Z_g = \left(\frac{4q^2}{3\Omega} + i\frac{s_f^2\sigma}{\rho\omega}\right)\frac{\omega/c}{k} \tag{2.7}$$

being the wave number:

$$k = \frac{\omega}{c}\sqrt{\gamma\Omega}\sqrt{\left(\frac{4}{3} - \frac{\gamma-1}{\gamma}N_{pr}\right)\frac{q^2}{\Omega} + i\frac{s_f^2\sigma}{\rho\omega}} \tag{2.8}$$

where the constant $N_{pr} \approx 0.7$ is the Prandtl number, σ is the flow resistivity, Ω is the porosity, g is a grain shape factor, s_f is the pore shape factor ratio and $q^2 \equiv \Omega^{-g}$ is the square of the tortuosity. By adjusting these four parameters, different types of ground surfaces can be simulated for a given frequency.

2.3 SOUND PROPAGATION IN AN INHOMOGENEOUS ATMOSPHERE

In an inhomogeneous atmosphere, the fluid pressure, density and speed are function of position. By this reason, the meteorological modeling of an atmosphere is very complex, depending on many variables such as temperature, wind speed and direction, air pressure and density. The following two sections describe two phenomena that affect sound propagation: atmospheric refraction and turbulence.

2.3.1 Atmospheric refraction

Atmospheric refraction can be described as the change of the sound wave propagation direction caused by the atmosphere sound speed gradient. For small distances between the source and the receiver, up to 100 m in an open area, atmospheric refraction can be ignored. Thus, to simplify calculations, a non-refracting or homogenous environment can be adopted. For distances larger than 100m, the influence of temperature and wind gradients on sound level is significant, particularly if both the source and the receiver are close to the ground surface. Most problems deal with outdoor long range propagation so the latter situation is more common. Being aware of that, the computational model developed in this thesis will incorporate atmospheric refraction.

The sound speed in the atmosphere change as a function of the temperature T and is defined by,

$$c = c_0 \sqrt{\frac{T}{T_0}} \tag{2.9}$$

where T is the temperature in Kelvin, c_0 is the sound speed at the temperature T_0 (commonly, $c_0 = 343\ m/s$ and $T_0 = 293\ K$).

The sound propagation speed depends on the air temperature: higher temperature yields faster sound propagation. During daylight, solar radiation heats the earth´s surface resulting in a warmer air temperature close to the ground. This occurrence is called temperature lapse (Figure 2.5).

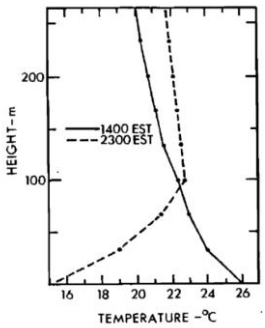

Figure 2.5 Variation of temperature with height; examples of lapse (solid line) and inversion (dashed line) conditions from [Munn, (1966)]

Due to this event, the sound wave travelling close to the ground propagates faster than the sound wave travelling more distant of the ground. Furthermore, the existence of a temperature gradient causes successive refractions of the sound wave and a consequent change of direction, bending upwards as shown in Figure 2.6 . This will create a shadow zone where the sound pressure is zero and the ray delimiting this area is tangent to the ground surface. In reality the pressure is small because of the of the atmospheric turbulence scattering effect as discussed in section 6.4.

During the night, the ground cools by radiation faster than the atmosphere (Figure 2.5). This causes the sound wave to change direction and bend downwards. This phenomenon is known as inversion and is illustrated in Figure 2.6.

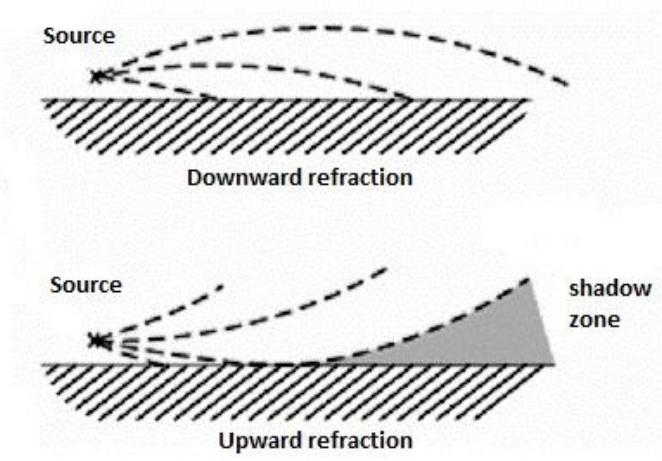

Figure 2.6 Top: illustration of downward refraction of sound. Bottom: illustration of upward refraction of sound [Piercy, et al., (1977)].

In the examples above, the atmosphere was considered non-moving, i.e., without wind. Conversely, an atmosphere with wind is called a moving atmosphere. Refraction caused by temperature is identical in all directions because it is a scalar quantity. However, refraction caused by wind depends on the sound direction of propagation. A vector of three components represents the wind in the atmosphere,

$$u(r, \theta, z) = (u_r, u_\theta, u_z) \tag{2.10}$$

where r, θ and z form the three coordinates of a cylindrical coordinate system.

Considering that the computational method developed in this work is two dimensional, only r and z coordinates, the same ones represented on Figure 2.1, were considered. As a result, if the sound propagates directly crosswind (perpendicular to the wind path), the refraction component caused by wind is zero. The vertical component u_z is much smaller than u_r, therefore can be neglected [Salomons, (2001)]. We can then approximate a moving atmosphere to a non-moving atmosphere, with an effective sound speed using,

$$c_{eff} = c + \|\vec{u}\| \approx c + u_r \tag{2.11}$$

where c is the adiabatic sound speed and u_r is the component of the wind speed in the direction of sound propagation. If the wind blows in the direction opposite to the sound propagation, it has a negative contribution to the sound speed and the sound rays are bent away from the ground. It results in upward refraction, just as the effect of the temperature lapse in Figure 2.6. Downward refraction occurs if the wind blows in the same direction.

The wind speed is approximately zero near the ground, due to friction over the ground surface and its value usually increases with altitude. The type of ground dictates the wind speed close to it: rough surfaces, such as grassland, cause the wind to slow down more, in comparison with smooth surfaces, like water.

A logarithmic function is frequently used to simulate a realistic atmosphere:

$$c_{eff}(z) = c_0 + b \ln\left(\frac{z}{z_0} + 1\right) \tag{2.12}$$

where c_0 is the sound speed at the ground surface, the parameter z_0 is the roughness length and b is the refraction velocity. Positive values of b represent a downward refracting atmosphere and conversely, negative values represent an upward reflecting atmosphere. Section 6 describes how to obtain realistic profiles of temperature and wind speed by adjusting the parameters of a logarithmic function. This profile is an accurate representation of the sound speed profile and is used, for benchmarking purposes, in the computational program developed in this thesis.

2.3.2 Atmospheric turbulence

In the previous section, the atmosphere was characterized by vertical profiles of both temperature and wind. These profiles were assumed to be average values over a period of time, typical over 10 minutes. However, in a real atmosphere, the profiles change continuously. These fluctuations can occur in a scale of several hours or longer, but also occur in much faster scales, of seconds or minutes. The latter fluctuations are known as atmospheric turbulence.

Two types of flow exist in fluid dynamics: laminar and turbulent. Laminar flow occurs when a fluid travels smoothly or in regular paths, without any disruption between them. This type of flow is the least common in most aerodynamics problems, and is usually present in low velocity flow or when the flow section is relatively small (Figure 2.7). If the flow speed increases, the fluid transits into a new state characterized by chaotic and stochastic property changes, called turbulent flow.

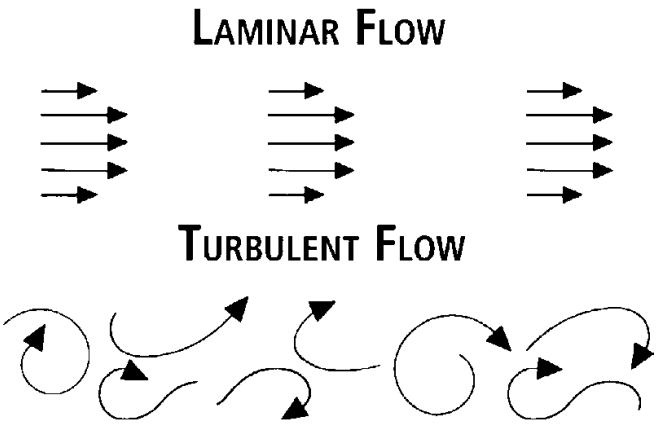

Figure 2.7 Top: Illustration of laminar flow. Bottom: Illustration of turbulent flow

The fluid currents in a turbulent flow often differ from the general flow direction, forming swirls in the fluid, which are called eddies (Figure 2.7). The eddies size in a turbulent flow depend on the characteristic dimension of it. In the atmospheric boundary layer, eddies size increase with ground distance. Although the eddies process formation is a continuous one, its constant instability induces them to break down continuously into smaller sizes until the energy is completely dissipated by viscosity. By that reason, there is a large spectrum of eddy sizes in the atmosphere. These motions span a broad spectrum of spatial scales from millimeters to kilometers [Kaimal, et al., (1994)]. Although its complexity and associated computational effort, the incorporation of atmospheric turbulence is essential nowadays to correctly evaluate the sound propagation in the atmosphere.

2.4 NUMERICAL MODELS

2.4.1 Fast Field Program (FFP)

The Fast Field Program was originally developed as a computational method for underwater acoustics [Dinapoli, et al., (1979)] and [Jensen, et al., (1994)]. Later on, this method was adapted for outdoor sound propagation in the atmosphere [Lee, et al., (1986)] and [Raspet, et al., (1985)]. This computer model permits the prediction of sound pressure in a layered refracting atmosphere, with arbitrary position for both source and receiver, above an absorbing or rigid ground surface. The atmosphere is divided in horizontal homogenous layers where each one has its own wave number, i.e., with constant wind speed and temperature (see Figure 2.8).

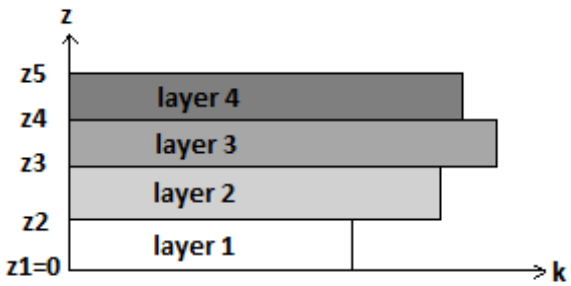

Figure 2.8 - Representation of a stratified atmosphere for the FFP method, where each layer has its own wave number k [Salomons, (2001)].

The sound field is computed in the horizontal wave number domain and to calculate it, a Fourier transformation of the wave equation is used, from the horizontal spatial domain to the wave number domain. This is necessary to solve numerically the wave equation. Thereafter, an inverse Fourier transform is used to obtain the sound field in the spatial domain, back from the horizontal wave number domain. Since only one frequency is obtained per sound field calculation, computing an entire frequency spectrum is very time consuming. This method is sometimes called “wave number integration method”, since the sound field is computed in the horizontal wave number domain. The FFP is restricted to simulations where the sound speed profile and ground surface are constant through each horizontal layer (Figure 2.8). This reduces the complexity of the environments which can be simulated, not only for both range dependent wind and temperature gradients, but also for atmospheric turbulence. Additionally, this method is limited to either flat topography or single large scale topographical feature, as for example a large hill, with constant ground impedance value.

However, despite these limitations, this model can calculate the sound field in a moving atmosphere, with realistic vertical wind and temperature gradients and has a speed advantage in long range calculations. It is important to note that, for homogenous atmospheres or linear sound speed profiles, the wave number equation can be solved analytically [Salomons, (2001)]. This is an important feature of this method, as it can be used to test the accuracy of other numerical methods.

2.4.2 Parabolic equation method

The Parabolic Equation (PE) method is a computational model based on a parabolic equation, which is an approximate form of the wave equation. It was developed initially for electromagnetic wave propagation on the earth’s surface by [Lentovich, et al., (1946)].

It is a step by step solution that uses a two dimensional grid (see Figure 2.9), where the source is at $r = 0$ with an arbitrary vertical position z, and sequentially solves the respective parabolic wave equation. The solution is usually computed in two dimensions to reduce the computational burden. This approach is based on an axisymmetric approximation and is described in section 3.1.

With this method, it is possible to change the sound speed gradient and the ground impedance along the route of propagation thus, it is also possible to include range dependent atmospheric conditions and more specifically, a turbulent atmosphere. Changing topography and obstacles, like barriers, are also feasible to implement. Hence, the PE method is more flexible than the FFP method in predicting real ground and climacteric conditions.

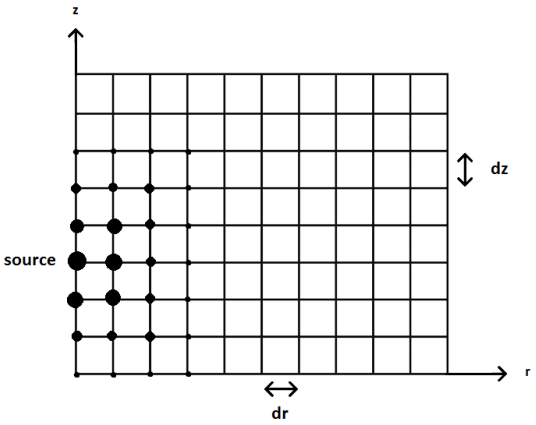

Figure 2.9 - Grid on the rz plane used in the two dimensional PE models [Salomons, (2001)].

As mentioned above, the parabolic equation is an approximation of the wave equation. There are different types of parabolic equations, each of them having a specific maximum elevation angle γ_{max}. This is the reason why the PE method is only valid up to a certain elevation angle. Thus, the sounds levels are only valid for receivers with elevation angles smaller than γ_{max} (see Figure 2.10) and consequently, for a given source, there is an area where the results are accurate.

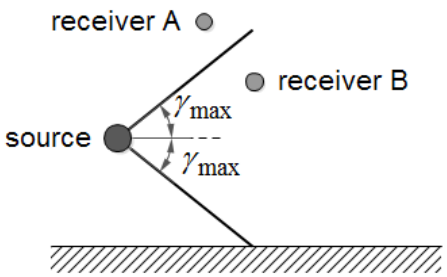

Figure 2.10 - Representation of the angular limitation of the PE method.

In Figure 2.10, the receiver A is outside the area defined by γ_{max}, so the results are not accurate. On the other hand, the receiver B is inside this area, where the sound levels are valid. For most outdoor sound propagation problems, both the source and the receiver are close to the ground, or the distance between them is large enough to minimize the influence of this limitation.

The parabolic equation is a one-way wave equation, thus the sound from a source is always directed outwards. This results in the absence of back scattering of sound waves but, as the sound speed profiles are commonly a smooth function of position, sound waves travel mostly from the source to the receiver.

There are two major methods for solving the parabolic equation: the Crank-Nicholson Parabolic equation (CNPE) method and the Green's Function Parabolic equation (GFPE) method. They are summarized in the two sections below.

2.4.2.1 Crank-Nicholson Parabolic Equation method

In this section, a summarized description of the Crank-Nicholson Parabolic Equation (CNPE) method, developed by [Gilbert, et al., (1989)], is presented. For a detailed description of this method, refer to [West, et al., (1992)]. As mentioned in the previous section, the CNPE is based in an approximation of the wave number equation, which, in this case, can be either a narrow-angle or an wide-angle parabolic equation. The accuracy in each approximation is guaranteed for $y_{max} = 15^{\circ}$ or $y_{max} = 35^{\circ}$, respectively (Figure 2.10). In each extrapolation step, the parabolic equation is solved numerically by approximating the wave equation derivates, by a finite difference Crank-Nicholson scheme. The horizontal and vertical grid spacing, which is used to build the two dimensional grid, as the one illustrated in Figure 2.9, have a maximum value of about $\lambda/10$, where λ is the average wavelength. This maximum value limitation is necessary to assure that each range integration accounts for each oscillation of the sound field, and consequently, the sound level accuracy. The grid spacing varies with source frequency: the higher the frequency, the lower the grid spacing. This result has some implications, in particular with the horizontal range step Δr. In a situation with high source frequency or long range propagation, the number of extrapolation steps required can be very high. This problem is mitigated with the Green's Function Parabolic Equation (GFPE) method, which is briefly described in the following section.

2.4.2.2 Green's Function Parabolic Equation Method

The GFPE method, which was developed by [Gilbert, et al., (1993)], is another method to solve a parabolic wave equation and the one used in this thesis' computational program. A Green function is applied to solve the inhomogeneous wave equation, in a rectangular grid like the one in Figure 2.9. The sound field is computed in the vertical wave number domain, so two Fourier transforms are used. The first one transforms the spatial domain into the vertical wave number domain, while the second one changes back to the spatial domain. This method analytically takes into account the horizontal wave oscillations in the field, which allows large horizontal extrapolation steps (up to 50 wavelengths [Gilbert, et al., (1993)]). Consequently, the horizontal spacing Δr is significantly larger than the vertical spacing Δz, which is about the same as the one used in the CNPE method ($\lambda/10$). Therefore, this method is significantly faster than the PE algorithms that use the Crank-Nicolson scheme, and

provides faster calculations of entire frequency spectrums, real-time predictions on home computers and practical three dimensional calculations.

These characteristics make the GFPE method the appropriate choice for an atmospheric computational program, combining the superior real atmosphere modeling of the PE method, with the faster long range calculations of the FFP method.

2.4.3 Ray Model

The sound propagation in the atmosphere can be computed using a ray sound model. This model is also called geometrical acoustics and has two steps:

i) calculation of the paths of all rays, direct or reflected, between the source and the receiver
ii) calculation of the received sound pressure by the contributions of all sound rays.

In a homogenous atmosphere with a ground surface, two ray paths are required to calculate the sound pressure. The first path represents the direct ray and the second term represents the ray reflected by the ground. The sound levels obtained are an exact solution and consequently, can be used to validate more complex computational models.

Homogenous atmosphere is only valid for small propagation distances. For propagation distances larger than 100 meters, atmospheric refraction must be taken into account. In a refractive atmosphere, the sound paths curve and multiple reflections can occur then, the number or rays from a source to a receiver, is usually larger than two. The number of rays increases with the distance between the source and the receiver, making this model less suitable for long range sound propagation. The calculation of all ray paths is called 'ray tracing' . An interactive computational algorithm is necessary to map all ray paths, from the source to the receiver.

Another usual problem related with this model derives from the fact that two rays, with infinitesimal difference in elevation, can be recognized by the algorithm as a caustic point. In this situation, geometrical acoustics predicts an infinite amplitude of the sound pressure. To overcome this limitation, a complex computational method is used, which makes the ray model less attractive for accurate calculations of sound propagation.

Different computational algorithms were developed to map efficiently all ray paths, as well as to solve the caustic point’s problem, [Salomons, (1998)] and [Gabillet, et al., (1993)].

3 THEORETICAL FORMULATION

Starting from the inhomogeneous Helmholtz equation in the spatial domain, we describe how to obtain the basic equations of the two-dimensional GFPE method, as well as how to incorporate atmospheric turbulence.

3.1 INHOMOGENEOUS HELMHOLTZ EQUATION

Considering a system with a monopole source, in a moving atmosphere with a non constant sound speed profile, the governing Helmholtz equation in the spatial domain is,

$$k_{eff}^2 \nabla\left(\frac{1}{k_{eff}^2}\nabla p_c\right) + k_{eff}^2 p_c = 0 \tag{3.1}$$

where $p_c(\boldsymbol{R})$ is the complex pressure amplitude, $\boldsymbol{R}$ is a three dimensional position vector and k_{eff} is the effective wave number. The Helmholtz equation 3.1 is deduced in detail in [Salomons, (2001)].

As described in section 2.3.1, a moving atmosphere is simulated with a non moving atmosphere with an effective sound speed k_{eff} , defined as,

$$k_{eff} = \frac{\omega}{c_{eff}} \tag{3.2}$$

ω being the angular frequency and c_{eff} is the effective sound speed as defined by equation (2.11).

Since most sound propagation computational programs, in particular the one developed in this text, use a two-dimensional representation of the atmosphere, an aproximation of the three-dimensional Helmholtz equation is required [Gilbert, et al., (1993)]. Using a cylindrical coordinate system (r, ϕ, z), with r and z as shown in Figure 2.9 and ϕ the azimuthal angle, equation (3.1) becomes,

$$\frac{1}{r}\frac{\partial}{\partial r}\left(r\frac{\partial p_c}{\partial r}\right) + k_{eff}^2 \frac{\partial}{\partial z}\left(\frac{1}{k_{eff}^2}\frac{\partial p_c}{\partial z}\right) + \frac{1}{r^2}\frac{\partial^2 p_c}{\partial \phi^2} + k_{eff}^2 p_c = 0 \tag{3.3}$$

In the approximation, it is assumed that the system has azimuthal symmetry about the vertical axis z, therefore, the third term on the left-hand side of equation (3.3) can be neglected. Also a variable $q_c = p_c\sqrt{r}$ is defined, which removes the cylindrical spreading. Replacing into equation (3.3), the resulting far-field equation ($r \gg k_{eff}^{-1}$) is,

$$\frac{\partial^2 q_c}{\partial r^2} + k_{eff}^2 \frac{\partial}{\partial z}\left(\frac{1}{k_{eff}^2}\frac{\partial q_c}{\partial z}\right) + k_{eff}^2 q_c = 0 \tag{3.4}$$

where the second term can be approximated by,

$$k_{eff}^2 \frac{\partial}{\partial z}\left(\frac{1}{k_{eff}^2}\frac{\partial q_c}{\partial z}\right) \approx \frac{\partial^2 q_c}{\partial z^2} \tag{3.5}$$

Numerical computations show that this approximation is suitable for the majority of numerical applications [Salomons, (2001)]. With $k_{eff} \equiv k$ and $q_c \equiv q$, equation (3.4) becomes,

$$\frac{\partial^2 q}{\partial r^2} + \frac{\partial^2 q}{\partial z^2} + k^2 q = 0 \tag{3.6}$$

with $q = q(r, z)$ and $k = k(z)$. Equation (3.6) is used to obtain the equations of the GFPE method.

3.2 KIRCHHOFF-HELMHOLTZ INTEGRAL EQUATION

Considering an inhomogeneous fluid with a volume V, enclosed by a surface S with an outward normal pointing vector $\mathbf{n}$ and giving an acoustic wave field $P(\boldsymbol{R})$, radiated by sources outside the surface S, the wave field $P(\mathbf{R_A})$ at a point $\mathbf{R_A} = (x_1, y_1, z_1)$ can be computed from $P(\mathbf{R})$ with the Kirchhoff-Helmholtz integral equation. In other words, it states that if the sound pressure is determined in all points on its surface, the sound pressure inside the volume free of sources can be also calculated (see Figure 3.1).

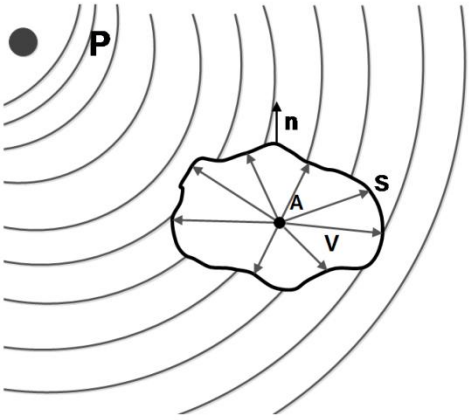

Figure 3.1 - Example of a geometry for the Kirchhoff-Helmholtz integral

The Kirchhoff-Helmholtz integral can be expressed as [Salomons, (2001)], [Morse, et al., (1953)],

$$P(\mathbf{R_A}) = -\frac{1}{4\pi}\oint_S [P(\mathbf{R})\nabla G(\mathbf{R}, \mathbf{R_A}) - G(\mathbf{R}, \mathbf{R_A})\nabla P(\mathbf{R})] \cdot \mathbf{n}\, dS \tag{3.7}$$

where the integral is over $\mathbf{R} = (x, y, z)$ on the surface S.

The acoustic wave field $P(\mathbf{R})$ satisfies in V the two-way wave equation,

$$\nabla^2 P(\mathbf{R}) + k^2(\mathbf{R}) P(\mathbf{R}) = 0 \tag{3.8}$$

Likewise, the Green's function $G(\mathbf{R}, \mathbf{R_A})$ satisfies in V the inhomogeneous wave equation with a point source at $\mathbf{A}$,

$$\nabla^2 G(\mathbf{R}, \mathbf{R_A}) + k^2(\mathbf{R}) G(\mathbf{R}, \mathbf{R_A}) = -4\pi\delta(\mathbf{R} - \mathbf{R_A}) \tag{3.9}$$

with $\delta(\mathbf{R} - \mathbf{R_A}) = \delta(x - x_1) \times \delta(y - y_1)$ being the product of two Dirac delta functions.

Therefore, the Green's function can be explained as the spatial impulse response of the medium in the volume V. Equation (3.7) can be proved using the two above equations and the divergence theorem.

The two dimensional Kirchhoff-Helmholtz equation can be obtained from equation (3.7), assuming that the wave field $P(\mathbf{R})$ is independent of the y coordinate,

$$P(\mathbf{r_A}) = -\frac{1}{4\pi} \int_C [P(\mathbf{r}) \nabla g_2(\mathbf{r}, \mathbf{r_A}) - g_2(\mathbf{r}, \mathbf{r_A}) \nabla P(\mathbf{r})] \cdot \mathbf{n}\, ds \tag{3.10}$$

where, $\mathbf{r_A} = (x, z)$, the integral is over positions $\mathbf{r} = (x, z)$ on the closed contour C, which encloses the area S_c, and $g(\mathbf{r}, \mathbf{r_A})$ is a two dimensional Green's function.

Similarly, equation (3.8) gives the two-dimensional Helmholtz equation,

$$\nabla^2 P(\mathbf{r}) + k^2(\mathbf{r}) P(\mathbf{r}) = 0 \tag{3.11}$$

The two dimensional Green's function $g_2(\mathbf{r}, \mathbf{r_A})$ satisfies in S_c the inhomogeneous wave equation with a point source at $\mathbf{A}$ and is obtained integrating equation (3.9) from $y = -\infty$ to $y = +\infty$,

$$\nabla^2 g_2(\mathbf{r}, \mathbf{r_A}) + k^2(\mathbf{r}) g_2(\mathbf{r}, \mathbf{r_A}) = -4\pi\delta(\mathbf{r} - \mathbf{r_A}) \tag{3.12}$$

In the geometry of Figure 3.2, the closed contour C consists of the arc C_1 with R radius and the segment C_0 at $x = x_0$. The contribution of the Kirchhoff-Helmholtz integral (equation 3.10) over C_1 to the pressure in $\mathbf{A}$ vanishes if R goes to infinity. The Green's function choice is important as it must have a contribution from a source at $\mathbf{r_A}$, in order to satisfy equation (3.12). Additional contribution from sources outside the contour C can also be added to the Green's function. If these contributions are two monopole sources placed symmetrically with respect to $x = x_0$, in points r_A and r_B , its value is,

$$g_2(\mathbf{r}, \mathbf{r_A}) = g(\mathbf{r}, \mathbf{r_A}) - g(\mathbf{r}, \mathbf{r_B}) \tag{3.13}$$

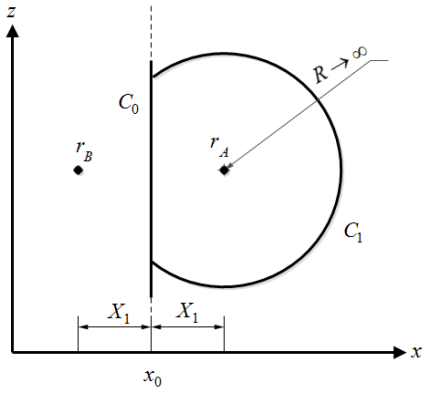

Figure 3.2 - Geometry for the two-dimensional Kirchhoff-Helmholtz integral

With the two monopole sources, $g_2 = 0$ on C_0 and the contour C only consists in the line segment C_0. Equation (3.10) results,

$$P(\mathbf{r_A}) = -\frac{1}{4\pi}\int_{-\infty}^{\infty}\left(P(\mathbf{r})\nabla g_2(\mathbf{r}, \mathbf{r_A})\right)_{x=x_0} \cdot \mathbf{n}\, dz \tag{3.14}$$

where, $\nabla g_2(\mathbf{r}, \mathbf{r_A}) \cdot \mathbf{n} = -2\frac{\partial g}{\partial x}$ from equation (3.13). The equation above becomes,

$$P(\mathbf{r_A}) = \frac{1}{2\pi}\int_{-\infty}^{\infty}\left(P(\mathbf{r})\frac{\partial g(\mathbf{r}, \mathbf{r_A})}{\partial x}\right)_{x=x_0} dz \tag{3.15}$$

This integral is known in acoustics as the Rayleigh II integral [Pierce, (1991)].

3.3 GENERAL GREEN'S FUNCTION METHOD

Returning to the notation used in section 3.1, equation (3.15) results,

$$q(\mathbf{R_A}) = \frac{1}{2\pi}\int_{0}^{\infty}\left(q(\mathbf{R})\frac{\partial g(\mathbf{R}; \mathbf{R_A})}{\partial r}\right)_{r=r_0} dz \tag{3.16}$$

where $\mathbf{R_A} = (r_{A,} z_A)$, $\mathbf{R} = (r, z)$ and the ground surface is located at $z = 0$.

The Green's function $g(\mathbf{R}, \mathbf{R_A})$ also satisfies the two-dimensional Helmholtz equation and can be written as follows,

$$\left(\frac{\partial^2}{\partial r^2} + \frac{\partial^2}{\partial z^2} + k^2(z)\right) g(\mathbf{R}, \mathbf{R_A}) = -4\pi\delta(\mathbf{R} - \mathbf{R_A}) \tag{3.17}$$

Here is assumed that the medium is independent of the horizontal distance r ($k = k(z)$), so the range dependence is taken into account by changing k between sequential horizontal steps and g can be written as $g(\Delta r, z, z_A)$, with $\Delta r = r_A - r$ as the horizontal spacing. To express the Green's function in terms of the horizontal wave number k_h, the following Fourier transform is introduced,

$$G(k_h, z, z_A) = \int g(\Delta r, z, z_A) e^{-ik_h \Delta r}\, d\Delta r \tag{3.18}$$

The inverse Fourier transform formula,

$$g(\Delta r, z, z_A) = \frac{1}{2\pi} \int G(k_h, z, z_A) e^{ik_h \Delta r}\, dk_h \tag{3.19}$$

is now substituted in equation (3.16), with $r_A = \Delta r + r$ and $\partial_r = -\partial_{\Delta r}$. Taking into account Fourier transform properties, equation (3.16) results (changing the notation from z to z_A and from z' to z),

$$q(\Delta r + r, z) = \frac{1}{4i\pi^2} \int_{-\infty}^{\infty} k_h e^{ik_h \Delta r} dk_h \int_0^{\infty} G(k_h, z', z)\, q(r, z') dz' \tag{3.20}$$

The previous expression can also be derived from the spectral theorem of functional analysis [Gilbert, et al., (1993)]

The Green's function $G(k_r, z', z)$ also satisfies the transformed version of the Helmholtz equation [equation (3.17)] and is obtained as follows,

$$\begin{aligned} \int_{-\infty}^{\infty} \left[\left(\frac{\partial^2}{\partial r^2} + \frac{\partial^2}{\partial z^2} + k^2(z) \right) g(r, z; r_A, z_A) e^{-ik_h \Delta r} \right] d\Delta r \\ = -4\pi \int_{-\infty}^{\infty} \delta(\Delta r) \times \delta(z - z_A)\, e^{-ik_h \Delta r} d\Delta r \end{aligned} \tag{3.21}$$

applying the Fourier transform properties and changing the notation from z_A to z and from z' to z, it reduces to,

$$\left(\frac{\partial^2}{\partial z^2} - {k_h}^2 + k^2(z) \right) G(k_h, z', z) = -4\pi \delta(z - z') \tag{3.22}$$

3.4 CONSTANT SOUND SPEED PROFILE

For a constant vertical sound speed $k(z) = k_0$, where k_0 is the wave number at zero height, the solution of equation (3.22) with a surface impedance boundary condition is [Gilbert, et al., (1993)],

$$G(k_h, z', z) = \frac{2\pi i}{k_v}\left[e^{ik_v|z-z'|} + R(k_v)e^{ik_v(z+z')}\right] \tag{3.23}$$

being k_v the vertical wave number defined by,

$$k_v^2 = k^2(z) - k_h^2 \tag{3.24}$$

and being $R_p(k_v)$ the plane wave reflection coefficient defined in equation (2.6). From Figure 2.4, $\cos(\theta) = k_v/k_0$, thus equation (2.1) becomes,

$$R_p(k_v) = \frac{k_v Z_g - k_0}{k_v Z_g + k_0} \tag{3.25}$$

where Z_g is the normalized ground impedance described in section 2.2.3.
Substituting equation (3.23) in equation (3.20) results,

$$\begin{aligned} q(r + \Delta r, z) = \frac{1}{\pi i}\int_{-\infty}^{\infty} k_h e^{ik_h \Delta r} dk_h \int_0^{\infty} \frac{i}{2k_v}\left[e^{ik_v|z-z'|}\right. \\ \left. + R_p(k_v)e^{ik_v(z+z')}\right] q(r, z')dz' \end{aligned} \tag{3.26}$$

To get an equivalent Fourier transform that uses the vertical wave number, two identities are introduced [Gilbert, et al., (1993)],

$$\frac{i}{2k_v}\left(e^{ik_v|z-z'|}\right) \equiv \frac{1}{2\pi}\int_{-\infty}^{\infty} \frac{e^{ik_z(z-z')}}{k_z^2 - k_v^2} dk_z \tag{3.27}$$

and

$$\frac{i}{2k_v} R_p(k_v)\left(e^{ik_v|z+z'|}\right) \equiv \frac{1}{2\pi}\int_{-\infty}^{\infty} R_p(k_z) \frac{e^{ik_z(z+z')}}{k_z^2 - k_v^2} dk_z + 2i\beta \frac{e^{-i\beta(z+z')}}{\beta^2 - k_v^2} \tag{3.28}$$

where $\beta = k_0/Z_g$ is the surface wave pole in the reflection coefficient. [Salomons, (2001)] describes with detail, using the residue theorem, the proof for both identities.

Applying these identities to equation (3.26) and rearranging the integration order,

$$\begin{aligned} q(r + \Delta r, z) = {} & \frac{1}{2\pi}\int_{-\infty}^{\infty} e^{izk_z} dk_z \int_0^{\infty} e^{-iz'k_z} q(r, z')dz' \frac{1}{\pi i}\int_{-\infty}^{\infty} \frac{e^{ik_h \Delta r}}{k_z^2 - k_v^2} k_h dk_h \\ & + \frac{1}{2\pi}\int_{-\infty}^{\infty} R_p(k_z) e^{izk_z} dk_z \int_0^{\infty} e^{iz'k_z} q(r, z')dz' \frac{1}{\pi i}\int_{-\infty}^{\infty} \frac{e^{ik_h \Delta r}}{k_z^2 - k_v^2} k_h dk_h \\ & + 2i\beta e^{-i\beta z}\int_0^{\infty} e^{-i\beta z'} q(r, z')\, dz' \frac{1}{i\pi}\int_{-\infty}^{\infty} \frac{e^{ik_h \Delta r}}{\beta^2 - k_v^2} k_h dk_h \end{aligned} \tag{3.29}$$

Using the residue theorem and equation (3.24), the two first integrals over the horizontal wave number k_h result,

$$\frac{1}{\pi i}\int_{-\infty}^{\infty}\frac{e^{ik_h\Delta r}}{k_z^2-k_v^2}k_h dk_h=\frac{1}{\pi i}\int_{-\infty}^{\infty}\frac{e^{ik_h\Delta r}}{k_h^2+k_z^2-k_0^2}k_h dk_h=e^{i\Delta r\sqrt{k_0^2-k_z^2}} \tag{3.30}$$

The integral over k_h in the third term on the right hand side of equation (3.29) is evaluated with the same method, with k_z replaced by β. Equation 3.29 becomes,

$$\begin{aligned} q(r+\Delta r,z)=&\frac{1}{2\pi}\int_{-\infty}^{\infty}e^{i\Delta r\sqrt{k_0^2-k_z^2}}e^{izk_z}dk_z\int_0^{\infty}e^{-iz'k_z}q(r,z')dz' \\ &+\frac{1}{2\pi}\int_{-\infty}^{\infty}R_p(k_z)e^{i\Delta r\sqrt{k_0^2-k_z^2}}e^{izk_z}dk_z\int_0^{\infty}e^{iz'k_z}q(r,z')dz' \\ &+2i\beta e^{-i\beta z}e^{i\Delta r\sqrt{k_0^2-\beta^2}}\int_0^{\infty}e^{-i\beta z'}q(r,z')\,dz' \end{aligned} \tag{3.31}$$

The above equation represents the sum of three different types of sound waves. The first term represents the direct wave, the second term represents the wave reflected by the ground and the third term represents the surface wave. Equation (3.31) is the basic equation for the GFPE method with a non-refracting atmosphere. In the next section, atmospheric refraction is included.

3.5 NON-CONSTANT SOUND SPEED PROFILE

In the previous section, the equation for the GFPE method with a non-refracting atmosphere was calculated. In this section, an equation for a refractive atmosphere is presented. The variation in each horizontal range step is small enough to assume that the wave number is only a function of height z, therefore its value is,

$$k^2(z)=k_a^2+\delta k^2(z) \tag{3.32}$$

where k_a is a constant wave number at some average height. Usually it takes the correspondent value at the ground surface $k_a=k(0)$. The second term on the right-hand side of equation (3.32) is the variation of the vertical profile, which can be either positive or negative and it is always small compared with $k^2(z)$.

Equation (3.6) can be written as,

$$\frac{\partial^2}{\partial r}q(r,z)+Qq(r,z)=0 \tag{3.33}$$

where the operator Q is defined as $Q=k^2(z)+\partial_z^2$ and it was assumed that k is independent of range.

Two-way wave propagation is described by,

$$\frac{\partial q(r,z)}{\partial r} = \pm i\sqrt{Q}\,q(r,z) \tag{3.34}$$

where the positive sign refers to waves travelling to the positive direction of r, and the negative sign applies to waves travelling to the negative direction of r. With the r dependence in q written explicitly and the z dependence implicit, the above equation results,

$$q(r+\Delta r) = e^{i\Delta r\sqrt{Q}}q(r) \tag{3.35}$$

For a refracting atmosphere, the operator Q is,

$$Q = \partial_z^2 + k_a^2 + \delta k^2(z) \tag{3.36}$$

The square root of the Q operator can be approximated as [Gilbert, et al., (1993)],

$$\sqrt{Q} = \sqrt{\partial_z^2 + k_a^2 + \delta k^2(z)} \approx \sqrt{\partial_z^2 + k_a^2} + \frac{\delta k^2(z)}{2k_a} \tag{3.37}$$

An alternative approximation of the square root operator is described in section 4.2.3. Substituting the above equation into the one-way equation (3.35) results,

$$q(r+\Delta r) = \exp\left[i\Delta r\left(\sqrt{\partial_z^2 + k_a^2} + \frac{\delta k^2(z)}{2k_a}\right)\right] q(r) \tag{3.38}$$

assuming that $\sqrt{\partial_z^2 + k_a^2}$ commutes with $\delta k^2(z)/2k_a$, equation (3.38) is approximately,

$$q(r+\Delta r) \approx \exp\left(i\Delta r\frac{\delta k^2(z)}{2k_a}\right)\exp\left(\, i\Delta r\sqrt{Q_2}\right)q(r) \tag{3.39}$$

where $Q_2 = \partial_z^2 + k_a^2$.

The above equation is the same as equation (3.35) minus the exponential factor $\exp[i\Delta r(\delta k^2(z)/2k_a)]$. Thus, is possible to include atmospheric refraction by multiplying the solution in a non-refracting atmosphere by a phase factor, as long as $\delta k^2(z)$ is small relative to $k^2(z)$. This method of splitting the effect of refraction in two terms (equation (3.39)), was first used in ocean acoustics and is known as the Fourier split-step algorithm [Dinapoli, et al., (1979)].

Replacing $q(r+\Delta r)$ with $\psi(r,z)=\exp(-ik_a r)q\,(r,z)$ for improved accuracy in numerical computations and including the refraction factor $\exp[i\Delta r(\delta k^2(z)/2k_a)]$, equation (3.31) results,

$$\psi(r+\Delta r,z)=e^{i\Delta r\frac{\delta k^2(z)}{2k_a}}\frac{1}{2\pi}\left\{\int_{-\infty}^{\infty}\left[\Psi(r,k_z)+R_p(k_z)\Psi(r,-k_z)\right]e^{i\Delta r\left(\sqrt{k_a^2-k_z^2}-k_a\right)}e^{izk_z}dk_z\right.$$
$$\left.+\,2i\beta\Psi(r,\beta)e^{i\Delta r\left(\sqrt{k_a^2-\beta^2}-k_a\right)}e^{-i\beta z}\right\} \tag{3.40}$$

where the spatial Fourier transform of $\psi(r,z)$ is,

$$\Psi(r,k_z)=\int_0^{\infty}\psi(r,z')e^{-iz'k_z}\,dz' \tag{3.41}$$

Equations (3.40) and (3.41) are the basic equations of the GFPE method with atmospheric refraction, which are used in the computational program.

3.6 ATMOSPHERIC TURBULENCE

The following sections describe the theoretical formulation and incorporation of atmospheric turbulence. Section 3.6.1 shows a standard approach in order to approximate the effect of turbulence on sound propagation in the atmosphere. Section 3.6.2 briefly describes a statistical approach to atmospheric turbulence, using two-dimensional spectral densities in the calculation of the refractive-index fluctuations. Section 3.6.3 explains the incorporation of turbulence in the GFPE method. Section 3.6.4 describes how to calculate the refractive-index fluctuations $\mu(r,z)$ and how to apply them to the GFPE method presented in the previous section.

3.6.1 Atmospheric model

Atmospheric turbulence on sound propagation models is usually described using an effective sound speed that randomly fluctuates around an average value. From equation (2.11), the effective sound speed is defined as,

$$c_{eff}=c_0\sqrt{\frac{T}{T_0}}+u \tag{3.42}$$

where $c_0\sqrt{T/T_0}$ is the adiabatic sound speed c [equation (2.9)] and u is the horizontal wind component in the direction of sound propagation (section 2.3.1). Temperature T_0 corresponds to an average value and c_0 is the corresponding sound speed. Small fluctuations of the temperature T and wind speed u

correspond to turbulent fluctuations of the effective sound speed c_{eff}. To measure these fluctuations, the acoustic refraction index n is used,

$$n = \frac{c_0}{c_{eff}} \tag{3.43}$$

This value fluctuates around an average number, which is of the order of the unit and is defined as n_d, being μ a fluctuating stochastic part. Thus, being $\mathbf{R}$ a position vector $\mathbf{R} = (x, y, z)$, and t the time, the refraction index results,

$$n(\mathbf{R}, t) = n_d(\mathbf{R}) + \mu(\mathbf{R}, t) \tag{3.44}$$

where $\mu \ll 1$, if weak turbulence is considered. Although the fluctuating part μ is a function of both space and time, its value can be approximated in a specific instant of time. This approximation is called the frozen medium approach and it is possible because the sound waves travel so fast that the medium can be considered as 'frozen'. Further, and simplifying the problem, n_d varies only with the height z above the ground. Additionally, μ varies with height z and range $(r = \sqrt{x^2 + y^2})$. Therefore, the sound propagates in the rz plane and the refraction index is azimuthally symmetric about the source. Taking into account these approximations, the refraction index is,

$$n(r, z) = n_d(z) + \mu(r, z) \tag{3.45}$$

The refraction index fluctuations $\mu(r, z)$ are further evaluated in section 3.6.4.

3.6.2 Gaussian and von Kármán spectral density

Using equations (3.42) and (3.43), the expression for the fluctuation μ is [Ostashev, (1997)],

$$\mu = -\frac{T_t}{2T_0} - \frac{u_t}{c_0} \tag{3.46}$$

where T_t is the temperature fluctuation and u_t is the wind speed fluctuation.

In a turbulent atmosphere, both temperature and wind speed are position and time fluctuating functions. In principle, these turbulent fluctuations are a deterministic process just as most physical phenomena, even though it is very hard to predict turbulence this way. Therefore, it is much easier to consider atmospheric turbulence a stochastic process. Statistical functions such as correlation, structure and spectral density, are used to describe temperature and wind speed fluctuations. [Salomons, (2001)] describes with detail how to obtain these functions.

We consider two different types of spectral density functions: the Gaussian and the von Kármán. For an atmosphere with temperature and wind speed fluctuations, and using equation (3.46), the two-dimensional Gauss spectral density function is [Ostashev, (1997)],

$$F(k_x, k_z) = \frac{a^2}{4\pi}\left[\frac{\sigma_T^2}{4T_0^2} + \frac{\sigma_v^2(k_z^2 a^2 + 2)}{4c_0^2}\right] e^{\frac{-k^2 a^2}{4}} \tag{3.47}$$

where a is the correlation lenght, $\sigma_T^2$is the standard deviation of the temperature fluctuation, σ_v^2 is the standard deviation of the wind speed fluctuation and $k = {k_x}^2 + {k_z}^2$.
Using the same conditions of equation (3.47), the two-dimensional spectral density of the von Kármán spectrum is [Ostashev, (1997)],

$$F(k_x, k_z) = \frac{5}{18\pi\Gamma\left(\frac{1}{3}\right)(k^2 + K_0^2)^{\frac{8}{6}}}\left[\frac{\Gamma\left(\frac{1}{2}\right)\Gamma\left(\frac{8}{6}\right)}{\Gamma\left(\frac{11}{6}\right)}\frac{C_T^2}{4T_0^2} + \frac{22C_v^2}{12c_0^2}\left(\frac{\Gamma\left(\frac{3}{2}\right)\Gamma\left(\frac{8}{6}\right)}{\Gamma\left(\frac{17}{6}\right)} + \frac{k_z^2}{k^2 + K_0^2}\frac{\Gamma\left(\frac{1}{2}\right)\Gamma\left(\frac{14}{6}\right)}{\Gamma\left(\frac{17}{6}\right)}\right)\right] \tag{3.48}$$

where $K_0 = 2\pi/L$ and L is related to the size of the largest eddies, C_v is the structure parameter of the wind speed fluctuation, C_T is the structure parameter of the temperature fluctuation and $k = {k_x}^2 + {k_z}^2$. The gamma function Γ is defined by the improper integral [Abramowitz, et al., (1972)],

$$\Gamma(z) = \int_0^\infty t^{z-1}\, e^{-t} dt \tag{3.49}$$

These two-dimensional spectral density functions are used in the calculation of the refractive-index fluctuations in section 3.6.4.

3.6.3 Turbulent phase factor

The two-dimensional sound field is represented by equation (3.6). Using the same method as in section 3.5, the one-way wave equation results,

$$\frac{\partial q(r,z)}{\partial r} = i\sqrt{Q}\, q(r,z) \tag{3.50}$$

where Q is the operator,

$$Q = k^2(z) + \partial_z^2 \tag{3.51}$$

Since only weak turbulence is considered ($\mu \ll 1$), the acoustic field is dominated by outgoing waves therefore, one-way wave propagation is an accurate approximation for turbulent effects. Assuming Q to be independent of range, the solution for equation (3.50) is,

$$q(r+\Delta r,z)=e^{i\Delta r\sqrt{Q}}q(r,z) \tag{3.52}$$

Like in section 3.5, the expression $\psi(r,z)=\exp(-ik_a r)q\,(r,z)$ is used to improve numerical accuracy once it varies more slowly with range than does q alone. Equation (3.52) results,

$$\psi(r+\Delta r,z)=e^{[i\Delta r(\sqrt{Q}-k_a)]}\psi(r,z) \tag{3.53}$$

as in equation (3.32), k_a is a constant wave number at some average height.

With the relation $n\approx k/k_a$ and assuming that $\overline{n}$ and $\overline{k}$ depend only of the height above the ground, equation (3.45) gives the following expression,

$$k=\overline{k}+k_a\mu \tag{3.54}$$

Substituting the above equation into equation (3.51) and ignoring the term ${k_a}^2\mu^2$ ($\mu \ll 1$) results,

$$Q\ \approx \overline{k}^2+\partial_z^2+2\overline{k}k_a\mu \tag{3.55}$$

The operator Q is the sum of a deterministic part $\overline{k}^2+\partial_z^2$ and a stochastic part $2\overline{k}k_a\mu$. Substituting Q into equation (3.53),

$$\psi(r+\Delta r,z)=\exp\left[i\Delta r\left(\sqrt{\overline{k}^2+\partial_z^2+2\overline{k}k_a\mu}-k_a\right)\right]\psi(r,z) \tag{3.56}$$

Therefore, it is possible to calculate the sound field for a given value of μ using equation (3.56) directly. Nonetheless, in computational terms, evaluating the entire operator $\sqrt{Q}$ in each range step is numerically inefficient. An alternative numerically faster method, requires to separate the deterministic part $\overline{k}^2+\partial_z^2$, which is calculated once, from the stochastic part $2\overline{k}k_a\mu$. [Gilbert, et al., (1990)] explains in detail the separation of the two factors. The resulting equation is,

$$\psi(r+\Delta r,z)=\exp\left[i\Delta r\left(\sqrt{\overline{k}^2+\partial_z^2}-k_a\right)\right]\exp(ik_a\mu\Delta r)\psi(r,z) \tag{3.57}$$

The first exponential factor on the right-hand side of equation (3.57) represents the sound field for a non-turbulent atmosphere [equation (3.53)], while the second factor represents the effect of turbulence. This method is computational more efficient than using equation (3.56), because turbulence is included by multiplying the sound field by an exponential factor after each range step.

[Gilbert, et al., (1990)] introduces a more accurate approach of equation (3.57). It consists in split the exponential turbulent factor into two different factors therefore, half of the turbulent exponential factor is applied before the step for the non-turbulent calculation, while the other half is applied after. This results in the following turbulent exponential factor,

$$\exp(ik_a\mu_2\Delta r) \tag{3.58}$$

where μ_2 is,

$$\mu_2 = \frac{1}{2}[\mu(r,z) + \mu(r+\Delta r, z)] \tag{3.59}$$

This exponential factor should be used when the horizontal range step is small compared with the turbulent correlation lenght, such as the CNPE method. In the GFPE, however, the range step can be larger than the turbulent correlation lenght thus, to correct this issue, [Martin, (1993)] gives the following turbulent exponential factor,

$$\exp(i\Theta) \tag{3.60}$$

where Θ is the turbulent phase fluctuation integrated over a range step, being its expression,

$$\Theta = k_a \int_r^{r+\Delta r} \mu(r,z)\, dr \tag{3.61}$$

Using the turbulent exponential factor in equation (3.60), the GFPE accurately takes into account the turbulent fluctuations within a range step.

3.6.4 Refractive-index fluctuations

Using the correlation function and the spectral density function, for a rectangular grid in the rz plane with vertical spacing Δz, as represented in Figure 2.9, the refractive index fluctuations function at the grid points is [Salomons, (2001)],

$$\mu(r, z_j) = \sum_{n=1}^{S} G(k_{nr}, k_{nz}) \cos(r k_{nr} + z_j k_{nz} + \alpha_n) \tag{3.62}$$

where,

$$G(k_{nr}, k_{nz}) = \sqrt{4\pi\ \Delta k\ F(k_{nr}, k_{nz})\ k_n} \tag{3.63}$$

being $k_{nr} = k_n \cos(\theta_n)$, $k_{nz} = k_n \cos(\theta_n)$ and $k_n = n\Delta k$ for $n = 1,2,3 \ldots, S$. The angles θ_n and α_n are random numbers between 0 and 2π. These numbers are calculated using the pseudorandom number generator referenced in section 4.2.4. The function $F(k_{nr}, k_{nz})$ is the two-dimensional spectral density and can be either equation (3.47) or (3.48). Replacing equation (3.62) into (3.61) results,

$$\Theta = \Upsilon(r + \Delta r, z_j) - \Upsilon(r, z_j) \tag{3.64}$$

with

$$\Upsilon(r, z_j) = k_a \sum_{n=1}^{S} \frac{G(k_{nr}, k_{nz})}{k_{nr}} \sin(r k_{nr} + z_j k_{nz} + \alpha_n) \tag{3.65}$$

To reduce computational effort, the sine function is evaluated as,

$$\sin(r k_{nr} + z_j k_{nz} + \alpha_n) = \mathrm{Im}[\exp(i r k_{nr} + i\alpha_n)\exp(i k_{nz}\Delta z)^j] \tag{3.66}$$

This way, for a fixed n, the sine factors can be calculated by recurrent multiplication by a constant factor $\exp(ik_{nz}\Delta z)$.

4 NUMERICAL IMPLEMENTATION

For the sound field calculation with the GFPE method, the equations (3.40) and (3.41) are used and, considering their nature, it is mandatory to make use of numerical methods to solve them (section 4.1). Section 4.2 describes additional functions of the program to correct some errors generated by the numerical approach. The numerical implementation complexity requires a programming language, which must offer fast and precise mathematical calculations, a wide range of open source libraries and be able to run in different environments. For these reasons, we chose the C language. The program implementation is described in section 4.3.

4.1 GREEN'S FUNCTION PARABOLIC EQUATION METHOD

The GFPE method (section 2.4.2.2) is a step by step extrapolation of the sound field $\psi(r + \Delta r, z)$ given by equations (3.40) and (3.41). A two dimensional rectangular grid like the one in Figure 2.9 is used, where Δr is the horizontal spacing and Δz is the vertical spacing. These two parameters are essentially frequency dependent, but atmospheric parameters also influence them. As it is a horizontal extrapolation method, the distance from the source to the receptor is given by the length of the grid and by the number of steps used. The grid is limited by the ground surface at $z = 0$ and is truncated at the top at height $z = z_{top}$, where the total height of the atmosphere is given by $z_{top} = M\Delta dz$, being M a positive integer. To prevent unwanted reflection from sound waves at the truncated top surface, an absorption layer is located between $z = z_{abs}$ and $z = z_{top}$, which is described in section 4.2.1. The next sections describe the different steps to implement the method numerically.

4.1.1 Starting field

As the GFPE method is a step by step extrapolation, the first step must be to define $\phi(0) \equiv \phi(0, z)$ as a starting field function that represents a monopole source. The complex pressure amplitude in an unbounded non-refracting atmosphere is represented by a harmonic spherical wave and can be written as,

$$p_c(\mathbf{r}) = S\frac{e^{ikr}}{r} \tag{4.1}$$

where r is the radial distance from the source and S is a constant. However, this expression cannot be used because it diverges from the source, since some of the sound waves have high elevation angles outside the area where the results are accurate (section 2.4.2), which creates computational errors in the solution.

In order to allow an accurate comparison with other methods, we use a Gaussian starting field given by [Tappert, (1977)],

$$\psi(z) = \sqrt{k_a}\exp\left\{-\frac{k_a^2}{2}(z-z_s)^2 + \frac{Z_g-1}{Z_g+1}\exp\left[\frac{-k_a^2}{2}(z+z_s)^2\right]\right\} \tag{4.2}$$

where z_s is the source height above the ground, the first term represents the direct sound wave and the second term represents the reflected wave.

4.1.2 Discretization of the Fourier integrals

To compute the sound field (equation (3.40)), it is necessary to calculate several Fourier integrals in each range step. Each of the integrals can be approximated by a sum called Discrete Fourier Transform (DFT). For the Fourier integral represented by equation (3.41), the discrete sum is [Champeney, (1985)],

$$\Psi(r,k_n) = \int_0^{\infty} \psi(r,z')e^{-iz'k_z}\,dz' \approx \left[\sum_{j=0}^{N-1} \psi(r,z_j)e^{-ik_n z_j}\right]\Delta z \tag{4.3}$$

where the integration variables k_z and z' are discretized respectively as,

$$k_n = n\Delta k, \qquad j = 0,1,2\ldots.N/2, -N/2+1, -N/2+2\ldots.-1 \tag{4.4}$$

$$z_j = j\Delta z \qquad j = 0,1,2\ldots\ldots N-1 \tag{4.5}$$

where $\Delta k = 2\pi/(N\Delta z)$, Δz is the vertical spacing described in section 4.1 and $N = 2M$ is the Fourier transform size. As a consequence of Fourier transform's periodic nature, the vector elements $\Psi(r,k_n)$ and $\Psi(r,-k_n)$ can be related between them by a permutation of vector positions. Therefore, it is possible to include both integrals into a single transformation of size $N = 2M$, which is the double of the vertical grid size. This assumption decreases the computational effort.

The integral $\Psi(r,\beta)$ only requires a single summation of N terms and its sum is,

$$\Psi(r,\beta) \approx \left[\sum_{j=0}^{N-1} \psi(r,z_j)e^{-i\beta z_j}\right]\Delta z \tag{4.6}$$

After the above integrals have been evaluated, the inverse Fourier integral of equation (3.40) can be calculated with an approximation analogous to equation (4.3),

$$\varphi(r, z_j) = \int_{-\infty}^{\infty} \Pi(r, k_z)\, e^{izk_z}\, dk_z \approx \left[\sum_{n=0}^{N-1} \Pi(r, k_n) e^{ik_n z_j}\right] \Delta k \tag{4.7}$$

where,

$$\Pi(r, k_z) = [\Psi(r, k_z) + R(k_z)\Psi(r, -k_z)] e^{i\Delta r\left(\sqrt{k_a^2 - k_z^2} - k_a\right)} \tag{4.8}$$

and k_n and z_j are described by equations (4.4) and (4.5) respectively. Finally, equation (3.4) is calculated with equations (4.6) and (4.7),

$$\psi(r + \Delta r, z) = e^{i\Delta r \frac{\delta k^2(z)}{2k_a}} \frac{1}{2\pi} \left\{ \varphi(r, z_j) + 2i\beta\Psi(r, \beta) e^{i\Delta r\left(\sqrt{k_a^2 - \beta^2} - k_a\right)} e^{-i\beta z} \right\} \tag{4.9}$$

Hence, the calculation of one range step requires two Fourier transforms: one forward DFT and one inverse DFT.

An alternative method for computing the Fourier integrals is based on the midpoint rule for numerical integration [Press, et al., (1986)]. The Fourier integral represented by equation (3.41) results in the following approximation,

$$\begin{aligned} \Psi(r, k_n) &\approx \left[\sum_{j=0}^{N-1} \psi\left(r, z_j + \frac{1}{2}\Delta z\right) e^{-ik_n\left(z_j + \frac{1}{2}\Delta z\right)}\right] \Delta z \\ &= \left[\sum_{j=0}^{N-1} \psi\left(r, z_j + \frac{1}{2}\Delta z\right) e^{-ik_n z_j}\right] e^{-\frac{1}{2} i \Delta z k_n} \Delta z \end{aligned} \tag{4.10}$$

where the integration variable k_z and z' are discretized as equation (4.4) and (4.5) respectively. Equation (4.10) uses the z coordinates at the center of the integration intervals $[z_j, z_{j+1}]$ therefore, the ground surface ($z = 0$) is represented more accurately in equation (4.10) than in equation (4.3), which in turn leads to a more accurate approximation. Using an approximation analogous to equation (4.10), the inverse Fourier transform integral in equation (3.40) results,

$$\begin{aligned} \varphi(r, z_j) &\approx \left[\sum_{n=0}^{N-1} \Pi\left(r, k_n + \frac{1}{2}\Delta k\right) e^{iz_j\left(k_n + \frac{1}{2}\Delta k\right)}\right] \Delta k \\ &= \left[\sum_{n=0}^{N-1} \Pi\left(r, k_n + \frac{1}{2}\Delta k\right) e^{iz_j k_n}\right] e^{\frac{1}{2} i \Delta k z_j} \Delta k \end{aligned} \tag{4.11}$$

using the same integration variables of equation (4.10).

4.1.3 Fast Fourier Transform

The direct calculation of the discrete sums is too slow to be practical therefore, an algorithm called Fast Fourier Transform (FFT) is used to calculate the forward DFT and its inverse, producing exactly the same results as evaluating the DFT directly. The advantage is that a FFT is much faster.

The chosen FFT was the "Fastest Fourier Transform in the West" or FFTW developed by Matteo Frigo and Steven Johnson at the Massachusetts Institute of Technology [Frigo, et al., (1997)]. The FFTW was written in C language and computes multidimensional complex discrete Fourier transforms of arbitrary size, using the Cooley–Tukey algorithm [Cooley, et al., (1965)]. FFTW's main advantages are:

i) faster than all other free available FFT software and it is comparable or even better than proprietary highly-tuned implementations,
ii) friendly interface and very well documented,
iii) not only restricted to transforms with a power of two size, although being faster in this particular situation,
iv) tunes the computation automatically to take advantage of particular hardware characteristics.

For these reasons the FFTW was the selected software to the computational program developed.

4.2 GFPE METHOD: ADDITIONAL FUNCTIONS

Due to the GFPE method limitations, such as the finite vertical discretization of the atmosphere, or the discrete sampling of the inverse Fourier, additional functions are required to help to correct the results, which are described in the next sections.

4.2.1 Artificial absorption layer

A real atmosphere can be regarded as being infinite in vertical height therefore, the sound waves travel to a point where their amplitude reaches zero. However, the DFT requires a finite discretization of the vertical height, which causes sound waves to be reflected back into the calculation region, causing errors in the sound field. To avoid this limitation, near the top of the numerical grid z_{abs}, a layer is introduced which, artificially, attenuates the sound waves reaching the top z_{top} [Gilbert, et al., (1993)]. This attenuation is obtained by adding an imaginary part to the wave number between z_{abs} and z_{top}, as described by the following equation,

$$k_{abs}(z) = k(z) + i\alpha(z) \tag{4.12}$$

where the imaginary part $\alpha(z)$ is defined as,

$$\alpha(z) = A\left(\frac{z - z_{abs}}{z_{top} - z_{abs}}\right)^2 \tag{4.13}$$

with A being an attenuation factor that varies with frequency (see Table 4.1) [Gilbert, et al., (1993)]. Intermediate frequencies are obtained by linear interpolation. Therefore equation (4.12) results,

$$k_{abs}(z) = k(z) + iA\left(\frac{z - z_{abs}}{z_{top} - z_{abs}}\right)^2 \tag{4.14}$$

The thickness of the absorption layer varies between 50λ and 100λ. If $\Delta z = \lambda/10$, the number of points of the layer ranges from 500 to 1000.

Table 4.1- Values of the attenuation factor for an octave band scale

$\boldsymbol{f}$(hz)	$\leq$ **16**	**31.5**	**63**	**125**	**250**	**500**	$\geq$ **1000**
$\boldsymbol{A}$ (m^{-1})	0.1	0.2	0.3	0.4	0.5	0.5	1

By increasing the number of vertical points M up to a certain level, it is possible to obtain irrelevant sound wave amplitude values. Nevertheless, the use of this method is unpractical, since it increases the computational effort dramatically.

The right plot of Figure 4.1 -shows a situation when there is no absorption layer. Similar situation occurs if the layer thickness is not enough to attenuate the sound waves completely.

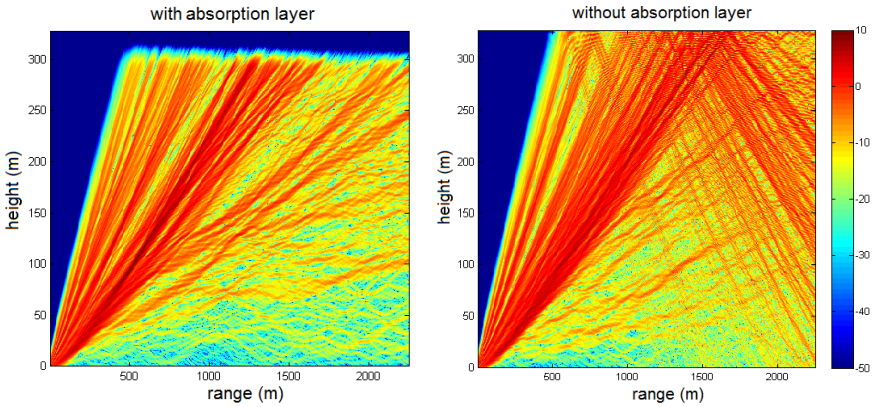

Figure 4.1 - Two-dimensional complete plots using the simulation parameters from test case B1 (Table 5.6), with an absorption layer of 20 m $(50\lambda = 500 \times 0.04)$.

The left plot shows that over 300 m of height (dark blue region), the absorption layer attenuates all the sound waves. As illustrated by the right plot above, the existence of sound waves reflected, as a

consequence of the computational method, creates artificial interferences. To avoid these interferences and to ensure accurate results, we use an absorption layer in all simulations.

4.2.2 Window function

The discrete sampling of the inverse Fourier transform causes errors when its summand oscillates rapidly. From equation (3.40), and k_z discretized as equation (4.4), the summand is,

$$S(k_n) = \frac{1}{N\Delta z}\left(\Psi(r,k_n) + R_p(k_n)\Psi(r,-k_n) \times e^{i\Delta r\left(\sqrt{k_a^2-k_z^2}-k_a\right)} e^{izk_n}\right) \tag{4.15}$$

being Δz the vertical spacing defined in equation (4.5) for a reflecting ground surface.

The cumulative sum of the above equation is,

$$C(k_n) = \sum_{i=0}^{n} S(k_i) \tag{4.16}$$

where i runs from zero to n in the order of equation (4.4).

To illustrate the variation of equation (4.15) with the vertical wave number, the following table shows a test case where a single range step is used,

Table 4.2 - Test case parameters

frequency $\boldsymbol{f}$ (hz)	$\mathbf{100}$	source height $\boldsymbol{z_s}$ (m)	$\mathbf{2}$
wave number $\boldsymbol{k_a}$ (m^{-1})	1.85	receiver height z_r (m)	4
non-refracting atmosphere		horizontal spacing Δr (m)	100
reflecting ground $\boldsymbol{Z_g}$	∞	vertical spacing Δz (m)	0.33

The summand is characterized by the following graphs,

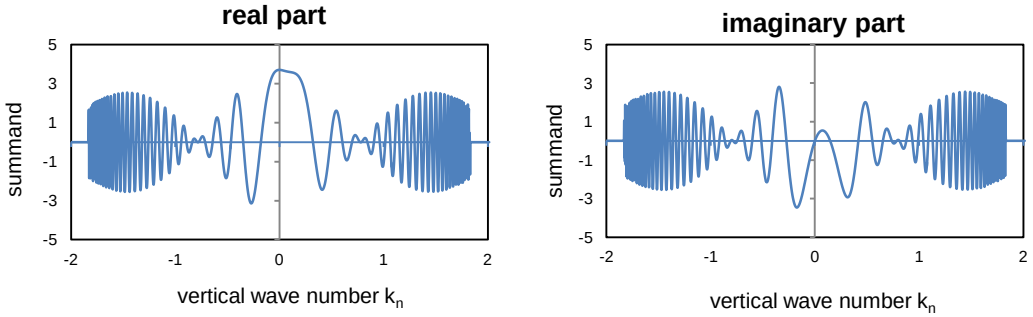

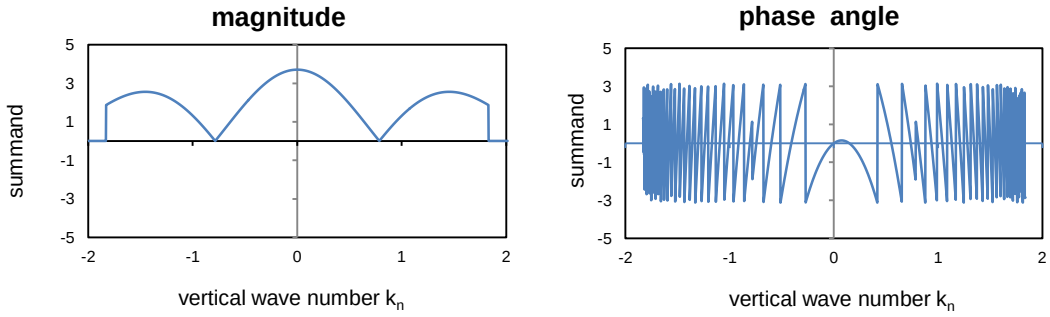

Figure 4.2 - Summand of the inverse Fourier transform in relation to the wave number k_n

As illustrated by the top two graphs of Figure 4.2, the summand oscillates very quickly for $|k_n| > 0.5k_a$. For $|k_n| > k_a$ its magnitude is zero and therefore are called evanescence waves (bottom left graph of Figure 4.2). The inverse Fourier transform of equation (3.40) is determined only by the vertical wave numbers k_n near the point of stationary phase which, in this case, is $k_n \approx 0.075$ m^{-1} (bottom right graph of Figure 4.2). We multiply the summand by window function to suppress its rapid oscillation [Salomons, (1998)],

$$\begin{cases} 1 & \text{for } |k| < 0.5k_a \\ \cos^2\left(\dfrac{\pi(|k| - 0.5k_a)}{k_a}\right) & \text{for } 0.5k_a \le |k| \le k_a \\ 0 & \text{for } |k| > k_a \end{cases} \tag{4.17}$$

Applying the above function to the test case of Table 4.2 results the following graphs,

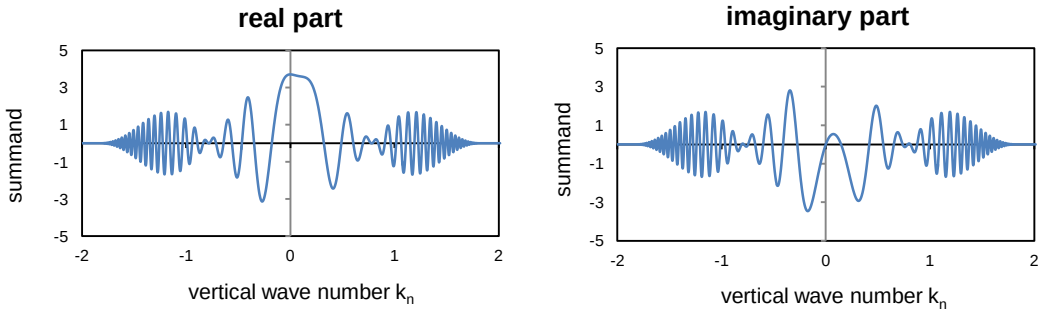

Figure 4.3 - Summand of the inverse Fourier transform in relation to the wave number k_n with the window function apllied.

Comparing the previous figure with Figure 4.2, the window function of equation (4.17) acts like a numerical filter in k space, suppressing the errors caused by the discrete sampling of the inverse

Fourier transform. The cumulative sum (equation (4.16)) for a height of 4 m is compared with and without the window function,

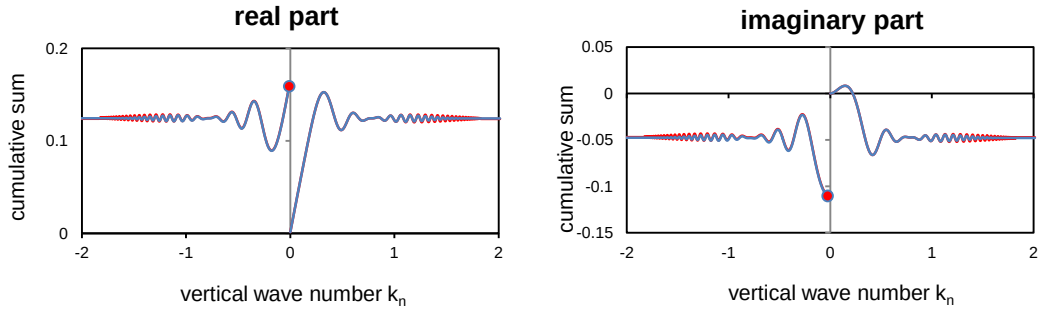

Figure 4.4 - Cumulative sum of equation (4.15), the blue line has the window function active and in the red line the window function is not applied.

As expected, the window function does not change the value of the cumulative sum. The red circle represents the complete sum of equation (4.16) or $C(k_N)$. This value can be regarded as ψ for a single range step of 100 m at an altitude of 4 meters, with the parameters of Table 4.2. Maintaining the same range step, the complete calculation of ψ, for a height of 300 m, is given bellow,

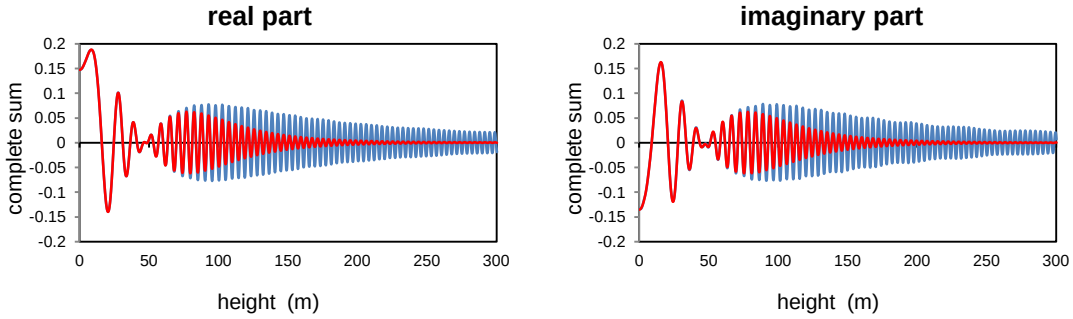

Figure 4.5 - Real and imaginary part of ψ. The red line represents the window function active, while in the blue line the window function is not applied.

The two graphs above show that with the window function, ψ converges faster with increasing height, as expected.

4.2.3 Alternate refraction factor

In section 3.5, atmospheric refraction was taken into account by multiplying the solution by the following exponential factor,

$$\exp\left(i\Delta r\frac{\delta k^2(z)}{2k_a}\right) \tag{4.18}$$

An alternate approach comes from another expansion of the square root operator $\sqrt{Q}$ defined as [Thomson, et al., (1983)],

$$\sqrt{Q} = \sqrt{(k_a + \delta k)^2 + \partial_z^2} \approx \sqrt{\partial_z^2 + k_a^2 + 2k_a \delta k} \approx \sqrt{\partial_z^2 + k_a^2} + \delta k \tag{4.19}$$

with $k(z) = \delta k(z) + k_a$. Following equations (3.38) and (3.39) the alternate refraction factor is,

$$\exp[i\Delta r\ \delta k(z)] \tag{4.20}$$

Numerical comparison with the CNPE presented in section 5.2.2, show that this exponential factor is slightly more accurate than the one given in equation (3.39) thus, all computational simulations use the alternate refraction factor.

4.2.4 Pseudorandom number generator

The statistical approach of calculation of the atmospheric turbulence used in this program (section 3.6.4) requires the use of random numbers in each range step. Without specific external hardware, a desktop computer can only generate a sequence of numbers that approximates the properties of random numbers i.e., a pseudorandom number generator (PRNG). This algorithm is completely determined by an initial value, known as seed or key. Therefore, the same sequence of numbers can be generated if the same seed is used. This feature is useful to test different turbulent parameters. The maximum sequence length before it begins to repeat itself is known as period. The period is determined by the size of the seed, measured in bits.

Several PRNG exist, including the standard C PRNG algorithm, but most of them (including the C algorithm) suffer from limitations such as low periodicity, lack of uniformity of distribution for large amounts of generated numbers and correlation of successive values. To address these limitations, [Matsumoto, et al., (1998)] developed a PRNG algorithm, written in C language, called the Mersenne Twister. Its name derives from the chosen period length, $2^{19937} - 1$, which is a Mersenne prime number. This algorithm has a very long period, in contrast with short periods (such as 2^{32}) found in most algorithms, and has passed numerous tests for statistical randomness.

Since the turbulent calculations use large amounts of random numbers, it is necessary to use a precise and fast algorithm, which generates long sequences of pseudorandom numbers, as close as possible to 'real' random numbers. For these reasons, the Mersenne Twister is the chosen PRNG algorithm and the seed used is the computer clock.

4.3 PROGRAM DESCRIPTION

In this section it is presented the flow chart of the software program developed, its description and the several features included.

The following diagram illustrates the organization of the computational program in a diagrammatic representation, including the user interface features, algorithm flow process, the input and the output interface.

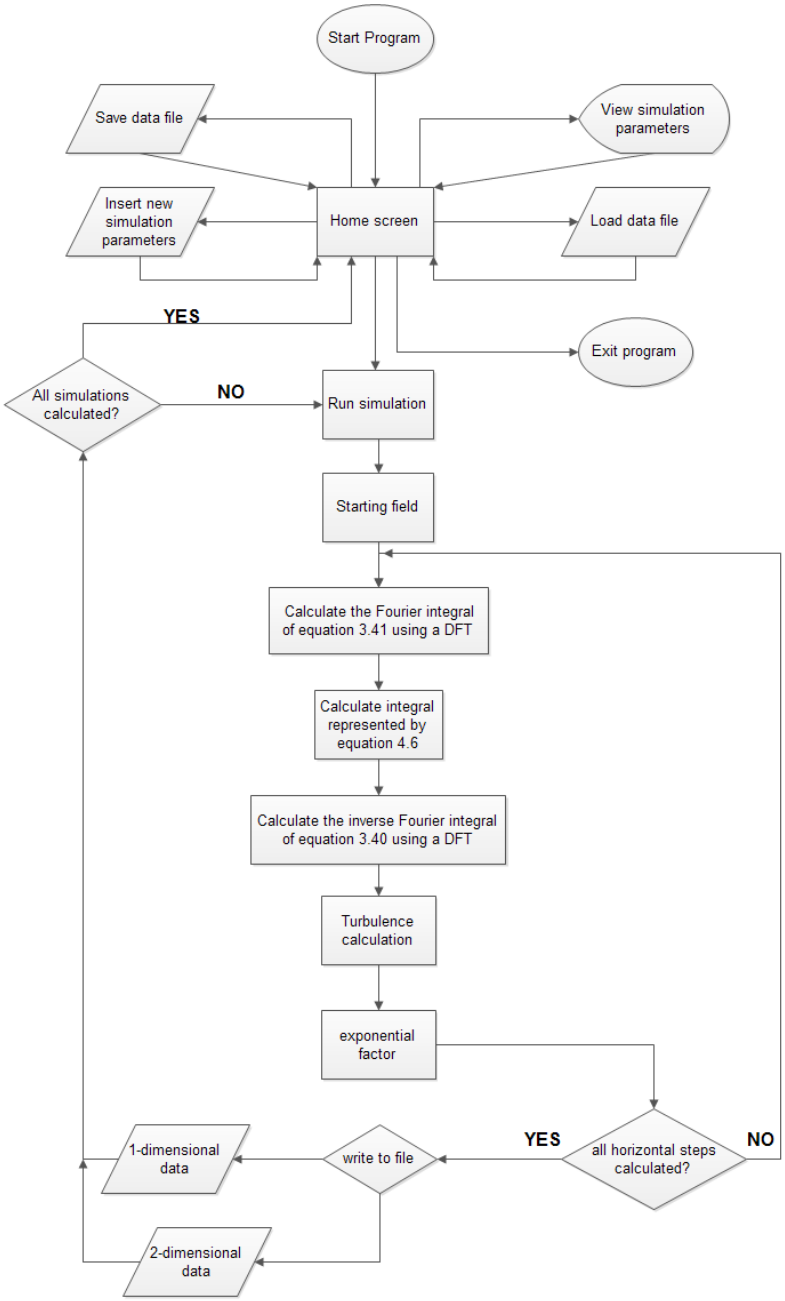

Figure 4.6 - Flow chart illustration of the computational program

4.3.1 User interface

The interaction with the program is obtained by typing commands in order to select the different options from the home screen, by inserting filenames of output or input files and by manually inserting simulation variables. This type of mechanism to interact with a software is also known as a command-line type interface (CLI).

In the main screen, the main options for controlling the program are displayed and included,

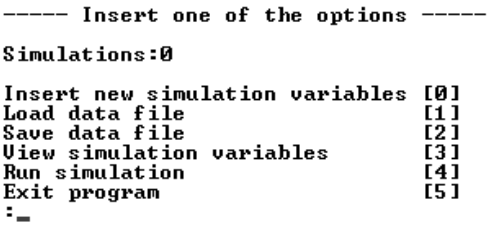

Figure 4.7 - Home screen interface

The table bellow summarizes and explains the different options above,

Table 4.3 - Home screen options explained in detail

Simulations	Displays the number of simulations stored in memory
Insert new simulation variables [0]	The different parameters are introduced one by one, for one or more simulations and are stored in memory
Load data file [1]	Loads to the computer memory a text data file which can contain one or more simulations
Save data file [2]	Saves to a chosen text data file the current simulations parameters stored in memory
View simulation variables [3]	Displays the different parameters of all simulations stored in memory
Run simulation [4]	Executes the program for all simulations stored in memory, in the same order they were loaded or manually inserted
Exit program [5]	Closes the program as well as all simulations stored in memory

The program returns error messages when introducing invalid options or incorrect simulation parameters.

4.3.2 Input files

As described in the section above, the program offers two ways to input the simulation variables: manually, inserting one by one directly in the program, or by loading a specific structured file. An example of the input file is,

```
100.000000              frequency
4096                    number vertical points
0.2000                  vertical spacing
20                      number of horizontal steps
10.000000               horizontal spacing
2.000000                source height
2.000000                receiver height/graph height
1.000000 1.000000       complex impedance
1                       [0]for non reflecting [1]for reflecting ground
0                       [0]constant [1]non constant vertical sound speed
343.000000              sound speed at the ground
1.831832                wave number at the ground
0.000000                refraction velocity
0.000000                ground roughness lenght
0.359677                attenuation factor
0                       [0]no turbulence [1]Gauss [2]von Karman spectrum
0.000000E+000           a Gauss spectrum
0.000000E+000           (TauT)^2/(T0)^2 Gauss spectrum
0.000000E+000           (Tauv)^2 Gauss spectrum
0.000000E+000           K0 von Karman spectrum
0.000000E+000           (CT)^2/(T0)^2 von Karman spectrum
0.000000E+000           (CV)^2/(C0)^2 von Karman spectrum
0                       N number of nodes (turbulence)
0.000000E+000           k node spacing (turbulence)
1                       [1] 1-dimensional [2] 2-dimensional graph
```

Figure 4.8 - Input file example.

When using the save option in the home screen, the program stores all simulations in a chosen text file with the structure displayed in Figure 4.8. When there is more than one simulation, the program stores the parameters into a single file, in a sequential order. These features allow the user to modify the parameters directly in the text file, reducing the time to introduce more than one simulation, especially when they differ only by few parameters. The load file option located in the home screen (Figure 4.7), is used to load the input file to the computer memory.

4.3.3 Simulation calculation

When option [4] (Figure 4.7) is selected, the program starts to calculate all simulations stored in memory. Each of the following steps corresponds to a process illustrated in Figure 4.6:

i) the starting field is calculated using equation (4.2) or $\psi(0, z_j)$, where the vertical height z is discretized as equation (4.5);

ii) then, the program runs a main loop, where each execution corresponds to a range step calculation. Using the previously calculated vector $\psi(0, z_j)$ (only for the first range step), the Fourier integral of equation (3.41) is approximated by a DFT, as described in section 4.1.2, with either equation (4.3) or the more accurate mid-point rule of equation (4.12). Any of the sums are calculated using the FFT algorithm described in section 4.1.3;

iii) the integral $\Psi(r, \beta)$ is calculated using equation (4.6), which only requires a single summation of N terms;

iv) as shown in section 4.1.2, the inverse Fourier integral of equation (3.40) is approximated by a DFT with either equation (4.7) or the mid-point rule of equation (4.11) using the same FFT algorithm as the forward Fourier transform;

v) turbulence is included by calculating equation (3.64) for all heights z_j;

vi) the final process of the main loop is to calculate the exponential factor, which can be done either from equation (3.39) or from equation (4.20), with the latter being more accurate. The absorption layer is included here (Figure 4.9), as described in section 4.2.1. As the turbulence is also incorporated multiplying the sound field by the previously calculated turbulent exponential factor [equation (3.60)], it is computed simultaneously with the refraction factor, as a way to reduce computational effort.

At the end of the loop, $\psi(r, z_j) = 0$ for heights z_j where $j \in [M, N-1]$, as a way to avoid coupling between the top and ground surface, which can generate computational errors (Figure 4.9). These heights can be interpreted as corresponding to negative heights, due to the Fourier transform's periodic nature. The program, then, repeats the loop, using the calculated vector $\psi(r, z_j)$ as illustrated in Figure 4.6. When all range steps are calculated, the program writes the results to a text file as described in the next section. The following figure illustrates how the computational grid is organized.

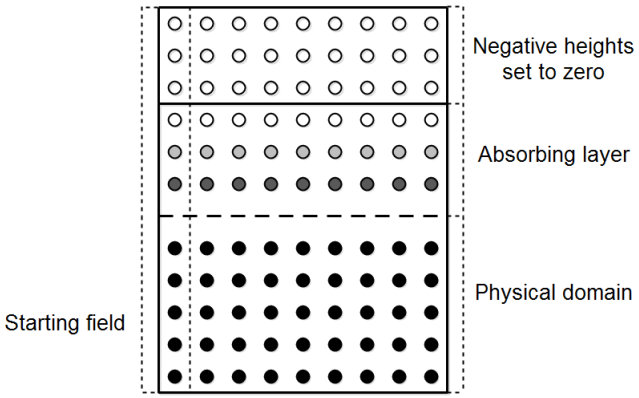

Figure 4.9 - Schematic representation off the computational grid.

4.3.4 Output files

As defined in section 2.1, the relative sound pressure ΔL (equation (2.4)) is used to measure the sound pressure in relation to the free field. This way, the attenuation caused by geometrical spreading (section 2.2.1) and the resulting attenuation from atmospheric absorption (section 2.2.2) can be ignored. Additionally, the transmission loss (TL) is also an output option of the program, primarily used for benchmark purposes.

The sound pressure level L_p (section 2.1) can be obtained from the following expression,

$$L_p = L_w - 10\log(4\pi R^2) - \alpha R + \Delta L \tag{4.21}$$

where the first term on the right hand side is the sound power level, or in other words, a measure of the strength of the sound source; the second term corresponds to the geometrical attenuation at a distance R from a source, corresponding to a spherical spreading situation; the third term represents the attenuation of sound waves due to atmospheric absorption, being α the absorption coefficient (in dB per unit of length); finally, the relative sound pressure ΔL can also regarded as the influence that meteorological factors (temperature, wind, turbulence), ground surface and topographical features have on sound levels.

Two types of graphs can be obtained for each simulation: one-dimensional or two-dimensional. One-dimensional type saves the sound levels at a specific receiver height $z = z_r$, whereas two-dimensional type writes the sound levels between $z = 0$ and $z = z_r$. Using the basic geometry of Figure 2.1 both cases can be represented as,

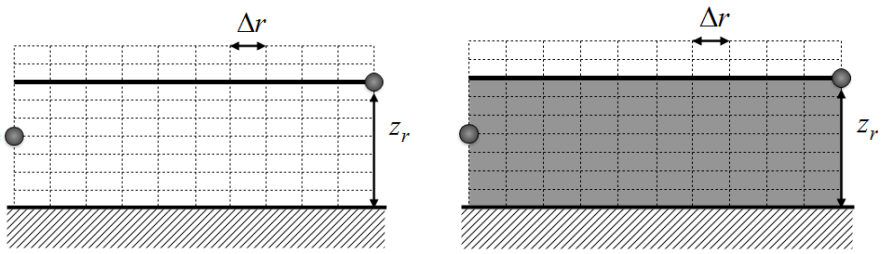

Figure 4.10 - Left image represents one-dimensional graph. Right image represents two-dimensional graph.

On the one-dimensional type, each horizontal position r corresponds to a sound level output (represented by the thick line in the left image of Figure 4.10). On the two-dimensional case, each r corresponds to a vector of sound levels, between $z = 0$ and $z = z_r$ (represented by grey area in the right image of Figure 4.10). As the following figure illustrates, the one-dimensional type output file consists of two data columns: the first one being the range step and the second one is the corresponding relative sound pressure,

```
10.000000  2.661959
20.000000  5.285358
30.000000  5.639868
40.000000  5.823078
50.000000  5.890145
60.000000  5.926498
70.000000  5.955618
80.000000  5.967456
90.000000  5.979480
100.000000  5.987894
110.000000  5.991889
120.000000  5.997827
130.000000  6.000413
140.000000  6.002965
150.000000  6.005934
160.000000  6.006774
170.000000  6.008904
180.000000  6.010029
190.000000  6.010721
200.000000  6.012227
```

Figure 4.11 - One-dimensional output file of the example test case displayed in Figure 4.8

On the two-dimensional output file, the first upper row indicates the range step r, while the first left column indicates the height z therefore, to every grid position (r, z) corresponds a specific relative sound pressure value. The figure below shows an example of the two-dimensional output file, with the parameters of Figure 4.8,

```
0.000000  10.000000  20.000000  30.000000  40.000000  50.000000  60.000000  70.000000  80.000000  90.000000  100.000000
0.000000  5.994153  5.876106  6.005665  6.004597  5.997392  6.021878  6.007640  6.016797  6.018477  6.013428  6.020877
0.200000  5.930553  5.862987  5.998407  6.000857  5.995103  6.020017  6.006512  6.015806  6.017695  6.012874  6.020315
0.400000  5.806646  5.840760  5.984337  5.993969  5.991005  6.016367  6.004539  6.013918  6.016208  6.011905  6.019205
0.600000  5.622589  5.809222  5.963511  5.983922  5.985086  6.010944  6.001710  6.011137  6.014018  6.010516  6.017554
0.800000  5.378578  5.768033  5.936023  5.970700  5.977326  6.003774  5.998007  6.007471  6.011130  6.008698  6.015369
1.000000  5.074820  5.716730  5.901995  5.954282  5.967696  5.994892  5.993403  6.002926  6.007547  6.006437  6.012662
1.200000  4.711493  5.654737  5.861581  5.934640  5.956161  5.984341  5.987867  5.997514  6.003278  6.003718  6.009449
1.400000  4.288696  5.581383  5.814959  5.911740  5.942684  5.972170  5.981362  5.991247  5.998329  6.000525  6.005746
1.600000  3.806389  5.495918  5.762326  5.885543  5.927219  5.958434  5.973848  5.984138  5.992707  5.996837  6.001571
1.800000  3.264318  5.397527  5.703890  5.856005  5.909722  5.943191  5.965282  5.976203  5.986422  5.992633  5.996946
2.000000  2.661959  5.285358  5.639868  5.823078  5.890145  5.926498  5.955618  5.967456  5.979480  5.987894  5.991889
2.200000  1.998466  5.158531  5.570473  5.786714  5.868443  5.908415  5.944813  5.957912  5.971890  5.982599  5.986422
2.400000  1.272685  5.016163  5.495908  5.746859  5.844571  5.888995  5.932825  5.947587  5.963659  5.976727  5.980562
2.600000  0.483290  4.857381  5.416360  5.703463  5.818487  5.868291  5.919612  5.936494  5.954793  5.970262  5.974328
2.800000  -0.370859  4.681337  5.331990  5.656476  5.790155  5.846347  5.905139  5.924644  5.945297  5.963187  5.967735
3.000000  -1.289919  4.487219  5.242923  5.605852  5.759543  5.823198  5.889375  5.912050  5.935175  5.955488  5.960796
3.200000  -2.271510  4.274261  5.149244  5.551552  5.726622  5.798874  5.872297  5.898718  5.924430  5.947157  5.953521
3.400000  -3.307825  4.041741  5.050992  5.493543  5.691373  5.773391  5.853888  5.884654  5.913062  5.938186  5.945915
3.600000  -4.380657  3.788988  4.948149  5.431802  5.653777  5.746758  5.834137  5.869859  5.901073  5.928573  5.937983
```

Figure 4.12 - A portion of the two-dimensional output file of the example test case with parameters from Figure 4.8

As expected, the row corresponding to a height of 2 meters has the same values of the one-dimensional example shown in Figure 4.11.

The program continuously calculates all simulations and saves the results in different files. This way is possible to introduce different parameters in the same atmosphere, such as entire frequency spectrums or various turbulence trials. When all simulations are calculated, the programs returns to the home screen (Figure 4.6).

5 ANALYSIS AND RESULTS

In this chapter, we validate the numerical implementation described in chapter 4 based on the GFPE theory present in chapter 3 (section 5.2), using the test cases introduced in section 5.1. Furthermore, the numerical program developed is compared with sound levels collected from a real atmosphere, i.e., with atmospheric turbulence (section 5.3).

5.1 BENCHMARK TEST CASES

This section defines various test cases to analyze the accuracy and optimization of the GFPE method described in chapters 3 and 4. The following table describes the two test cases, which have a non-refracting atmosphere with three source frequencies [Salomons, (1998)],

Table 5.1- Acoustic and environment parameters for two test cases in a non-refracting atmosphere

Test case	1	2
Atmosphere	non-refracting $c_0 = 343$ m/s	non-refracting $c_0 = 343$ m/s
Ground surface	reflecting	absorbing
10 Hz	$Z_g = \infty$ (at all frequencies)	$Z_g = 51.94 + 51.73i$
100 Hz		$Z_g = 16.73 + 16.06i$
1000 Hz		$Z_g = 6.336 + 4.229i$
Source/receiver height	2 m	2 m

As described in section 2.2, in a non-refracting atmosphere the adiabatic sound speed is constant in all medium's points.

The influence of a ground surface on sound propagation is explained in section 2.2.3. Although ground surfaces are usually irregular and vary with range, in these test cases the ground is assumed to be transversely uniform, to have range independent properties and to be a completely flat ground surface. The ground impedance of test case 1 ($Z_g = \infty$) represents a water surface while the ground impedances enumerated for the test case 2 represent grassland. They are calculated using equations (2.7) and (2.8) with the following parameters:

i) porosity $\Omega = 0.3$,
ii) flow resistivity $\sigma = 300\ \mathrm{kPA \cdot s \cdot m^{-2}}$,
iii) s_f is the pore shape factor ratio $s_f = 0.75$
iv) grain shape factor $g = 0.5$

Both receiver and source are 2 meters above the ground surface.

Although these two test cases are incomplete representations of a real atmosphere, both have an exact analytical solution, which is useful and fundamental to test the accuracy of the program.

The next test cases represent a more complex atmosphere, including atmospheric refraction as described in section 2.3.1 and their parameters are taken from benchmark problems used to test outdoor sound propagation models [Attenborough, et al., (1995)]. The following table displays the sound speed profiles of the four test cases,

Table 5.2 - Atmospheric refraction parameters of four test cases

Test case	3	4	5		6
Sound speed profiles speed c $(\mathrm{m/s})$	upward	downward	DUC		downward
	$343 - z/10$	$343 + z/10$	$343 + z/10$	$0 \leq z < 100$	$343 + \ln(z/0.1 + 1)$
			$363 - z/10$	$100 \leq z < 300$	
			333	$z \geq 300$	

Test case 3 represents an idealized situation of sound propagation under upwind conditions. Test case 4 is similar to the previous one, only with opposite gradient sign and represents a downwind condition. Test case 5 is a DUC profile (downward - upward - constant) and is composed by three functions: a positive gradient up to 100 m, then a negative gradient between 100 and 300 m, followed by a constant profile. The gradient values are similar to the previous ones. Test case 6 is a logarithmic profile, which is used as a realistic representation of the atmosphere above open ground areas (section 2.3.1). From equation (2.12), $z_0 = 0.1$ and $c_0 = 343$ m/s.

Figure 5.1 illustrates the previous sound speed profiles and Table 5.3 displays the remaining simulation parameters.

Table 5.3 - Acoustic and environment parameters for test cases from Table 5.2.

Starting field	Gaussian
Ground surface	absorbing
1000 Hz	$Z_g = 40.16 + 39.97i$
100 Hz	$Z_g = 12.97 + 12.38i$
10 Hz	$Z_g = 5.03 + 3.18i$
Source height	5 m
Receiver height	1 m

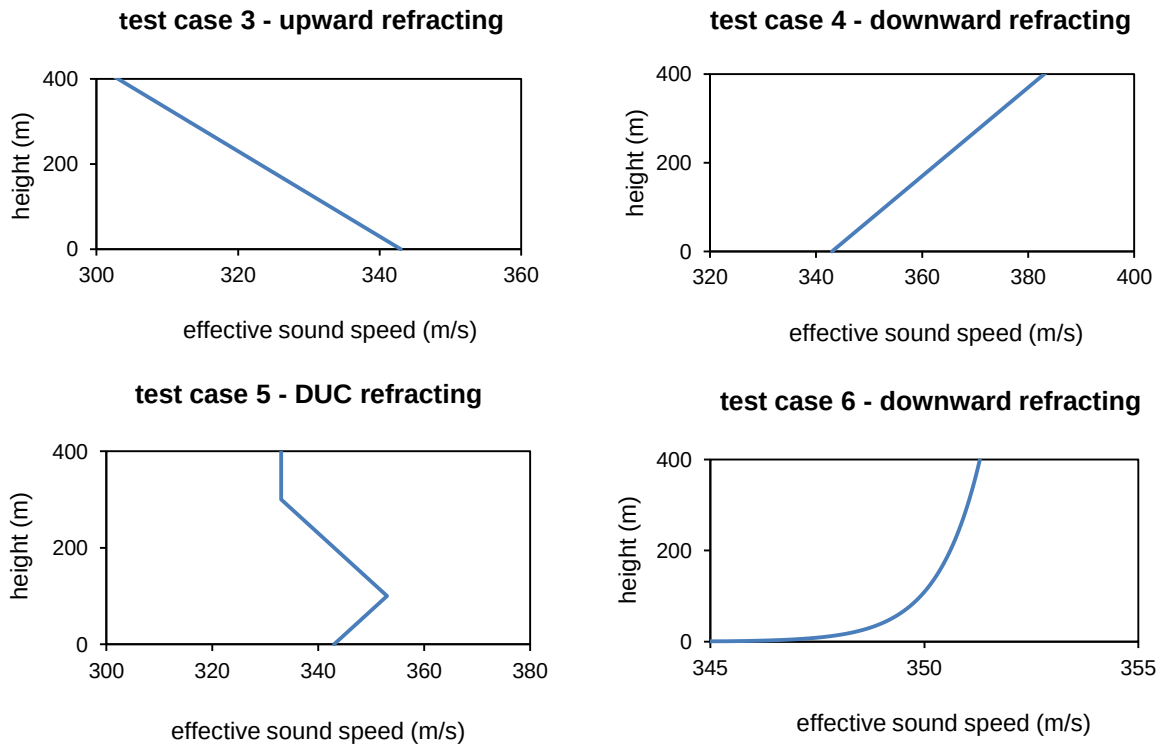

Figure 5.1- Plots of the sound speed profiles of Table 5.2.

Normalized ground impedance values are similar for the four test cases and were calculated using equations (2.7) and (2.8) with the following parameters:

i) porosity $\Omega = 0.27$,

ii) flow resistivity $\sigma = 366\ \mathrm{kPA \cdot s \cdot m^{-2}}$,

iii) s_f is the pore shape factor ratio $s_f = 0.5$,

iv) grain shape factor $g = 0.5$,

v) air density $\rho_0 = 1.2\ \mathrm{kg/m^3}$.

These test cases will be used in the following section to validate the developed numerical program.

5.2 GFPE METHOD VALIDATION

In this section, we validate the computational program developed, which uses the GFPE method, with, either the exact solution for a non-refracting atmosphere (section 5.2.1), or a known accurate computational method for a refracting atmosphere (section 5.2.2), by analyzing and comparing its results. Simultaneously, we analyze some computational errors.

5.2.1 Non-refracting atmosphere

With the parameters described in Table 5.1, we present the program results in the following plots using, either the standard Fourier transform [equation (4.3)], or the alternate Fourier transform based on the midpoint rule for numerical integration [equation (4.10)]. Furthermore, we introduce the results with the exact solution, which numerically integrates an exact Laplace transform for a point source in a homogeneous atmosphere above an absorbing ground [Di, et al., (1993)]. All the results in this section use the relative sound pressure to measure the sound levels [equation (2.4)].

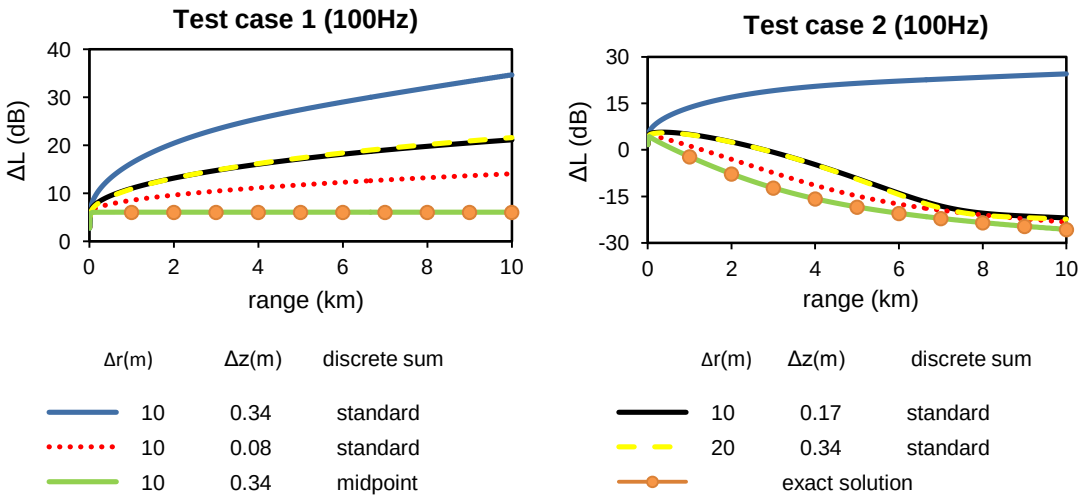

Figure 5.2 - Relative sound pressure up to 10 km with parameters from test case 1 (left figure) and test case 2 (right figure), for a 100 Hz point source.

As described in section 2.4.2.2, the vertical spacing Δz should not be larger than $\lambda/10$ or 0.34 m in these two test cases. On the other hand, the horizontal spacing can be up to 50λ, depending on the simulation parameters. Since this section analyses the accurancy of the foward Fourier transform, we use conservative values of Δr (10 m and 20 m).

Acording to Figure 5.2, the sound level results, with the standard Fourier transform, deviate substantially from the exact solution (up to 50 dB in test case 2). However, when using smaller vertical spacings, the latter results tend to approximate the exact solution. Oppositely, the error decreases with increasing horizontal spacing.

The alternate Fourier transform results, based on the midpoint rule, are very similar to the exact solution, presenting a difference minor than 0.1 dB. With $\Delta z = \lambda/10$, the standard transform deviates considerably. We found similar results for the frequencies 10 and 1000 Hz.

The alternate Fourier transform allows the use of larger Δz to obtain accurate sounds levels and consequently, the program requires a smaller number of vertical points. This results in a more efficient computational effort and, simultaneously, an accurate solution. For these reasons, all the following test cases use the alternate Fourier transform.

The discrete sampling of the inverse Fourier transform causes numerical errors due to the rapid oscillation of its summand [equation (4.11)]. Section 4.2.2 describes in detail the nature of this type of numerical error and the use of a window function to prevent it [equation (4.14)].

In the following plots, we test the window function's influence on sound levels and, simultaneously, compare them with the accurate results of Figure 5.2, using the test cases in Table 5.1.

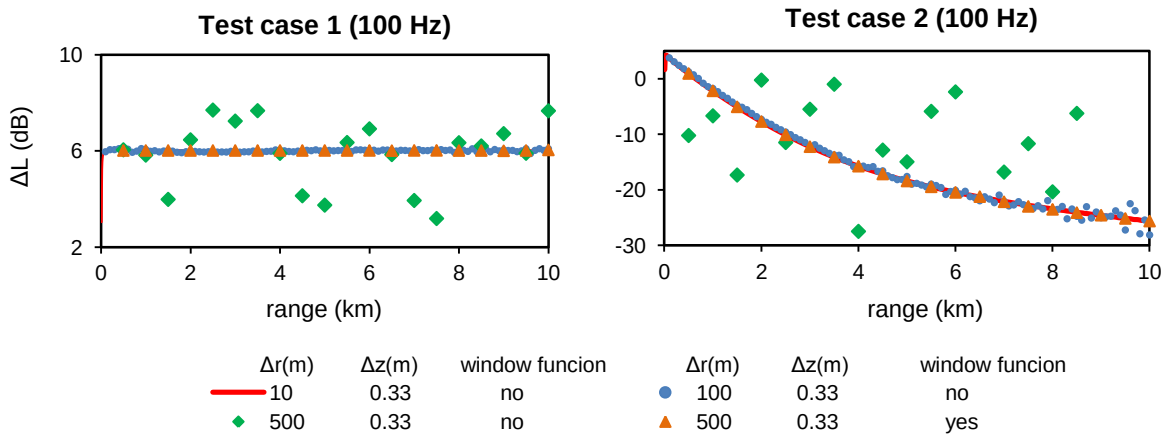

Figure 5.3 - Relative sound pressure up to 10 km, with parameters from test case 1 (left figure) and test case 2 (right figure), with and without the window function, for a 100 Hz point source.

For a horizontal spacing over 100 m and without the window function, the results begin to deviate from the exact solution. We obtained analogous results for 10 and 1000 Hz. With the window function, we can use range steps up to 500 m, allowing a greater computational efficiency, without compromising the solution's accuracy. With atmospheric refraction, the maximum range steps allowed are smaller, as can be seen in the next section.

Overall, the program results agree perfectly with the exact solution, particularly when we use the alternate Fourier transform and the window function. In this situation, the difference between the two solutions, up to a range of 10 km, is less than 0.1dB. For this reason, we are quite sure that the numerical implementation for a non-refracting atmosphere is numerically accurate.

5.2.2 Refracting atmosphere

Using the test cases from Table 5.2 and Table 5.3, we calculate the results and compare them with the CNPE method, as its accuracy is well known. From [Gilbert, et al., (1993)] we took, as reference, the range step values for the GFPE method, as well as, the reported range step values for the CNPE method. This was required to compare the number of horizontal steps used by each method and thus evaluate the speed advantage of the GFPE over the CNPE methods. The downward and DUC sound speed profiles cause the sound levels to oscilate in some frequencies in contrast with the smooth

nature of the sound levels generated by the upward sound speed profile. These results allow to use larger range steps in upward profiles.

In some frequencies, we verified it was possible to use larger range steps than the ones reported by [Gilbert, et al., (1993)], and at the same time to obtain similar sound levels. This result is most likely an influence of the window function (section 4.2.2), as we tested in the previous section.

Since the CNPE method sound levels are evaluated using the transmission loss (TL) [equation (2.6)], we also used it to calculate the sound levels in the develop program. For all simulations we used a vertical spacing of $\Delta z = \lambda/10$ thus, 3.43 m for 10 Hz, 0.343 m for 100 Hz and 0.034 m for 1000 Hz. Furthermore, the number of vertical points M used was 2048 for 10 Hz and 100 Hz and 4096 for 1000 Hz. Test case 3 is represent by three frequencies as diplayed in the following plots,

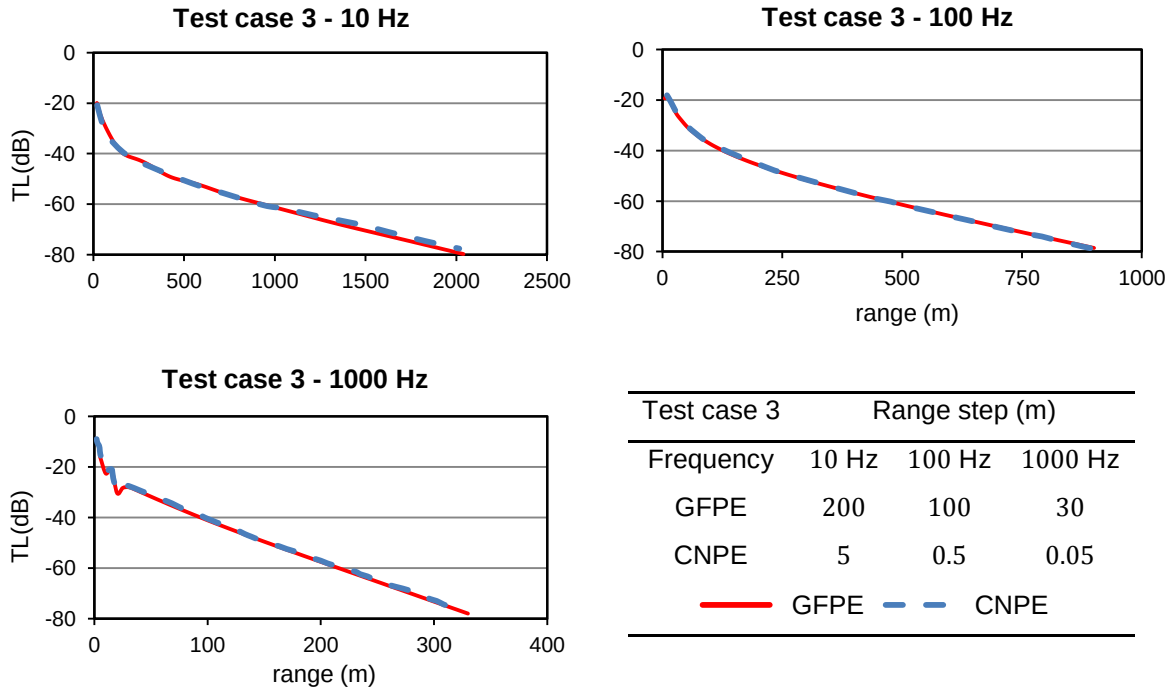

Test case 3	Range step (m)		
Frequency	10 Hz	100 Hz	1000 Hz
GFPE	200	100	30
CNPE	5	0.5	0.05

GFPE CNPE

Figure 5.4 - Comparison between the GFPE and the CNPE methods, with parameters from test case 3. The respective range steps used are displayed in the bottom right table.

Despite a slight difference of 1 dB over a range of 1000 m for a frequency of 10 Hz, the compared results of the methods are in good accordance. The range step values used for the GFPE method are from [Gilbert, et al., (1993)], although we verfied that larger values could be used with small difference in the sound levels. For example, for a frequency of 10 Hz, a range step of 500 m only has a 2 dB difference in relation to the CNPE method results. For 100 Hz, a range step of 250 m results in the same difference. By comparing the range steps on Figure 5.4, we conclude that the GFPE method range steps are 600, 200 and 40 times the ones of the CNPE method at 1000, 100, 10 Hz, respectively. This in turn corresponds into a faster calculation, without sacrificing accuracy. Nevertheless, the difference bewteen range steps can be higher, supposing that a slight difference in

the results is neglected. All the results were computed in a dual core desktop computer and it took less than 1 s to calculate the three frequencies in sequential order. The following plots are for test case 4, which has a medium with a downward refracting atmosphere.

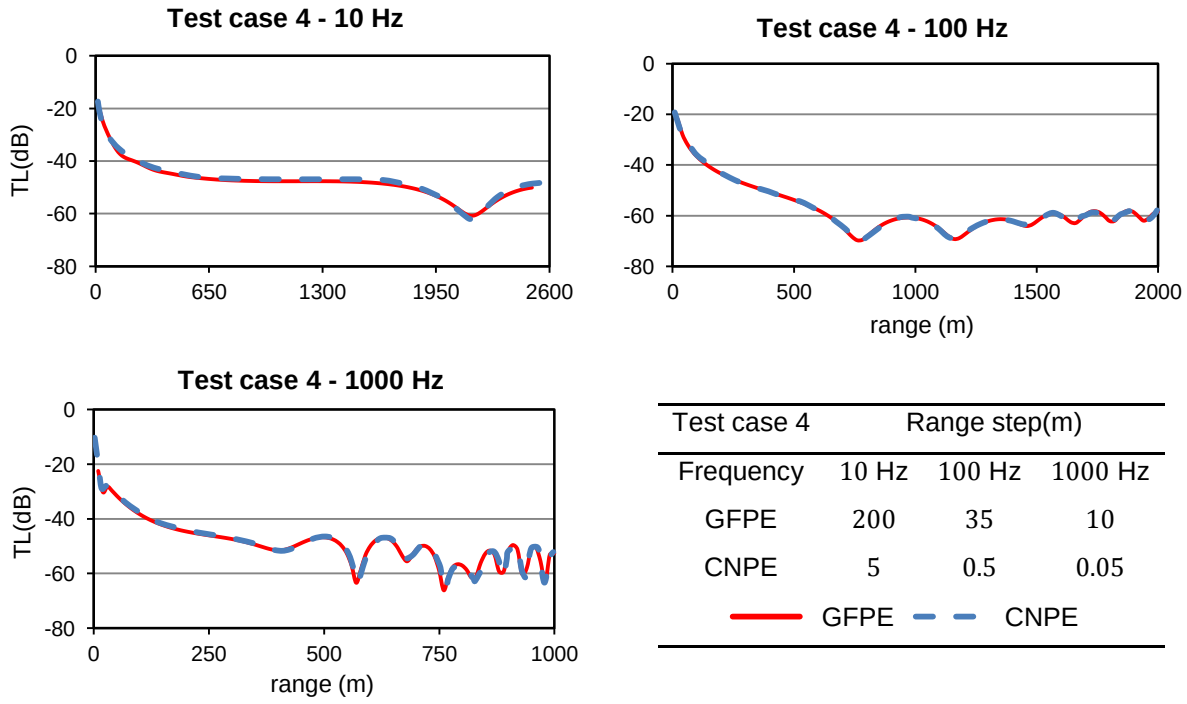

Test case 4	Range step(m)		
Frequency	10 Hz	100 Hz	1000 Hz
GFPE	200	35	10
CNPE	5	0.5	0.05

GFPE CNPE

Figure 5.5 - Comparison between the GFPE and the CNPE methods, with parameters from test case 4. The respective range steps used are displayed in the bottom right table.

Like the previous test case, the two lines of test case 4 are mostly indistinguishable for all frequencies. The oscillatory nature of the sound levels obtained, particularly for 100 and 1000 Hz, is a result of interference between the propagating modes. For the GFPE method, larger range steps can be used, with the disadvantage that the sound field oscillations can be inadequately represented.

By comparing the range step values, we conclude that the speed advantage of the GFPE over the CNPE method is smaller than the test case 3, where exists an upward refracting profile. Nonetheless, it is 40 to 163 times faster than the CNPE, depending on its frequency. The three simulations for test case 4 took about 2 s to complete, in sequential order.

In Figure 5.6, we study the accuracy of the GFPE method with a profile composed of three functions, which are represented on the bottom left plot of Figure 5.1. The agreement between the two methods is very good and both possess an oscillatory behavior for 100 and 1000 Hz. The explanation for this oscillation is similar for the one from test case 4. The range steps used for the GFPE method in test case 5 are identical with the ones used for test case 4 therefore, the speed advantage is identical as well. The three simulations for test case 5 took about 2 s to complete, in sequential order. Like the previous test case, we can use a larger range step if we are interested in obtaining the receiver sound level at some fixed range, thus neglecting the proper representation of the sound levels oscillations.

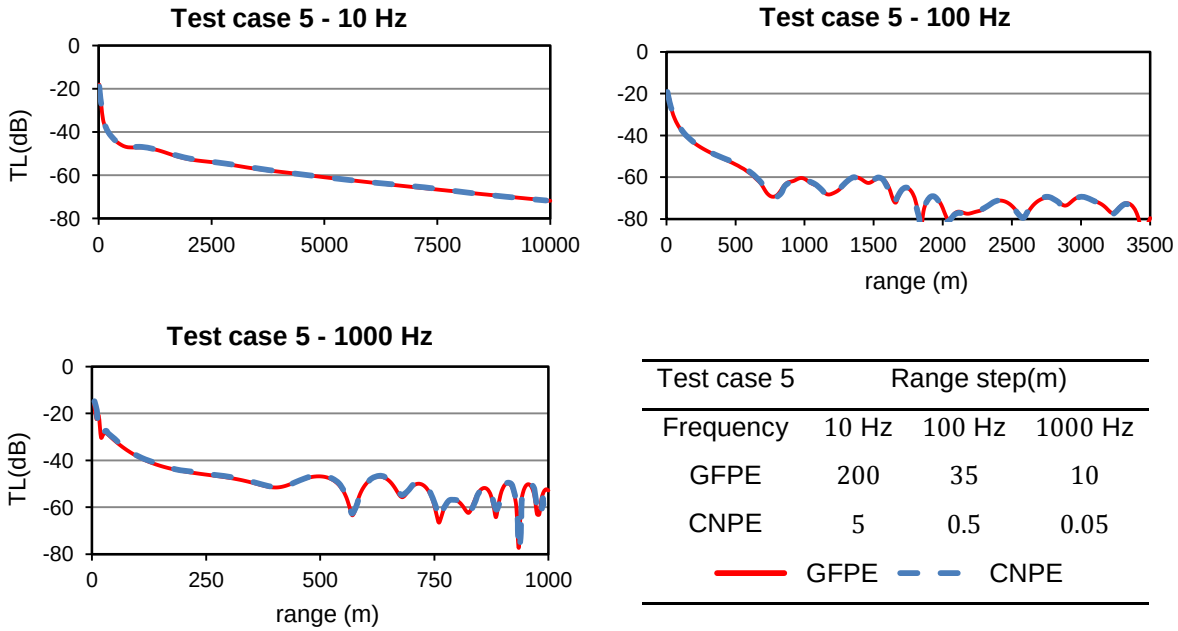

Test case 5	Range step(m)		
Frequency	10 Hz	100 Hz	1000 Hz
GFPE	200	35	10
CNPE	5	0.5	0.05

GFPE CNPE

Figure 5.6 - Comparison between the GFPE and the CNPE methods, with parameters from test case 5. The respective range steps used are displayed in the bottom right table.

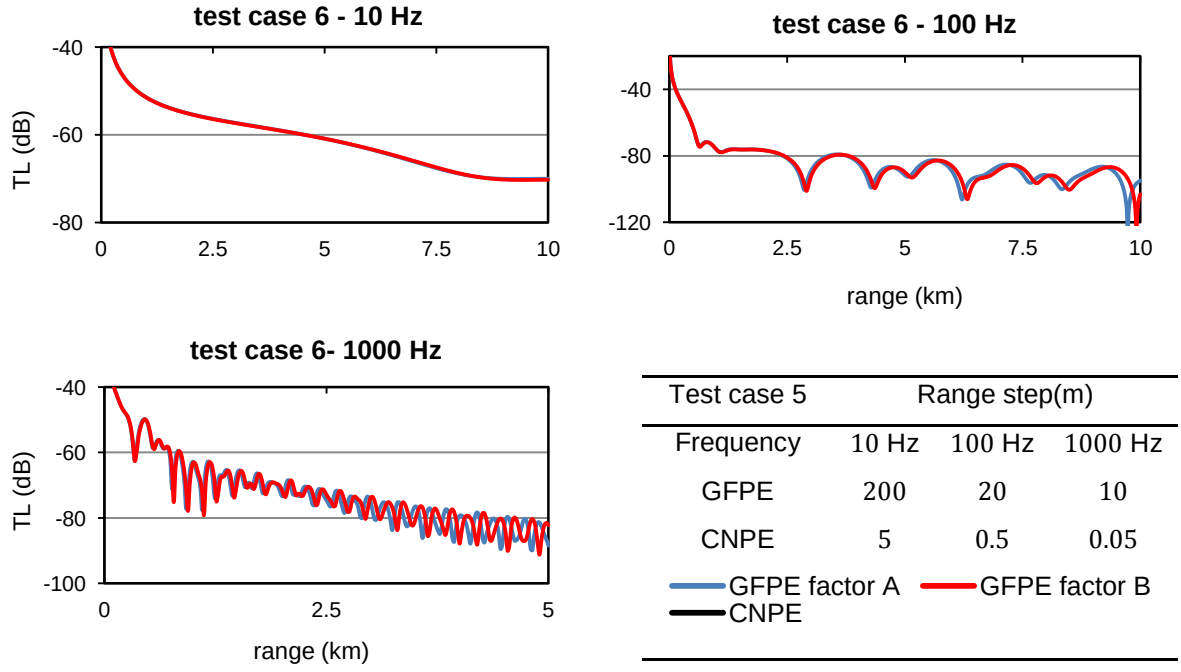

Test case 5	Range step(m)		
Frequency	10 Hz	100 Hz	1000 Hz
GFPE	200	20	10
CNPE	5	0.5	0.05

GFPE factor A GFPE factor B CNPE

Figure 5.7 - Comparison between the GFPE (two refraction factors) and the CNPE methods, with parameters from test case 6. The respective range steps used are displayed in the bottom right table.

Finally, we use test case 6 to study the accuracy of the developed program with a logarithmic sound speed profile and, simultaneously, we test the influence of the alternative refraction factor of

section 4.2.3. The blue solid line represents the GFPE method with the standard refraction factor (A) derived in section 3.5, while the red solid line represents the GFPE method with the alternate refraction factor (B) described in section 4.2.3. To test the accuracy of both refraction factors, we compare them with results from the CNPE method. We use this method because it yields a solution of the wide angle parabolic equation, which is more accurate than the low angle parabolic equation used in the GFPE.

For 10 Hz, the three lines are indistinguishable. For 100 Hz and up to 5 km, the three methods are in accordance. Over 5 km, the GFPE method with the standard refraction factor (A) starts to generate a phase error, but the GFPE method with alternate refraction factor (B) and CNPE method have equal results. Similar situation occurs for 1000 Hz, although the results deviate for a range over 2.5 km.

[Gilbert, et al., (1993)] reported no improvement with the alternate refraction factor. This is probably because [Gilbert, et al., (1993)] only tested both factors up to the range where the results were matching. Small phase errors have insignificant physical meaning at long range, as atmospheric fluctuations cause further phase shifts and the average sound levels are similar in both two factors. Despite this, all the simulations in this text use the alternate refraction factor (B).

By analyzing the range step values, we estimate that the GFPE method is 40 to 200 times faster than the CNPE method, depending on its frequency and the three simulations for test case 6 took about 13 s to complete, in sequential order. This value is larger than the previous ones due to the extreme long-range calculations performed.

Overall, all the test cases using the GFPE method were in accordance with the CNPE method therefore, we are confident that the numerical implementation developed for refracting atmosphere is accurate. As we stated, by comparing the range steps of the two methods, the speed advantage of the GFPE method is notorious, without sacrificing the accuracy.

5.3 TURBULENCE ANALYSIS AND RESULTS

In the previous sections, the program was validated by comparing it with other numerical methods or exact solutions, for an atmosphere with temperature refraction, wind and an acoustically absorbing ground. Turbulence effects are always present in a certain degree in experimental measures hence, they must be included in order to correctly compare the program with those measures. In this section, we compare the numerical program developed with sound levels collected from a real atmosphere.

5.3.1 Turbulence numerical parameters

The data used to compare the program belongs to an extensive set of measurements of sound propagation, in an upward refracting atmosphere done by Weiner and Keast [Weiner, et al., (1959)]. The turbulence parameters for the two spectral density functions (section 3.6.2) and for the refractive-index fluctuations (section 3.6.4), have to be correctly estimated to reproduce, as close as possible, the conditions of the experimental measurements.

[Ostashev, (1997)] gives the following parameters for the Gaussian spectrum [equation (3.47)]: correlation lenght $a = 1$ m, $\sigma_T^2/T_0^2 = 10^{-5}$ and $\sigma_v^2 = 0$. Those values are a good approximation of the real turbulent spectrum, but in a limited wave number range. In constrast, the von Kármán spectrum [equation (3.48)], agrees with the real spectrum over a larger wave number range. [Ostashev, (1997)] proposes the parameter ranges presented in Table 5.4, for the von Kármán spectrum.

Table 5.4 - von Kármán spectrum parameters

Parameter		Minimum value	Maximum value
C_T^2/T_0^2	$(\mathrm{m}^{-2/3})$	2×10^{-10}	6×10^{-7}
C_v^2/c_0^2	$(\mathrm{m}^{-2/3})$	1×10^{-9}	2×10^{-6}
K_0	(m^{-1})	1×10^{-2}	1

We used the following set of parameters for a turbulent atmosphere near a flat ground surface: $C_T^2/T_0^2 = 6 \times 10^{-7}\mathrm{m}^{-2/3}$, $C_v^2/c_0^2 = 2 \times 10^{-6}\mathrm{m}^{-2/3}$ and $K_0 = 1\ \mathrm{m}^{-1}$.

To estimate the parameters of the refractive-index fluctuation is necessary to calculate the size of the sum S and the wave number spacing Δk in equation (3.65). Figure 5.8 shows an example of the variation of the refractive-index flcutuation $\mu(r,z)$ [equation (3.62)] and its mode amplitude $G(k_r,k_z)$ [equation (3.63)], using the previous parameters for both spectra,

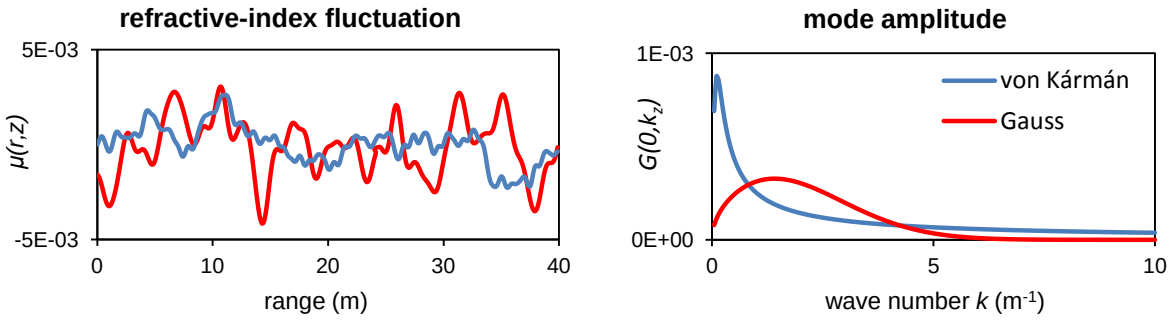

Figure 5.8 - Example of the refractive-index fluctuation $\mu(r,z)$, for a height of 2 m along a horizontal line in the r direction (left figure) and its corresponding mode amplitude $G(0,k_z)$ with $k_r = 0$ (right figure) for both von Kármán and Gauss spectra, using the parameters listed above. $S = 100$ and $\Delta k = 0.1\ \mathrm{m}^{-1}$ are the wave number parameters [equation (3.63)]

For the Gaussian spectrum, function $G(0,k_z) \approx 0$ for $> 7\ \mathrm{m}^{-1}$. In contrast, for the von Kármán spectrum, function $G(0,k_z)$ has finite value for $k = 10\ \mathrm{m}^{-1}$. Therefore, to calculate all the values of the von Kármán spectrum requires a large number of 'modes' S, being necessary to keep Δk small enough to correctly sample the small wave numbers. However, for most situations, $k_{\max} = 10\ \mathrm{m}^{-1}$ and $S = 100$ is enough to accurately represent the von Kármán spectrum, since wave numbers larger than

$10\ \mathrm{m}^{-1}$ generate small fluctuations of $\mu(r,z)$ [Salomons, (2001)]. Table 5.5 displays all the turbulence parameters used.

Table 5.5 - Turbulence parameters used

Gauss spectrum	von Kármán spectrum	Both spectra
$a = 1$	$\frac{C_T^2}{T_0^2} = 6 \times 10^{-7}\mathrm{m}^{-2/3}$	$S = 100$
$\frac{\sigma_T^2}{T_0^2} = 10^{-5}$	$\frac{C_v^2}{c_0^2} = 2 \times 10^{-6}\mathrm{m}^{-2/3}$	$\Delta k = 0.1\ \mathrm{m}^{-1}$
$\sigma_v^2 = 0$	$K_0 = 1\ \mathrm{m}$	$k_{\max} = 10\ \mathrm{m}^{-1}$

5.3.2 Experimental test cases

As refered in section 5.3.1, we use the experimental data from [Weiner, et al., (1959)] to compare the computational program with data collected from a real atmosphere. Weiner and Keast conducted an extensive program of measurements of sounds levels in an upward-refracting atmosphere.

The measured values were corrected for spherical spreading and atmospheric absorption and ajusted to be 0 dB at 30.5 m. We assumed the measured level is the same as the sound pressure relative to the free field hence, we use the relative sound pressure ΔL to compare the results [equation (2.4)].

The sound levels were measured at a height of 1.5 m, up to a distance of 1400 m from the source, which was placed at a height of 3.7 m. The source emitted octave bands of random noise, ranging from 300 to 4800 Hz. A sound band covers a specific range of frequencies and, in the particular case of an octave ban, the upper band frequency is twice the lower band frequency. Two octave bands from the experimental measures were considered: $300 - 600$ Hz and $600 - 1200$ Hz. The center frequency f_0 of an octave band is,

$$f_0 = \sqrt{f_1 f_2} \tag{5.1}$$

where f_1 is the lowest frequency and f_2 is the highest frequency in the octave bands previously considered. Using equation (5.1), the center frequencies are 424 and 848 Hz.

[Gilbert, et al., (1990)] studied the sound speed profile and concluded that a logaritmic profile was the most accurate representation of the atmosphere. The profile is written as,

$$c(z) = \begin{cases} c_0 + b\ln\left(\frac{z}{d}\right), z \geq z_0 \\ c_0 + b\ln\left(\frac{z_0}{d}\right), z < z_0 \end{cases} \tag{5.2}$$

where $c_0 = 340\ \mathrm{m/s}$, $z_0 = 0.01\ \mathrm{m}$ and $d = 6 \times 10^{-3}$. Two types of refraction where studied by [Weiner, et al., (1959)]: strong upward refraction and weak upward refraction. The first one refers to propagation almost directly upwind and the estimated refraction parameter is $b = -2\ \mathrm{m/s}$. The second one represents the sound propagation mostly crosswind (see section 0) and the estimated refraction parameter is $b = -0{,}5\ \mathrm{m/s}$. The two sound speed profiles are represented in the following plot, up to a height of 200 m. Additionally, Figure 5.10 visually elucidates the wind directions.

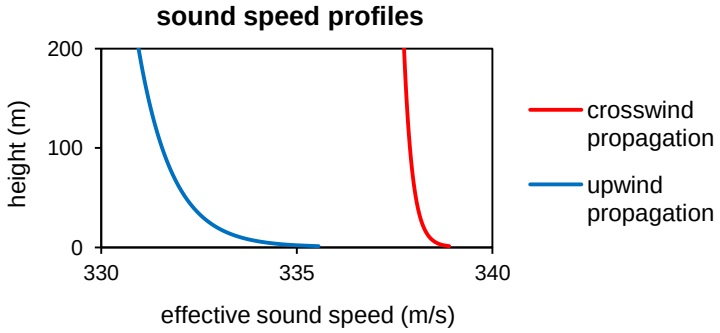

Figure 5.9 - Graphical representation of the sound speed profiles for upwind (solid blue line) and crosswind propagation (solid red line).

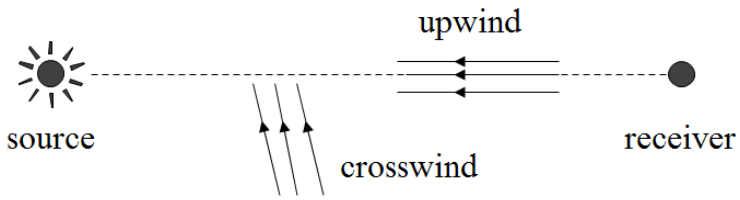

Figure 5.10 - Wind directions of the experimental measurement study by [Weiner, et al., (1959)].

The soil in the experimental measurement is described as a flat ground surface, covered with sparse vegetation, which can be simulated using a locally reacting plane with a complex impedance value representing grassland, as described in section 2.2.3. Using the empirical formulas of [Delany, et al., (1970)], the complex impedances for each source frequency are [Gilbert, et al., (1990)]: $8.00 + 9.24i$ and $5.17 + 5.57i$, for 424 and 848 Hz respectively.

Table 5.6 gathers the previous atmospheric and ground parameters for four test cases, each one with a specific frequency and sound speed profile.

Table 5.6 - Atmospheric and ground parameters from the experimental study

Test case	A1	A2	B1	B2
Frequency	424 Hz	848 Hz	424 Hz	848 Hz
Refraction	$b = -0.5\ \mathrm{m/s}$		$b = -2\ \mathrm{m/s}$	
Ground impedance	$8.00 + 9.24i$	$5.17 + 5.57i$	$8.00 + 9.24i$	$5.17 + 5.57i$
Source height	3.7 m		3.7 m	
Receiver heights	1.5 m		1.5 m	

5.3.3 Comparison of theory and experiment

In this section, we compare the results of the four test cases presented in Table 5.6 using the GFPE method, for an atmosphere with and without turbulence, with the sound levels measured by Weiner and Keast.

Each test case is represented bellow by two plots, one using the Gauss spectrum and the other using the von Kármán spectrum. Additionally, we calculated two different trials of the same test case, to evaluate how the refractive-index fluctuations μ influence the average sound levels.

Three different sound levels are presented. The connected red dots are experimental sound levels measure by Weiner and Keast. Each red dot represents the horizontal position of the microphones, which were used to measure, in dB, the sound levels. The solid lines are GFPE method solutions for a refracting turbulent atmosphere using either, the Gauss spectrum (green line, left side) or the von Kármán spectrum (blue line, right side). The dashed black lines are GFPE method outputs for a refracting atmosphere without turbulence. The following table displays the simulation parameters used in all test cases,

Table 5.7 - Simulation parameters for the experimental test cases

Parameter	424 Hz	848 Hz
horizontal spacing Δr (m)	5	5
vertical spacing Δz(m)	0.08	0.04
vertical points M	4096	8192
range steps	300	300

The following plots represent the test cases from Table 5.6, using the simulation parameters in the above table, with the arrangement described earlier in this section.

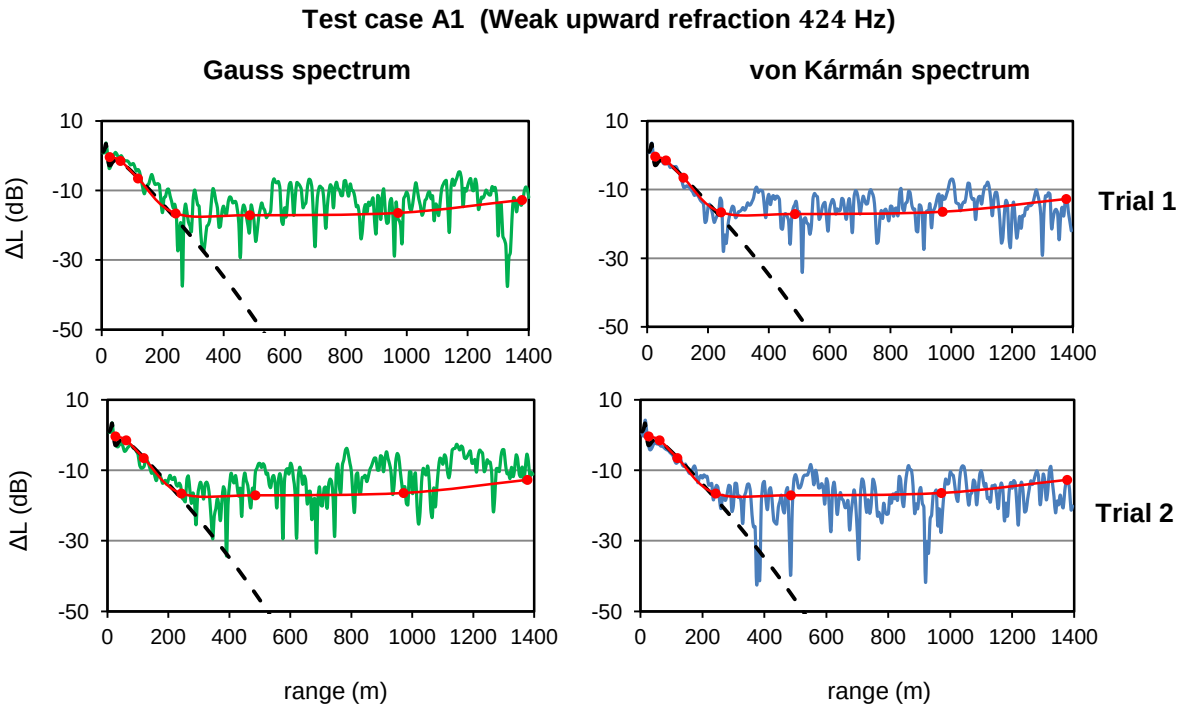

Figure 5.11 - Two trials of the relative sound pressure up to a range of 1400 m for test case A1

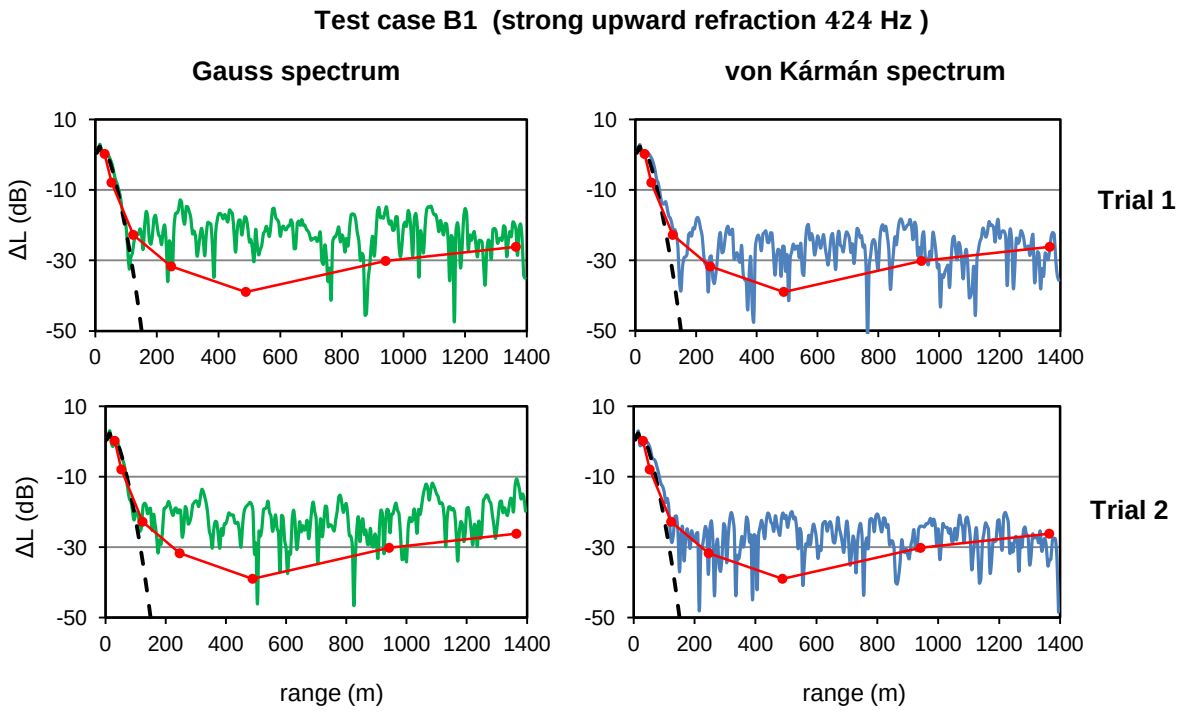

Figure 5.12 - Two trials of the relative sound pressure up to a range of 1400 m using test case B1

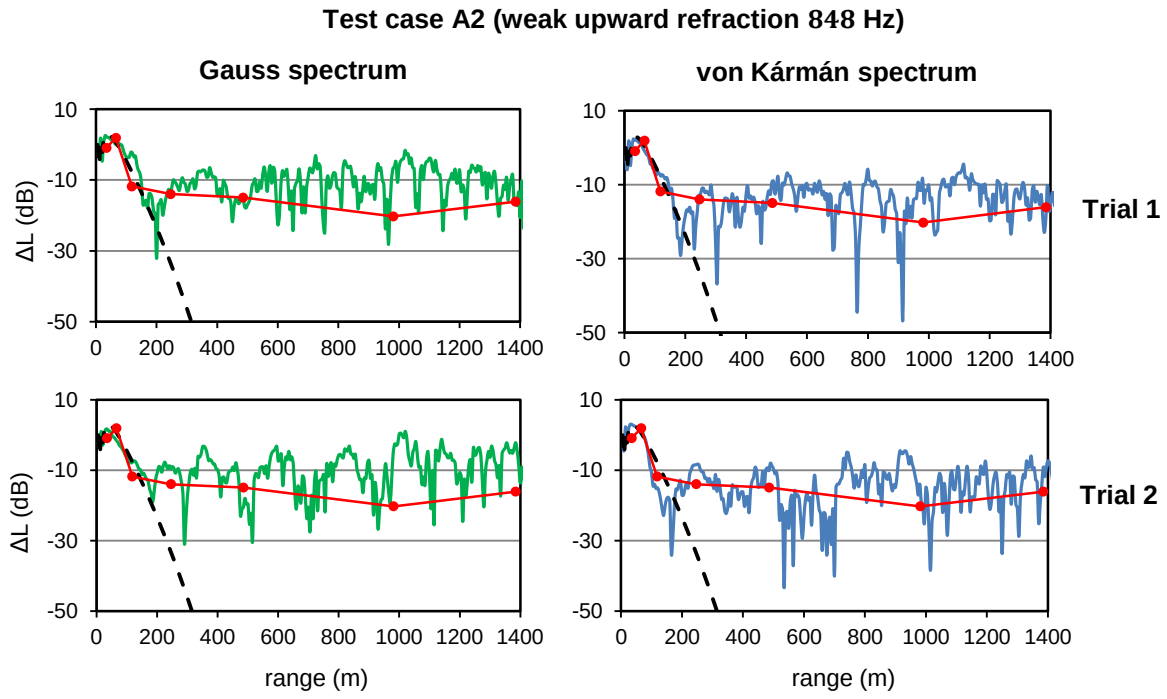

Figure 5.13 - Two trials of the relative sound pressure up to a range of 1400 m using test case A2

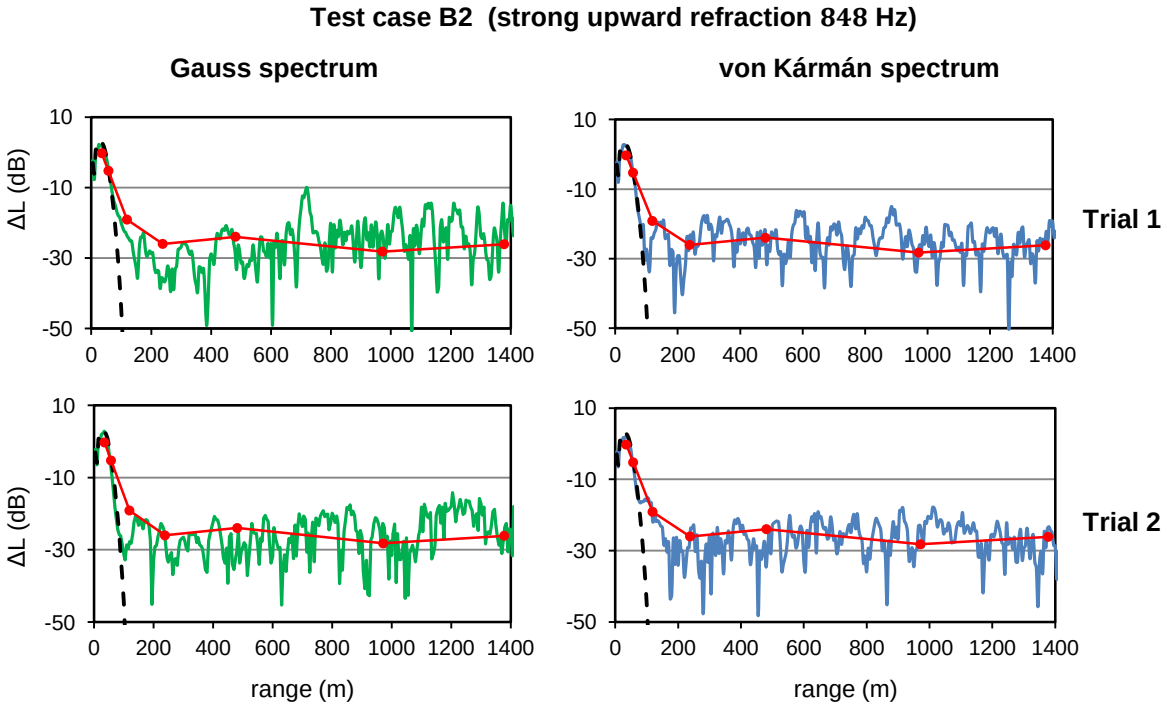

Figure 5.14 - Two trials of the relative sound pressure up to a range of 1400 m using test case B2

Overall, the results from the GFPE method with turbulence (green and blue solid lines) are in conformity with the experimental measurements (red connected dots), for both spectra. The exception

is test case B1 (strong upward refraction for 424 Hz), which differs 10 dB in the range from 500 m to 900 m. There is a slightly better agreement using the von Kármán spectrum, although the results with the Gauss spectrum are nearly identical. This is most likely because the von Kármán spectrum represents a wider wave number range therefore, a better fit to the 'real' spectrum (section 3.6.2). Additionally, for any of the test case, the average sound levels for the two trials are consistent hence, one trial is enough to accurately estimate them.

The spectral parameters initially assumed for a turbulent atmosphere close to a flat ground, are a reasoable representation of the medium where the sound levels were measured. Nonetheless, a perfect match with the experimental results is possible by a trial and error detailed adjustment of the parameters for both spectra, specially the correlation length a for the Gauss spectrum and the wave number K_0 for the von Kármán spectrum.

Results from the GFPE method without turbulence (black dashed line) are severely underestimated for a distance greater than 200 m. Up to a range of 200 m, all the three results are in accordance. This means that turbulent effects are small up to this distance thus, at short range, sound propagation is mostly governed by deterministic parameters such as the source frequency or the refraction parameter. For long range sound propagation (more than 200 m), the incorporation of turbulence effects is essential in order to obtain realistic sound pressure levels.

The results of these test cases can be approximated as a step function (Figure 5.15). In region 1 the sound levels remains constant thus, spherical spreading is present. The sound levels start to drop down (region 2) and then approach to a constant value (region 3).

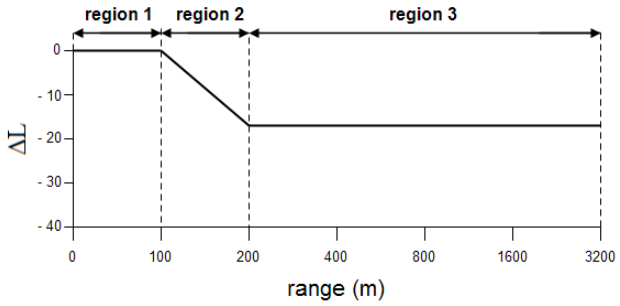

Figure 5.15 – Example of the step function for a turbulent upward refracting atmosphere.

From the results obtained from the test cases, we concluded that the shape of the step function depends mostly from the refraction parameter thus, from the wind direction and from the temperature profile. Source frequency has a slight influence in the shape of the step function, especially at short range. At longer range, sound levels do not depend much on frequency.

6 PROGRAM APPLICATION TO AN AIRPORT

In this section, we use the developed computational program to study the noise generated by an aircraft in the surrounding areas of an airport. This task requires information on air temperature and wind speed and direction, in the region where the sound propagates therefore, in section 6.1 we present how these profiles can be realistically estimated by using semi-empirical formulas that depend on ground and meteorological conditions. With these conditions, we can have a realistic set of sound speed profiles (section 6.2), which along with a proposed group of simulation parameters (section 6.3), allow us to study the influence of turbulence and wind on the noise produced by aircraft near an airport (sections 6.4, 6.5 and 6.6)

6.1 WIND AND TEMPERATURE PROFILES

Most sound propagation problems occur near the ground surface in a region called atmospheric boundary layer (ABL). This layer contains the lower part of the earth's atmosphere, which is strongly influenced by the presence of the earth's surface, causing variations on the meteorological parameters in a time scale of about an hour or less. The ABL height varies substantially, between some hundred meters up to 2 km, depending on the location and time of the day. The atmospheric surface layer (ASL) constitutes de lowest part of the ABL. It is the active link between the atmosphere and the surface of the earth, transporting between them momentum, heat and other factors. Despite being only about 10% of the ABL total height, it is where most sound propagation problems take place.

The vertical profiles of wind and temperature are influenced by the amount of turbulence present in the earth's atmosphere. Pasquill stability classes classify different atmospheric conditions based on incoming solar radiation (during the day), cloud cover (during the night) and wind speed. The six classes are displayed in Table 6.1 [Pasquill, (1961)].

Table 6.1 - Pasquill meteorological stability classes

Wind speed	Day - Incoming solar radiation			Night - Cloud cover	
(m/s)	Strong	Moderate	Slight	$> 4/8$	$< 3/8$
< 2	A	A - B	B	-	-
$2 - 3$	A - B	B	C	E	F
$3 - 5$	B	B - C	C	D	E
$5 - 6$	C	C - D	D	D	D
> 6	C	D	D	D	D

Class A represents a very unstable atmosphere with strong vertical mixing therefore, this type of atmosphere has large temperature gradients. Conversely, class F represents a stable atmosphere with weak vertical mixing. Class D corresponds to a neutral atmosphere, which has both high values of wind speed and cloud cover. Typically, the atmosphere is unstable during the day and stable during

the night thus, classes A - D are suitable for representing day time atmospheric conditions and classes D - F for nighttime atmospheric conditions. Moreover, large temperature gradients and high wind speed cannot coexist, since the strong turbulence present in an atmosphere with high wind speeds increases the fluid homogenization and therefore, inhibits the development of large temperature gradients.

Several empirical formulas were developed by meteorologists to predict the wind and temperature gradients, when direct measurement is impractical or unattainable. The formulas we use, are based on the Monin-Obukhov simularity theory [Monin, et al., (1979)], where a logarithmic function and a correction term (ψ_M and ψ_H) are used to describe the vertical distribution of horizontal wind speed and air temperature. The following equation estimates the horizontal wind speed u,

$$u(z) = \frac{u^*}{\kappa}\left[\ln\left(\frac{z}{z_0}\right) - \psi_M\left(\frac{z}{L}\right)\right] \tag{6.1}$$

The temperature T at a height z above the ground is,

$$T(z) = T_0 + \frac{T^*}{\kappa}\left\{\ln\left[\frac{z}{z_0}\right] - \psi_H\left(\frac{z}{L}\right)\right\} + \Gamma \tag{6.2}$$

The following table displays some of the parameters, as well as their respective values, from equations (6.1) and (6.2).

Table 6.2 - Definitions and values of the parameters used to describe the Monin-Obukhov profiles

u^*	Friction velocity (m/s)	Depends on the ground surface
z_0	Roughness lenght	See Table 6.4
T^*	Scaling temperature (K)	Depends on the ground surface
T_0	Air temperature at zero height (K)	Convenient to use 283
κ	Von Kármán constant	0.4 ± 0.01
Γ	Adiabatic correction factor ($°C/m$)	-0.01 for dry air
		> 0 stable atmosphere
L	Monin-Obukhov lenght (m)	< 0 unstable atmosphere
		$= \infty$ neutral atmosphere

Monin-Obukhov lenght L is a scaling parameter which depends upon the heat flux at the ground surface. As displayed on the previous table, positive and negative values of L represent stable and unstable atmospheric conditions respectively. With a neutral atmosphere, L has infinite value.

Different forms of the correction terms have been sugested for unstable and stable conditions [Stull, (1991)], [Paulson, (1970)] and [Brekhovshikh, (1980)]. Under neutral conditions $\psi_M = \psi_H = 0$. We use the following expression for the diabatic momentum profile correction function ψ_M,

$$\psi_M\left(\frac{z}{L}\right) = \begin{cases} 2\ln\left(\frac{1+x}{2}\right) + \ln\left(\frac{1+x^2}{2}\right) - 2\arctan(x) + \frac{\pi}{2} & \text{for } L < 0 \\ -5z/L \text{ for } L > 0 \end{cases} \quad (6.3)$$

with,

$$x = \left(1 - \frac{16z}{L}\right)^{1/4} \quad (6.4)$$

For the diabatic heat profile correction function ψ_H the expression is,

$$\psi_H\left(\frac{z}{L}\right) = \begin{cases} 2\ln\left(\frac{1+x}{2}\right) & \text{for } L < 0 \\ -5z/L & \text{for } L > 0 \end{cases} \quad (6.5)$$

Equations (6.3) and (6.5) are called Businger-Dyer profiles [Stull, (1991)] and are in accordance with measurements from a real atmosphere up to a height of 100 m. The evaluation of the Businger-Dyer profiles requires the value for the respective Monin-Obukhov lenght L. [Salomons, et al., (1994)] suggests evaluating L, using the Pasquill meteorological categories (Table 6.1), with the following expression,

$$\frac{1}{L} = B_1 \log(z_0) + B_2 \quad (6.6)$$

where z_0 is the roughness length and some typical values are described in Table 6.4 . The constants B_1 and B_2 are obtained from the following table,

Table 6.3 - Value of constants B_1 and B_2 for the six Pasquill classes

	Pasquill class					
	A	B	C	D	E	F
B_1	0.04	0.03	0.02	0	−0.02	−0.05
B_2	−0.08	−0.035	0	0	0	0.025

6.2 METEOROLOGICAL PARAMETERS

The meteorological and ground surface data used in this study are similar to the conditions found on the Portela airport in Lisbon. The roughness lenght z_0 is a corrective measure to include the effect of the surface roughness on wind flow, and its value is a fraction of the average height of the elements on the ground. Table 6.4 displays a few z_0 values for different types of ground surfaces, including an airport area.

Table 6.4 - Some typical roughness lengths z_0

Type ground surface	$z_0(\mathrm{m})$
Water areas (lakes, open sea)	10^{-4}
Grassland	0.01
Airport runway with some buildings	0.02
City	≥ 1

We use $z_0 = 0.02$ to simulate sound propagation near an airport runway.

[Wilson, et al., (2000)] performed numerical calculations for mean vertical profiles that obey Monin-Obukhov similarity. Some of the results obtained are displayed in the following table,

Table 6.5 - Parameters used in the Monin-Obukhov profiles for two meteorological conditions

Meteorological condition	Pasquill Class	$T_0\,(\mathrm{K})$	$u^*\,(\mathrm{m/s})$	$T^*\,(\mathrm{K})$	$1/L\,(\mathrm{m}^{-1})$	Stability
Moderate cloud cover and light wind	B	298	0.1	-0.33	-0.086	unstable
Moderate cloud cover and moderate wind	C	298	0.3	-0.11	-0.148	slightly unstable

With these parameters, we can obtain the wind [equation (6.1)] and temperature [equation (6.2)] profiles, for the two meteorological conditions. The profiles are represented in the following plots,

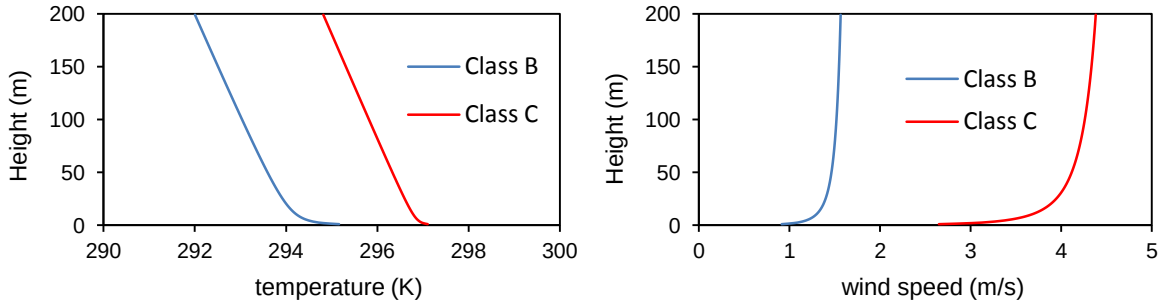

Figure 6.1 - Temperature (left) and wind (right) profiles, for the meteorological conditions from Table 6.5, up to a height of 200 m.

Using these values in equations (6.1) and (6.2), the two resulting sound speed profiles are calculated from equation (2.9), adding the horizontal sound speed u if the wind is directly downwind,

$$c(z) = c_0\sqrt{\frac{T(z)}{T_0}} + u(z) \tag{6.7}$$

If the wind is directly upwind, the horizontal wind speed u is subtracted. When the wind is directly crosswind, the wind speed u is zero. The sound speed profiles are represented in Figure 6.2, with the three previous wind directions, for the meteorological conditons from Table 6.5.

In the situation with light wind (Pasquill class B), the sound speed gradient is larger than with moderate wind (Pasquill class C), mostly due to the strong turbulence present in an atmosphere with high wind speeds (section 6.1). The wind speed always increases with height, although its direction can increase (downwind) or deacrease (upwind) the sound speed.

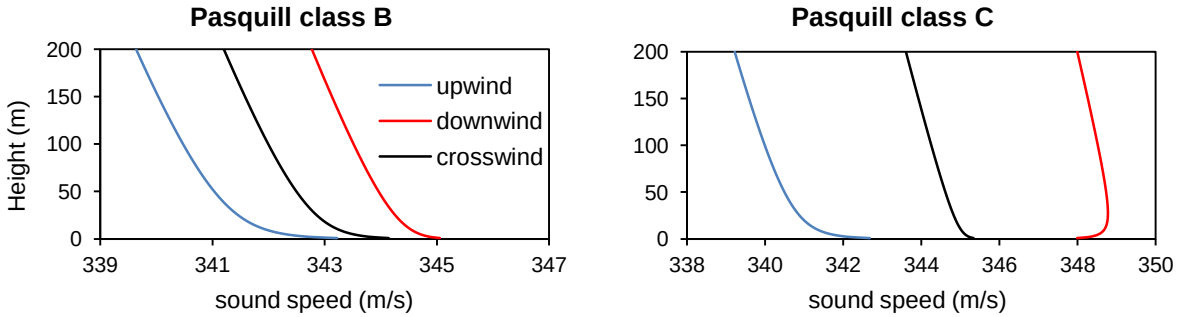

Figure 6.2 - Sound speeds obtained for two meteorological conditions from Table 6.5, including three different wind directions.

Additionally, turbulence has to be included in order to correctly estimate sound levels, particularly when a shadow region exists (section 6.4). For unstable conditons, [Zaporozhets, et al., (2011)] uses the following expressions to obtain the parameters of the Gaussian spectrum (section 3.6.2),

$$\sigma_v = 0.8\left(12 - 0.5\frac{z}{L}\right)^{1/3} u^* \tag{6.8}$$

$$\sigma_T = 2\left(1 - 18\frac{z}{L}\right)^{-1/2} T^* \tag{6.9}$$

Using the previous expressions, we can estimate the Gauss spectrum parameters for the two meteorological conditions in Table 6.5.

Table 6.6 - Gauss spectrum parameters at a height $z = 1\ \mathrm{m}$

Pasquill class	$a\ (\mathrm{m})$	σ_T^2/T_0^2	σ_v^2/c_0^2
B	1	1.93×10^{-6}	2.86×10^{-7}
C	1	1.49×10^{-7}	2.58×10^{-6}

6.3 SIMULATION PARAMETERS

Additionally to meteorological imputs, the GFPE method requires assumptions about source and receiver locations and type of ground surface. Aircraft generates noise from two main sources: aerodynamic noise and engine noise. Aerodynamic noise originates from the airflow around the aircraft fuselase and control surfaces, while engine noise is due to jet noise, although high bypass ratio turbofans also have high fan noise.

Two source heights were considered: 100 m and 2 m. The first one represents an aircraft taking off or landing, whereas 2 m stands for an aircraft taxiing, i.e., moving slowly on the ground, under its own power. The wind direction proposed in Figure 6.3 was headwind or blowing against the direction of travel, since this is the most frequent and favorable situation when taking off or landing. We assumed three receiver locations, to simultaneously simulate upwind (receiver A), downwind (receiver B) and crosswind (receiver C) sound propagation. The receiver's height was set at 1.5 m to represent the typical human ear height.

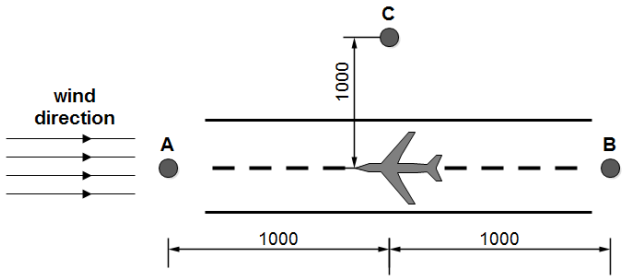

Figure 6.3 - Schematic representation of the source and receivers position (m) and wind direction.

The ground along the sound propagation path is a mixture of hardened asphalt, grassland and exposed soil. To simplify calculations, we assume an average value for the parameters used in the Attenborough's four parameter model [equation (2.7)]. The four parameters are,

i) porosity $\Omega = 0.3$,
ii) flow resistivity $\sigma = 300\ \mathrm{kPA \cdot s \cdot m^{-2}}$,
iii) s_f is the pore shape factor ratio $s_f = 0.75$
iv) grain shape factor $g = 0.5$

and the normalized ground impedances Z_g for an octave band spectrum are,

Table 6.7 - Normalized impedance values for an octave band spectrum

Frequency (Hz)	31.5	63	125	250	500	1000	2000
Normalized impedance	$29.4 + 29.0i$	$20.9 + 20.4i$	$15.0 + 14.3i$	$10.9 + 9.8i$	$8.1 + 6.6i$	$6.3 + 4.2i$	$5.3 + 2.5i$

Finally, Table 6.8 displays the test cases for the present study and their respective parameters.

Table 6.8 - Test cases and their respective parameters

Test case	up2	down2	cross2	up100	down100	cross100
Source height	2 m			100 m		
Receiver position	A	B	C	A	B	C
Receiver height	1.5 m					
Wind direction	upwind	downwind	crosswind	upwind	downwind	crosswind

6.4 EFFECT OF ATMOSPHERIC TURBULENCE ON SOUND PROPAGATION

In this section we use the proposed test cases to evaluate the influence of turbulence on sound generated by an aircraft in the vicinity of an airport.

Turbulence has three major effects on sound propagation:

i) lower wave front coherence
ii) random fluctuations of propagating sound waves in amplitude and phase
iii) randomly scatters energy into shadow regions.

The first two effects result in a spatial coherence loss that increases as the front waves propagate away from the source. This results into sound pressure fluctuations, from the average values. The one-dimensional plots, with the GFPE method from section 5.3.3, clearly display this effect.

The third effect of turbulence occurs when an acoustical shadow region forms. The shadow region occurs in the presence of a negative sound speed gradient (Figure 2.6), or when the sound waves encounter topographical obstructions such as barriers or hills. According to the sound ray theory (section 2.4.3), the shadow region is defined by exact boundaries thus, one side of the boundary has finite sound levels and conversely, on the other side (shadow region) the sound pressure is zero.

Experimental measurements carried by [Weiner, et al., (1959)], show that sound levels in the shadow region are significantly higher than expected by the ray theory. It is generally assumed that atmospheric turbulence affects the maximum attenuation achieved in a shadow region [Piercy, et al., (1977)]. Figure 6.4 exemplifies how turbulence increases the sound levels in the shadow region. Initially, a refracted spherical wave propagates with an angle θ with the horizontal line, called skywave. This area of propagation close to the source corresponds to region 1 from Figure 5.15 and Figure 6.5.

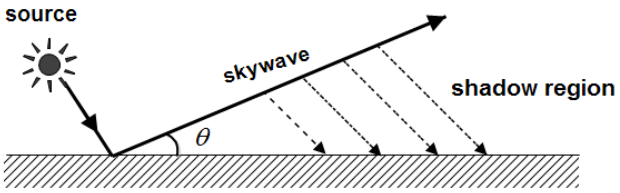

Figure 6.4 - Representation of scattering of sound into the shadow region.

The skywave then reaches the shadow region and consequently, the sound level starts to drop (region 2). The non-uniform nature of atmospheric turbulence causes the sound waves to scatter into the shadow region, raising the sound levels to an average constant value (region 3).

This phenomenon occurs in the presence of a negative sound speed gradient. To demonstrate it, we use two different types of sound speed profiles, with upwind and downwind sound propagation, from Table 6.8, and with class C atmospheric conditions (moderate wind). Then, we plot the results and compare the sound levels with and without turbulence (Figure 6.5). Moreover, the step function introduced in section 5.3.3 is also represented in the left plot.

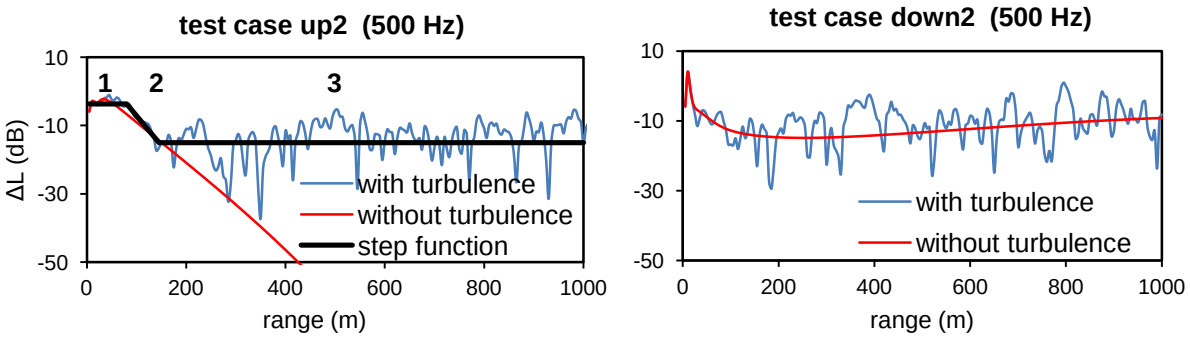

Figure 6.5 - One trial of the relative sound pressure up to a range of 1000 m using test case up2 (left plot) and test case down2 (right plot), with and without atmospheric turbulence.

As we are interested in studying the influence of wind and turbulence, we used the relative sound pressure to quantify sound levels. To calculate the sound pressure levels from an aircraft, or any other sound source at a certain distance, we use equation (4.21), which takes into account the sound power level from the source. By knowing the value of ΔL, it is easy to estimate the sound pressure level, since the geometrical spreading only depends on the distance from the source. Moreover, the atmospheric absorption attenuation can be considered constant through the sound propagation path.

With upwind propagation (left plot), the sound speed decreases with height (Figure 6.2) thus, a shadow region forms in region 3 (step function) and accordingly, the average sound levels relative to the free field remain constant throughout this region. When turbulence is not incorporated, the sound levels are largely underestimated.

With downwind propagation (right plot), the sound speed increases close to the ground (Figure 6.2) therefore, the sound speed gradient is positive within this region. In this situation, the sound levels without turbulence are in accordance with the average ones with turbulence. In this particular case, the addition of atmospheric turbulence is redundant and not mandatory.

When the source is located at 100 m, the sound levels without turbulence and the average ones with turbulence are similar, but not identical (Figure 6.6). Since the wind speed above a certain height is nearly constant (Figure 6.1), the sound speed gradient at a height of 100 m is only slightly negative (Figure 6.2). This explains why both the results are in close agreement, despite the fact that the sound waves are propagating in a negative sound speed gradient medium.

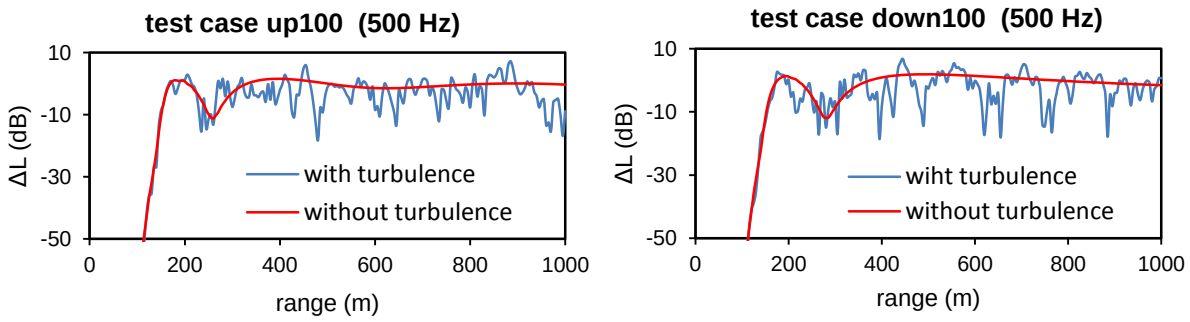

Figure 6.6 - One trial of the relative sound pressure up to a range of 1000 m using test case up100 (left plot) and test case down100 (right plot), with and without atmospheric turbulence.

To graphically illustrate how turbulence influences the penetration of sound waves into the shadow region, we use the test cases up2 and cross2 from Table 6.8 and plot a two-dimensional representation of the relative sound pressure field, with (right plot) and without (left plot) turbulence effects. Note that the relative sound pressure values below -50 dB have the same color.

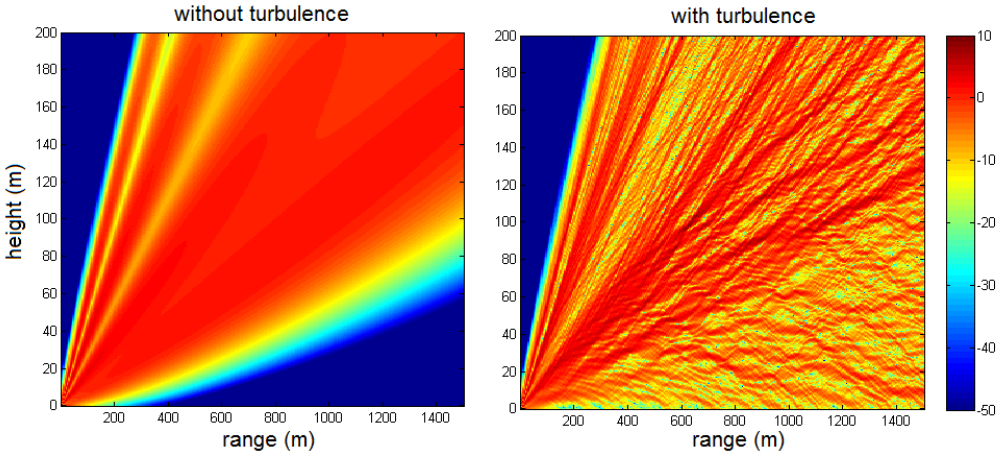

Figure 6.7 - Two-dimensional plots of the relative sound pressure level ΔL (dB), with parameters from test case up2. The source height is 2 m and the frequency is 500 Hz, with upwind propagation.

The skywave angle θ, for crosswind and upwind propagation, is about $3°$ and $4.5°$ respectively (note that the horizontal spacing is smaller than the vertical one). The blue region above the source is an area where the GFPE results are not valid. This drawback is also known as the angular limitation of the GFPE method and is described in section 2.4.2. From Figure 2.10, we can conclude that the results are accurate up to an angle of about $35°$ ($y_{max} \approx 35^{\circ}$), on both test cases.

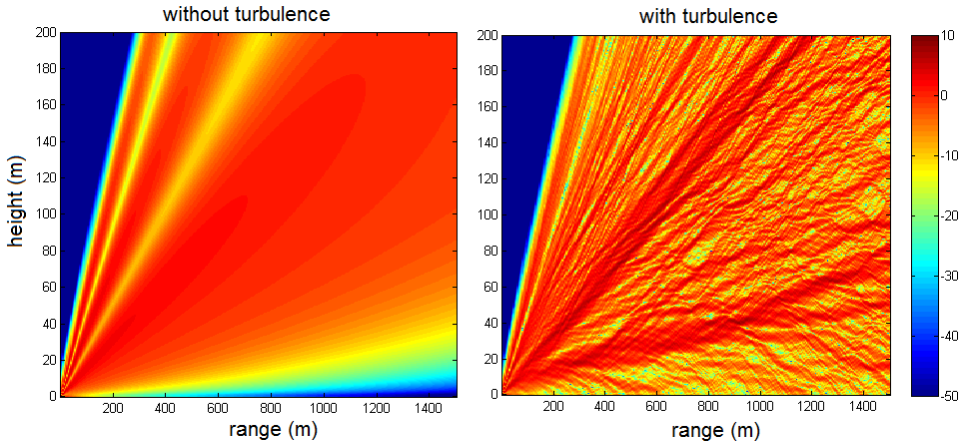

Figure 6.8 - Two-dimensional plots of the relative sound pressure level ΔL (dB), with parameters from test case cross2. The source height is 2 m and the frequency is 500 Hz, with crosswind propagation.

We obtained similar results for the remaining octave spectrum frequencies. These two-dimensional plots clearly show that sound pressure levels in a shadow region are a direct result of scattering due to atmospheric absorption. In their experimental study [Weiner, et al., (1959)] verified that the relative sound pressure levels, in the shadow region, were mostly independent of range. Furthermore, [Daigle, et al., (1986)] in the same conditions of the previous study, reported a limited dependence of relative sound pressure levels with height. These observations are in accordance, not only with the results from the two dimensional plots in this section, but also with the one dimensional plots from section 5.3.3.

From experimental and computational simulations, we conclude that the average relative sound pressure levels within the shadow region are, for the most part, uniform. Additionally, in a long range sound propagation perspective, in particular when a shadow region occurs due to the presence of a negative sound speed gradient, atmospheric turbulence has to be included to correctly estimate the sound pressure levels inside that region.

6.5 EFFECT OF WIND ON SOUND PROPAGATION

In this section, we study the influence of wind speed and direction on sound propagation. To accomplish this, we use the test cases from Table 6.8, with B and C class atmospheric conditions, and plot the results in a scale of octave bands, where each dot is a center frequency. Moreover, turbulence

is also included and we use the relative sound pressure ΔL to measure the sound levels [equation (2.4)]. The following two plots are for a source height of 2 m.

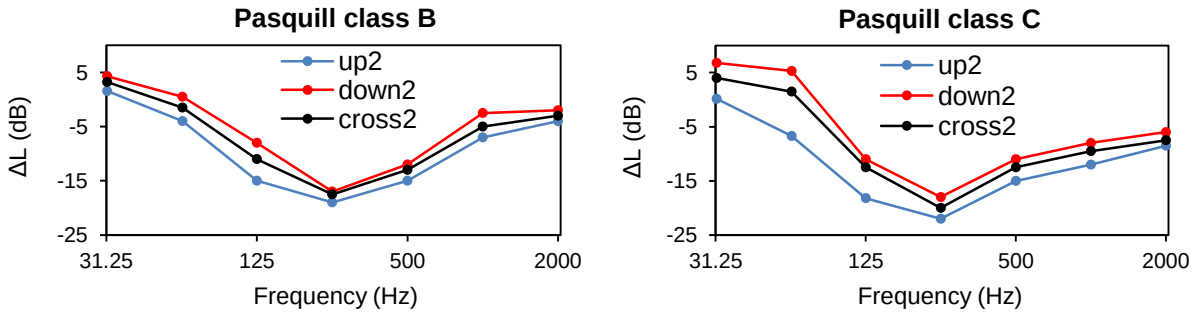

Figure 6.9 - Comparison of the relative sound pressure values, at a range of 1000 m, for three wind directions (three different receiver locations at a height of 1.5 m) , each one for light wind (left plot) and moderate wind (right plot) atmospheric conditions and for a source height of 2 m.

By comparing the wind directions in each plot, we infer that maximum attenuation is achieved when the wind is directly upwind (up2). When the wind direction is downwind (down2) a sound speed inversion for moderate wind occurs (C class atmospheric condition on Figure 6.2), which by turn results in less attenuation of the sound waves. With crosswind propagation (cross2), the attenuation value is between upwind and downwind propagation, as expected.

By comparing both meteorological conditions, we conclude that a stronger speed wind increases the attenuation on the sound levels and a light wind speed attenuates it less. Furthermore, the sound level difference between the three wind directions grows with increasing wind speed. The following plots are the same as the previous test cases, but for a source height of 100 m.

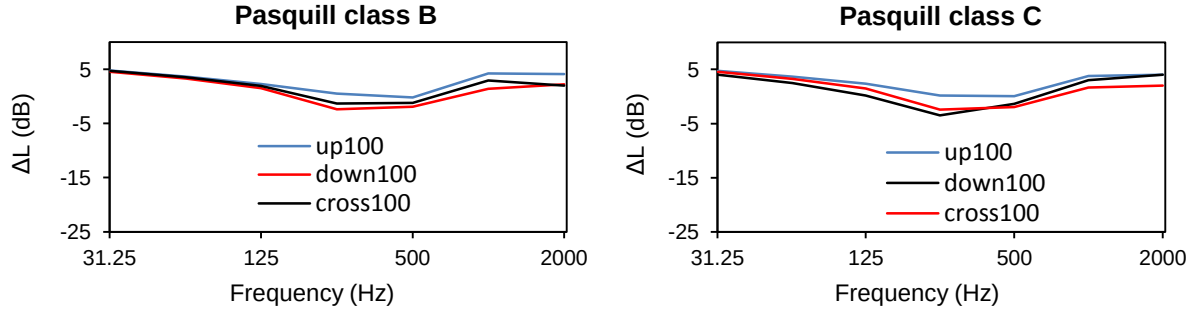

Figure 6.10 - Comparison of the relative sound pressure values, at a range of 1000 m, for three wind directions (three different receiver locations at a height of 1.5 m) , each one for light wind (left plot) and moderate wind (right plot) atmospheric conditions and for a source height of 100 m.

For a source height of 100 m, the attenuation achieved for a 1000 m range is smaller than the one for a source height of 2 m, for all test cases. This difference is due to two effects: the source distance

from the ground and the sound speed gradient. Since the source height in these test cases is greater than the one in the test cases from Figure 6.9, the ground surface has less influence on the sound levels. It does not absorb sound waves with the same intensity as if the source was 2 m above the ground. The other reason is the sound speed gradient becomes less intense as the height from the ground surface increases, due to the fact that the wind speed is nearly constant above a certain height. This effect minimizes the magnitude of refraction and consequently, as we verified in the first two plots of this section, the attenuation on the sound levels is smaller. It should be noted that the sound levels are average values and thus can vary considerably.

6.6 AIRPORT SCENARIO SIMULATION: CASE STUDIES

In section 6.3 we studied the influence of wind and turbulence on sound propagation, using two different situations: one close to the ground, at an altitude of 2 m, and the other at an altitude of 100 m. In the present section, we use the developed program to simulate two proposed scenarios, more realistic and complex. The first one simulates the noise emitted by an aircraft landing and the second one by an aircraft flying at a constant height.

Figure 6.11 illustrates case study 1, where an aircraft, initially at a height of 102 m, approaches the runway and lands (height of 2 m). The approach angle, also called glide slope, is approximately 3° above the horizontal (ground level), which is the one used in the Portela airport and in most airports. Like in section 6.3, we use different receivers to simulate different wind directions. Receiver A is positioned 500 m away from the point of landing, in the direction of landing. The sound emitted by the aircraft that reaches this receiver and the wind have opposite directions thus, the sound propagation is upwind. Receiver B is positioned as illustrated in figure 6.11 and accordingly, the sound propagation is downwind. The receiver's height was set at 1.5 m to represent the typical human ear height. We use the developed program to simulate the sound emitted by the aircraft in six points of the glide slope, each one with a horizontal spacing of 400 m.

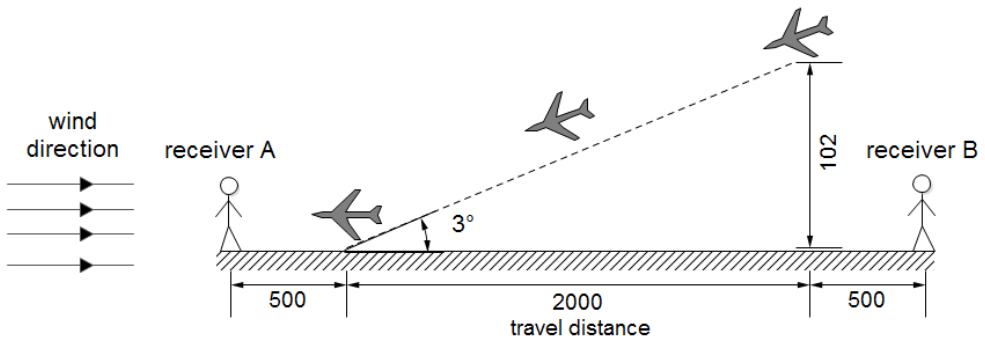

Figure 6.11 - Schematic representation of case study 1. All distances are displayed in meters.

Figure 6.12 illustrates case study 2, where we propose a scenario to simulate crosswind sound propagation. In this situation, an aircraft flies at a constant height of 20 m and the receiver C is positioned as displayed in Figure 6.12, at a height of 1.5 m. For the first 1500 m, the wind speed component and the sound traveling from the source to the receiver have opposite directions thus, the sound propagation is upwind and with decreasing intensity. Conversely, from 1500 to 3000 m the sound propagation is downwind, with increasing intensity. The wind speed component, when the aircraft travels exactly 1500 m, is zero (position 2), since the sound speed direction is perpendicular to the wind direction.

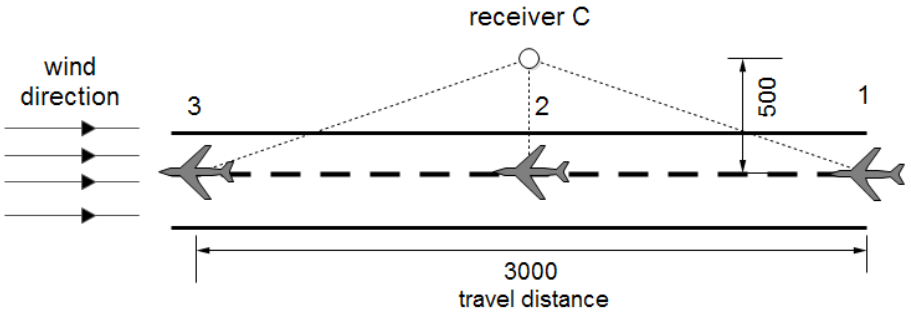

Figure 6.12 - Schematic representation of case study 2. The aircraft travels from position 1 to position 3 and all the distances are displayed in meters.

For the meteorological parameters we use both moderate wind and cloud cover (Pasquill class C) from section 6.2. For the ground parameters, we use the normalized ground impedance values from Table 6.7.

To obtain the sound pressure level L_p on the receivers we use the following expression [equation (4.21)],

$$L_p = L_w - TA \tag{6.10}$$

where TA is the total attenuation and is defined as,

$$TA = 10\log(4\pi R^2) + \alpha R + \Delta L \tag{6.11}$$

As in equation (4.21), the first term on the right hand side is the geometrical spreading, the second term is the atmospheric absorption and the third term is the relative sound pressure. With the total attenuation TA and the source power level L_w, we obtain the sound pressure level L_p.

As described in section 2.2.2, the atmospheric absorption depends on frequency, temperature, pressure and humidity. We assumed an average temperature of 20°C, relative humidity of 50% and air pressure of 1 atm. For a frequency of 250 and 1000 Hz, the atmospheric absorption is 1.3 and 4.66

dB/km, respectively [Piercy, et al., (1977)]. Furthermore, we assume that the geometrical spreading is spherical.

The following plots display the sound attenuation values due to geometrical spreading (black line), atmospheric absorption (red line) and meteorological and ground effects (blue line), for source frequencies of 250 and 1000 Hz. The total attenuation (green line), is the sum of all combined effects [equation (6.11)]. The horizontal axis represents the horizontal distance traveled by the aircraft. For the top left and top right plots (case study 1), 0 meters of horizontal travel refers to the initial position of the aircraft (height of 102 m) and 2000 m is the final position, at a height of 2 m. Similarly, for the bottom left plot, 0 m refers to the initial position 1 on Figure 6.12 and 3000 m refers to the final position 3.

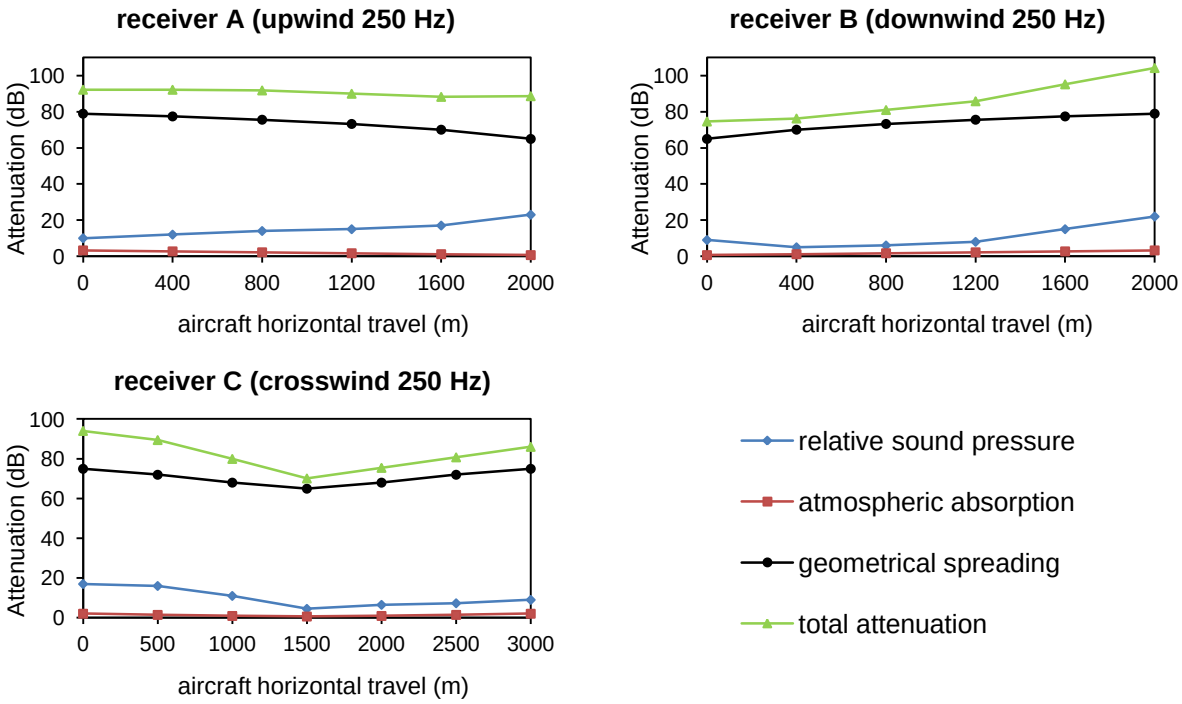

Figure 6.13 - Attenuation values for case study 1 (top left and top right plots) and case study 2 (bottom left plot), for a source frequency of 250 Hz. The horizontal axis represents the horizontal distance traveled by the aircraft.

For the receiver A, the distance between it and the aircraft decreases therefore, the atmospheric absorption and spherical spreading attenuation decrease with horizontal travel. Moreover, the relative sound pressure increases, since initially the source is at 102 m and its height decreases (up to 2 m), where the sound speed gradient is more intense. We verified this behavior in section 6.5. With these attenuation values, the total attenuation remains mostly constant at roughly 90 db.

For the receiver B the opposite occurs, the distance between the receiver and the aircraft increases hence, the atmospheric absorption and spherical spreading attenuation increase with horizontal travel. The relative sound pressure attenuation also increases, although with less intensity

than for the receiver A (upwind propagation). With these factors, the total attenuation increases from 75 to 105 db.

For the receiver C, the distance between the aircraft and the receiver decreases from 0 m up to 1500 m, where it reaches a minimum value, and then increases. The sound attenuation components also decrease up to 1500 m and afterwards increase. The relative sound pressure has more attenuation when the sound propagation is upwind (from 0 to 1500 m). When the propagation is downwind (from 1500 to 3000), the attenuation is less intense. We also verified this influence in section 6.5.

We carried out a similar analysis for a frequency of 1000 Hz (Figure 6.14).

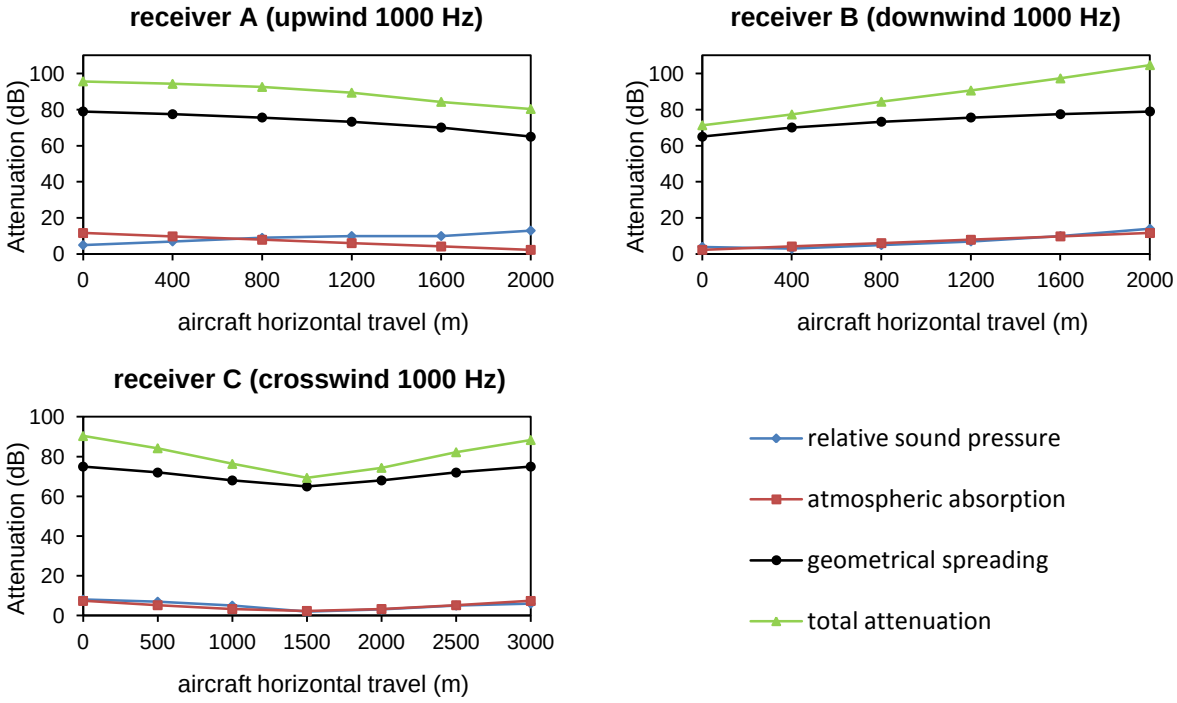

Figure 6.14 - Attenuation values for case study 1 (top left and top right plots) and case study 2 (bottom left plot), for a source frequency of 1000 Hz. The horizontal axis represents the horizontal distance traveled by the aircraft.

For 1000 Hz, the attenuations values have similar behavior, although the relative sound pressure attenuation is smaller. This difference of attenuation between different frequencies also was verified in section 6.5. In contrast, the atmospheric attenuation increases from 1.3 to 4.66 dB/km.

6.7 PROGRAM APPLICATION TO AN AIRPORT: CONCLUSION NOTES

In chapter 5 we validate the developed program, in an abstract situation, comparing the results with other methods and with real measures and its coherence was confirmed.

In this chapter a real situation associated with an airport was simulated. In fact, the parameters used reproduce an airport real situation namely, the source and receiver positions and the meteorological conditions. The coherent results obtained in the previous sections confirmed, once again, that the program developed is numerically accurate. Its user interface is also suitable and can be, easily and effectively, used to evaluate the effects of wind and turbulence on sound propagation near an airport.

7 GENERAL CONCLUSIONS AND FUTURE DEVELOPMENTS

In the last years, societies growing environmental and health conscience, obliged the national authorities to reinforce existing legislation concerning the maximum permissible noise levels.

In this context, the infrastructures that can generate significant levels of noise require studies, which must incorporate a large variety of parameters in order to reproduce the real situation. Nowadays, they consume a large amount of resources to obtain accurate results, with special relevance to the financial costs associated, as well as, the long time to complete them.

The existent methods, described in chapter 2, calculate the sound level in a given atmosphere with different degrees of complexity, accuracy and speed. Some of them do not incorporate many parameters that influence the real atmospheric sound behavior or are computationally inefficient. To incorporate the effect of wind and turbulence on sound propagation in the atmosphere, the most suitable numerical method is the Green's Function Parabolic Equation (GFPE) method, which its theoretical formulation is described in detail in chapter 3.

Since GFPE method does not allow an analytical solution, it was necessary to develop a numerical implementation (chapter 4) to solve the basic equations of the method (equations (3.40) and (3.41)). Several assumptions to develop the approach were introduced and justified. Some additional functions were also implemented, to overcome the limitations of the mathematical approach of the propagation physical phenomenon, such as the introduction of an artificial absorption layer, a window function and an alternate refraction factor. The functions were validated and they improved substantially the results accuracy and the computational effort.

The numerical implementation complexity requires a programming language, which must offer fast and precise mathematical calculations, a wide range of open source libraries and be able to run in different environments. For these reasons, C language was chosen to implement the program. The algorithm flow process is presented in section 4.3 and it includes a command line interface, with input and output files, which allows a friendly use.

In chapter 5, three sets of test cases were used to validate the numerical implementation developed. The first set is for a non-refracting atmosphere, which has a mathematical exact solution; the second set includes atmospheric refraction and was compared with the CNPE method results; finally, the third set includes atmospheric turbulence in addition to the previous conditions and was verified by comparing with experimental measurements. In all the test situations, the results accordance between the numerical implementation and the mathematical and benchmark cases, were good enough to assure that the numerical approach and the program developed are accurate.

Finally, in chapter 6, a real situation associated with an airport was simulated. Once again, it was confirmed that the program developed is numerically accurate and its user interface can be, easily and effectively, used to evaluate the effects of wind and turbulence on sound propagation in the vicinity of an airport.

Nevertheless the good results obtained with the approach in this thesis, it should be kept in mind that several limitations were considered. To achieve a yet more realistic description, new features can be incorporated in future developments such as, ground barriers, topographic features and vegetation. A three dimensional approach, an inhomogeneous and anisotropic turbulence model, and a combined model of GFPE method with the Ray Model, to overcome the angular limitation of the first, are other possible improvements to better represent sound propagation in the atmosphere.

8 REFERENCES

Abramowitz, M. and Stegun, I. A. (1972). *Handbook of Mathematical Functions with Formulas, Graphs and Mathematical Tables.* Dover, New York : s.n., (1972).

Attenborough, K. (1985). Acoustical impedance models for outdoor ground surfaces. *J. Sound & Vibration.* (1985), 99, pp. 521-544.

Attenborough, K., et al. (1995). Benchmark cases for outdoor sound propagation models. *J. Acoust. Soc. Am.* (1993), 97, pp. 173-191.

Brekhovshikh, L. M. (1980). *Waves in Layered Media.* second edition. New York : Academic, (1980).

Champeney, D. C. (1985). *Fourier Transforms in Physics.* Bristol : Adam Hilger, (1985).

Cooley, J. W. and Tukey, J. W. (1965). An algorithm for the machine computation of the complex Fourier series. *American Mathematical Society.* (1965), 19, pp. 297–301.

Daigle, G. A., Embleton, T. F. W. and Piercy, J. E. (1986). Propagation of sound in the presence of gradients and turbulence near the ground,. *J. Acoust. Soc. Am.* (1986), 79, pp. 613-627.

Delany, M. E. and Bazley, E. N. (1970). Acoustical properties of fibrous absorbent materials. *Applied Acoustics.* (1970), 3, pp. 105-116.

Di, X. and Gilbert, K. E. (1993). An exact Laplace transform formulation for a point source above a ground surface. *J. Acoust. Soc Am.* (1993), 93, pp. 714-720.

Dinapoli, F. R. and Deavenport, R. L. (1979). *Numerical models of underwater acoustic propagation.* Berlin : J. A. DeSanto, (1979).

Environment, European Comission for. (1996). *Green paper on Future Noise.* Brussels : s.n., (1996).

Frigo, M. and Johnson, S. G. (1997). *The Fastest Fourier Transform in the West.* s.l. : Massachusetts Institute of Technology, (1997).

Gabillet, Y., et al. (1993). Application of the Gaussian Beam Approach to Sound Propagation in the Atmosphere: Theory and Experiments. *J. Acoust. Soc. Am.* (1993), 93(6), pp. 3105-3116.

Gilbert, K. E. and Di, X. (1993). A fast Green's function method for one-way sound propagation in the atmosphere. *J. Acoust. Soc. Am.* (1993), 94, pp. 2343-2352.

Gilbert, K. E. and White, M. J. (1989). Application of the parabolic equation to sound propagation in the atmosphere,. *J. Acoust. Soc. Am.* (1989), 85, pp. 630-637.

Gilbert, K. E., Raspet, R. and Di, X. (1990). Calculation of turbulence effects in an upward-refracting atmosphere. *J. Acoust. Soc. Am.* (1990), 87, pp. 2428-2437.

Jensen, F. B. and Kurperman, W. A. (1994). *Computational Ocean Acoustics.* New York : American Institute of Physics, (1994).

Kaimal, J. C. and Finnegan, J. J. (1994). *Atmospheric Boundary Layer Flows: Their Structure and Measurement.* New York : Oxford U.P., (1994).

Lee, S. W. and Bong, N. (1986). Impedance formulation of the fast field program for acoustic wave propagation in the atmosphere. *J. Acoust. So. Am.* (1986), 79, pp. 628-634.

Lentovich, M. A. and Fock, V. A. 1946. Solution of Propagation of Electromagnetic Waves Along the Earth´s Surface by Method of Parabolic Equations. *Journal of Physics USSR.* 1946, 10, pp. 13-23.

L'Espérance, A., et al. 1992. Heuristic model for outdoor sound propagation based on an extension of the geometrical ray theory in the case of a linear sound speed profile. *Appl. Acoust.* 1992, 37, pp. 111-139.

Martin, J. (1993). *Simulation of wave propagation in random media: theory and applications.* Washington : IOP Publishing and SPIE, (1993). pp. 463-486.

Matsumoto, M. and Nishimura, T. (1998). Mersenne Twister: A 623-dimensionally equidistributed uniform pseudo-random number generator. *ACM Transactions on Modeling and Computer Simulation.* (1998), Vol. 8, pp. 3-30.

Monin, A. S. and Yaglom, A. M. (1979). *Statistical Fluid Mechanics: Mechanics of Turbulence.* Cambridge : MIT Press, (1979). Vol. 1.

Morse, P. M. and Fesbach, H. (1953). *Methods of Theoretical Physics .* New York : McGraw-Hill, (1953).

Munn, R. E. (1966). *Descriptive micrometeorology.* New Yok : Academic, (1966).

Zaporozhets, O., Tokarev, V. and Attenborough, K. (2011). *Aircraft Noise Propagation: Assessment, Prediction and Control.* s.l. : CRC Press, (2011).

Ostashev, V. E. (1997). *Acoustics in Moving Inhomegeneous Media.* London : E&FN Spon, (1997).

Pasquill, F. (1961). The estimation of the dispersion of windborne material. *The Meteorological Magazine.* (1961), Vol. vol 90, pp. 33-49.

Paulson, C. A. (1970). The mathematical representation of wind speed and temperature profiles in the unstable atmospheric surface layer. *J. Appl. Meteor.* (1970), 9, pp. 857-861.

Pierce, A. D. (1991). *Acoustics: An Introduction to its Physical Principles and Applications.* New York : American Institute of Physics, (1991).

Piercy, J. E. and Embleton, T. F. W. 1977. Review of noise propagation in the atmosphere. *J. Acoust. Soc. Am.* 1977, 61(8), pp. 1403-18.

Press, W. H., Flannery, S. A. and Teukolsky, S. A. (1986). *Numerical Recepies: The Art of Scientific Computing.* Cambridge : Cambridge U.P., (1986).

Raspet, R. and Lee, S. W. (1985). A fast-field program for sound propagation in a layered atmosphere above an impedance ground. *J. Acoust. Soc. Am.* (1985), 77, pp. 345-352.

Raspet, R., Baird, G. and Wu, w. (1992). Normal mode solution for low-frequency sound propagation in a downward refracting atmosphere above a complex impedance plane. *J. Acoust. Soc. Am.* (1992), 91, pp. 1341-1352.

Salomons, E. M. (1998). Caustic diffraction fields in a downward refracting atmosphere. *J. Acoust. Soc. Arm.* (1998), 104, pp. 3259-3272.

Salomons, E. M. (1998). Improved Green's function parabolic equation method for atmospheric sound propagation. *J. Acoust. Soc. Am.* (1998), 104, pp. 100-111.

Salomons, E. M., van den Berg, F. H. and Brackenhoff, H.E. A. (1994). Long-term average sound transfer through the atmosphere based on meteorological statistics and numerical computations of sound propagation. *Proceedings of the 6th International Symposium on Long Range Sound Propagation.* (1994).

Salomons, Erik M. (2001). *Computational Atmospheric Acoustics.* Netherlands : Kluwer Academic Publishers, (2001).

Stull, R. B. (1991). *An Introduction to Boundary Layer Meteorology.* Dordrecht : Kluwer, (1991).

Stull, R. B. (2000). *Meteorology for Scientists and Engineers, 2nd Edition.* s.l. : Brooks/Cole. A Division of Thompson Learning, (2000).

Takarskii, V. I. (1961). *Wave propagation in a turbulent medium .* New York : McGraw-Hill, (1961).

Tappert, F. D. (1977). *The parabolic approximation method.* [ed.] J. B. Keller and J. S. Papadakis. Springer-Verlag, Berlin : s.n., (1977). pp. 224-287.

Thomson, D. J. and Chapman, N. R. (1983). A wide-angle split-step algorithm for the parabolic equation,. *J. Acoust Soc. Am.* (1983), 74, pp. 1848-1854.

Weiner, F. M. and Keast, D. N. (1959). Experimental study of the propagation of sound over ground. *J. Acoust. Soc. Am.* (1959), Vol. 31, pp. 724-733.

Wescott, J. W. and Kushner, S. S. (1965). *Propagation of Sound in the Air.* University of Michigan (AD 465 678) : A Bibliography with Abstracts, Report of Geophysics Lab, (1965).

West, M., Gilbert, K. and Sack, R. A. (1992). A tutorial on the parabolic equation (PE) model used for long range propagation in the atmosphere. *Appl. Acoust.* (1992), 37, pp. 31-49.

Wilson, D. K. and Ostashev, V. E. (2000). A Reexamination of Acoustic Scattering in the Atmosphere Using an Improved Model for the Turbulence Spectrum. *in Proceedings of Battlespace Atmospheric and Cloud Impacts on Military Operations Conference 2000.* (2000).

Zwikker, C. and Kosten, C. W. (1949). *Sound Abosorbing Materials.* (1949).